

LONG PERIOD REGIONAL BODY WAVES

Thesis by

Terry C. Wallace, Jr.

In Partial Fulfillment of the Requirements

of the Degree of

Doctor of Philosophy

California Institute of Technology

Pasadena, California

1983

(submitted March 9, 1983)

-ii-

To my wife Karen

Acknowledgments

When I first came to the Seismo. Lab in the summer of 1978 I wasn't sure what I was getting into - it turned out to be a very pleasant experience. The faculty, students and staff provide an excellent environment for research. I have particularly benefited from the support of, and interaction with my thesis advisor Don Helmberger. Don, besides being a Minnesota Viking fan, has deluged me with ideas. I have also had the pleasure of working with Hiroo Kanamori and Dave Harkrider. I am indebted to Rob Clayton who made it possible for this thesis to be in this form. Although it is impossible to thank all the students by name, there are several who deserve special mention: Thome Lay, Jeff Given, Jim Pechmann and Marianne Walck. Gladys Engen was a valuable colleague and I would have been hard pressed to finish without her. Laszlo Lenches helped in the production of the figures. Karen Wallace typed much of the material in this thesis (and for a suprisingly cheap hourly rate!).

Most of the research was supported by the Advanced Research Projects Agency of the Department of Defense and monitored by the Air Force Office of Scientific Research under Contract F49620-77-C-0022. The U. S. Geological Survey Contract Nos. 14-08-0001-19755 and 14-08-0001-19270 supported the work on the Mammoth Lakes earthquakes.

Abstract

The seismograms recorded at regional distances (2° - 12°) are quite complicated due to the waveguide nature of the crust. The body wavetrains are essentially crustal reverberations. If these complicated waveforms are modeled with synthetic seismograms then significant information can be learned about the seismic source and the structure along the travel path. With certain restrictions, the long-period regional body waves (P_{nl}) from shallow, continental earthquakes can be modeled with a layer (crust) over a halfspace (mantle). Generalized ray theory and the Cagniard-de Hoop technique can be streamlined for computing a synthetic seismogram in such a structure. We present an approximation to the travel time equation which results in an analytic inversion for the de Hoop contour. The simplicity of the individual rays requires that the displacement potential need only be evaluated at a small number of time points; small changes in structure are, to first order, expressed in terms of the timing of different arrivals. It is possible to "stretch" or "squeeze" the synthetic to simulate a change in structure. Therefore, a single Green's function can be used to investigate a whole suite of structural models.

If the average crustal structure is known, the P_{nl} waveforms are insensitive enough to structural details to allow the extraction of source parameters of moderate size earthquakes. The technique which is used is an iterative least-squares waveform inversion which makes use of an error function determined by the cross-correlation of an observation and a synthetic. Since any synthetic seismogram is a combination of the three fundamental faults, the error functions can be written as a

series of cross-correlations multiplied by constants corresponding to source orientation. Once the cross-correlations are computed the source orientation is determined iteratively, and only the constants have to be recalculated. The inversion procedure requires only a small data base. Several examples are presented to demonstrate its usefulness.

If the source orientation is known, then differences in the synthetic waveform and observed P_{nl} can be parameterized in terms of the crustal thickness and Pn velocity. An inversion technique based on the error function previously described has been developed to determine crustal structure from P_{nl} . Once the structure is known for many paths a regionalized map can be produced. Such a map is presented for the western United States.

The ability to efficiently model P_{nl} makes it possible to use it as a routine tool. We present two examples of this procedure, the first of which is the 1980 Mammoth Lakes earthquake sequence. The fault mechanisms which are determined at long-periods (> 5 seconds) differ significantly from those determined by the distribution and polarity of local short-period first motions. Although it is not possible to isolate the cause of the discrepancy, at least part of it appears to be structurally related. Local short-period arrivals which travel through the Long Valley Caldera could be systematically deflected. The second example involves the signature of tectonic release on the long-period P waves from underground nuclear explosions. The distortion of explosion waveforms can be modeled as a double couple which has a strike-slip orientation. The modeling of the sP phases at upper mantle distances requires time functions which have short durations. The short duration can be interpreted in terms of very high stress drops if the tectonic release is triggered fault motion. For this reason we prefer a driven fault model.

Table of Contents

Introduction	1
References	5
Chapter I: Some useful approximations to generalized ray theory	
for regional distance seismograms	
1.1 Introduction	6
1.2 Evaluation of the synthetic response	9
1.3 Changes in model parameters	19
1.4 Discussion	26
1.5 Conclusions	34
References	35
Chapter II: The inversion of long-period regional body waves for	
source parameters	
2.1 Introduction	38
2.2 The Green's functions	39
2.3 Inversion technique	48
2.4 Examples	53
2.5 Discussion	67
2.6 Conclusions	73
References	74
Chapter III: The inversion of long-period regional body waves for	
crustal structure	

3.1 Introduction	76
3.2 Inversion procedure	79
3.3 Example: the western U.S.	86
3.4 Discussion	94
3.5 Conclusion	95
References	96
Chapter IV: Analysis of several earthquakes near the Long Valley Caldera	
4.1 Introduction	98
4.2 Long-period mechanism	101
4.3 Comparison between the long- and short-period mechanisms	122
4.4 Discussion	128
4.5 Conclusions	138
References	139
Chapter V: Evidence of tectonic release from underground explosions	
 in long-period P waves	
5.1 Introduction	141
5.2 Comparison of explosions and earthquakes	143
5.3 Analysis	147
5.4 Discussion	165
5.5 Conclusions	171
References	172
Appendix V-1	175

Introduction

Jack Oliver once wrote that the long range goal of seismology is to understand every wiggle on the seismogram. Throughout the history of the science steady progress has been made towards this end. First with the identification of different phases, which led directly to the gross structure of the earth. The next step was to use the waveform shape, such as in dispersion studies. This led to the refinement of the earth structure. The final step is to actually model the waveforms. This is a difficult task because one must separate the source and propagation effects, but at the same time the benefits are large. By fitting a waveform with a synthetic the use of the information contained in the seismogram is maximized. The body waves at teleseismic distances ($>30^\circ$) are fairly simple since the earth response is known, and their use has become rather routine. At upper mantle distances ($14^\circ - 30^\circ$) the modeling is much more challenging, but the state of the science is such that a new upper mantle model is not accepted without a synthetic fit to the observations. At regional distances, ($<12^\circ$) the seismograms become very complicated due to the waveguide nature of the crust. The purpose of this thesis is to understand and make use of the long-period body waves at regional distances (P_{nl}). The first three chapters discuss various techniques for using P_{nl} , while the last two use P_{nl} data as a tool in solving seismological problems.

Chapter I discusses the technique for generating synthetic regional distance seismograms. We use generalized ray theory because of the physical insight which it offers. With generalized ray theory it is possible to measure the response from a

single ray. On the other hand, great care must be taken to assure that all the rays which are important are summed in the response. The ray set must be extensive enough to be accurate yet limited enough to be practical in terms of computation time. It is possible to streamline generalized ray theory to investigate the waveguide problem. By assuming a layer (crust) over a halfspace (mantle) model we make use of a series of approximations. The first of these assumes that the de Hoop contour for a given ray is most strongly dependent upon the fastest velocity of any leg of the ray. This results in an analytic, although approximate, contour. Since each ray in the waveguide is basically two arrivals (a headwave and a reflected arrival) the response of the ray need only be evaluated at a few points about these arrivals and interpolated in between. We have found that it is sufficient to describe the response of each ray with just 15 time points. A change in structure most strongly affects the relative timing of the headwave and reflected arrival for a given ray so it is possible to "stretch" or "squeeze" the P_{nl} waveform of a representative model to simulate a whole suite of models.

Chapter II discusses a technique for the extraction of source parameters of moderate size earthquakes from P_{nl} waveforms. The technique is a least-square inversion which is based on the comparison of the observed and synthetic waveforms. Although the synthetic waveforms are constructed using Green's functions for a single structural model, we have found that they are adequate for most continental regions (they are particularly suited to the western U. S., where most of my interest is). The inversion is parameterized in terms of strike, dip and rake. The number of inversion parameters is kept to a minimum so that inadequacies in the Green's functions are not over-emphasized. The inversion does not require a large data set, and will allow the determination of source parameters of many earthquakes

which would otherwise be ignored. This technique can also be useful for historic events which typically have sparse data sets. The work in chapter II has been published in two papers; *Wallace, Helmberger and Mellman, 1981*; and *Wallace and Helmberger, 1980*.

Chapter III discusses a technique for the inversion of P_{nl} data for crustal structure. The standard technique used in crustal structure studies is seismic refraction, but if one wants a regionalized map over a large area (say, the western U. S.) then refraction studies are prohibitive in terms of expense and time. It is possible to take advantage of the "stretch" and "squeeze" analysis presented in chapter I to develop partial derivatives of the waveform with respect to the structural parameters of crustal thickness and Pn velocity. Therefore, it is possible to fit each travel path with an "average" structure. After the crustal parameters are determined for many different paths, they can be combined using a block-type inversion to produce a regionalized crustal structure. We have produced such a regionalized map for the western U. S., and by comparison with refraction results, the resolution of the technique is surprisingly good.

Chapter IV summarizes the analysis of several earthquakes near the Long Valley Caldera. This is one of the most exciting regions in California in terms of geophysics. There is good evidence of some type of magma migration; general uplift in the western portion of the caldera, screening of S waves which cross the caldera and intense swarms of small earthquakes. This chapter can be considered as an "example" of how regional body waves and the techniques discussed in the previous two chapters can be used. The source parameters of seven events were determined. The mechanisms we determined from long-period waveforms differ significantly from those determined with local short-period first motions. The short-period focal

mechanisms require vertical strike-slip faulting, while invariably the long periods require oblique slip on more moderately dipping faults. This discrepancy is discussed in detail in chapter IV, although at this time it is not possible to isolate the cause as either structurally related or source complexity. The research in this chapter is published in two papers: *Given, Wallace, and Kanamori, 1982*; and *Wallace, Given, and Kanamori, 1982*.

Chapter V is another example of how regional body waves can be used. The surface waves from numerous explosions require that there be a substantial non-isotropic component in the source. In addition, teleseismic SH waves have been observed from the same explosions. A widely accepted explanation for this non-isotropic radiation is the release of tectonic strain. We use the P_{nl} waveforms and upper mantle long-period P waves from megaton explosions at Pahute Mesa at NTS to quantify the tectonic release. The tectonic release can be sufficiently represented as a double couple, which is predominantly strike-slip. It is apparent that high stress drops are required on the basis of modeling the sP phase. Because there is not a short-period signature of the tectonic release, we prefer a driven fault for the release mechanism. The work in this chapter has been published in a paper by *Wallace, Helmberger, and Engen, (1983)*.

REFERENCES

- Given, J.W., T.C. Wallace and H. Kanamori (1982). A teleseismic analysis of the 1980 Mammoth Lakes earthquake sequence, *Bull. seismo. Soc. Am.*, 72, 1093-1110.
- Wallace, T.C., D.V. Helmberger and G.R. Mellman (1981). A Technique for the inversion of regional data in source parameter studies, *J. Geophys. Res.*, 86, 1679-1685.
- Wallace, T.C. and D.V. Helmberger (1982). Determining source parameters of moderate-size earthquakes from regional waveforms, *Phys. Earth Planet. Int.*, 30, 185-196.
- Wallace, T.C., J.W. Given and H. Kanamori (1982). A discrepancy between long- and short-period mechanisms of earthquakes near the Long Valley Caldera, *Geophys. Res. Lett.*, 9, 1131-1134.
- Wallace, T.C., D.V. Helmberger and G.R. Engen (1983). Evidence for tectonic release from underground nuclear explosions in long-period P waves, *Bull. seismo. Soc. Am.*, 73, 326-346.

Chapter I: Some Useful Approximations to Generalized Ray Theory for Regional Distance Seismograms

1.1 INTRODUCTION

The body wavetrains of seismograms at regional distances are much more complicated than those at teleseismic distances because of the waveguide properties of the crust. *Oliver and Major* (1960) were the first to quantify some of the long-period regional arrivals when they discussed the phase PL, which they defined as the normally dispersed, long-period oscillatory train during the interval between the initial P and S waves (by their definition PL is in exclusion of such phases as P_n, pP_n, sP_n). PL is the fundamental mode of a family of leaking modes and represents the multiple reflections of P and SV waves in the crustal waveguide. *Phinney* (1961) and *Gilbert and Laster* (1962) developed the theoretical modal representation and numerous authors (*Oliver*, 1964; *Poupinet*, 1972; *Rial*, 1976; to name a few) have used dispersion curves derived from PL to model crustal structure. *HelMBERGER and Engen* (1980) have broadened the understanding of long-period (greater than 3-5 seconds) regional phases by defining the entire wavetrain between P and S as P_{nl} . Figure 1-1 shows some typical P_{nl} waveforms for shallow earthquakes. For reference, the longest period part of the P_{nl} waveforms has been denoted PL.

It is obvious that the onset of P_{nl} is dominated by P wave energy. The ray description of this energy corresponds to P_n; that is, P waves which bounce several times in the crust and then travel as headwaves along the Moho. The later portions

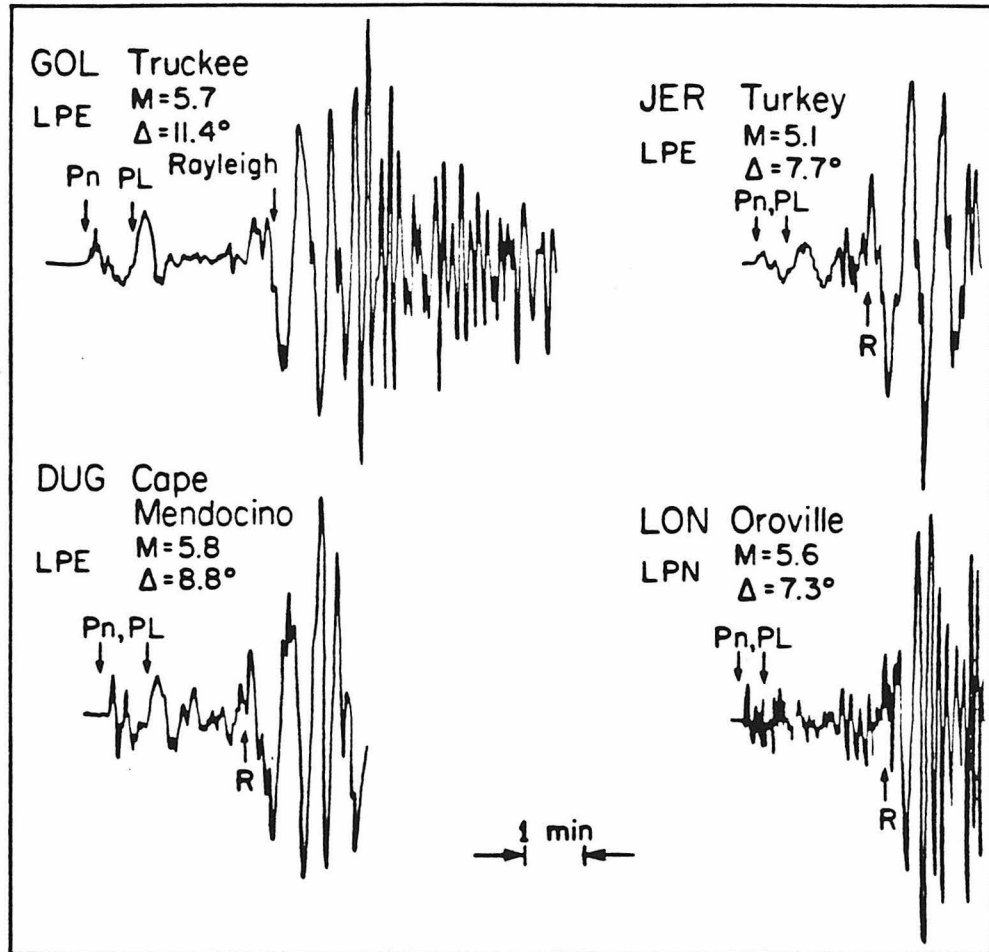


Figure 1-1: The horizontal component of motion for four moderate-size earthquakes. The magnitude and distance to the recording stations are given for each. Clockwise from the upper left: (1) September 12, 1966, Truckee, CA, strike-slip event; (2) June 13, 1965, southwest Turkey, normal event; (3) August 1, 1975, Oroville, CA, normal event; and (4) December 10, 1967, off the coast near Cape Mendocino, CA, strike-slip event.

of P_{nl} contain progressively more SV energy corresponding to PL and the rays which are reflected in the crust and undergo subsequent mode changes at the free surface and the Moho. The interference of all the rays gives rise to the waveform; parameters such as the crustal thickness and velocity contrast between the crust and Moho control the character of the waveform. There are several characteristics of P_{nl} . First, since only P and SV energy is involved it should be polarized in a vertical plane. The rotation of over 50 seismogram pairs has shown that typically there is very little multipathing energy present. The excitation of P_{nl} is very sensitive to the location of the source. If the source is in the crust the maximum amplitude of PL may be three or four times the amplitude of the first Pn pulse. For sources below the crust the PL amplitude decreases with increasing depth. More correctly, the PL which is coupled with the P waves decreases; the PL coupled with shear waves increases. The net effect is that the PL moves back into the record, finally arriving after the S arrival (see *Frazier*, 1976, for more on shear coupled PL).

The use of synthetic seismograms to model body waves has been exploited to increase our knowledge of both the seismic source process and the earth's structure. The procedures for teleseismic ($>30^\circ$) modeling methods are outlined by *Fukao* (1971), *Helmberger* (1974), and *Langston and Helmberger* (1975), among others. Similar techniques have been applied to upper mantle distance (14° to 30°) records (*Wiggins and Helmberger*, 1973; *Burdick and Helmberger*, 1978; *McMechan*, 1979; to name a few). The purpose of this study is to develop procedures for modeling P_{nl} and approximations which are useful in solving inverse problems for structure and the seismic source. Although the previous work on PL is formulated in terms of modes we have chosen to model P_{nl} with generalized rays. The reason for this is two-fold; (1) the ability to trace or suppress individual rays (thus

gaining physical insight), and (2) the ability to put in laterally varying structure such as a dipping Moho. *Helmberger and Engen* (1980) have shown that a simple layer (crust) over a half space (mantle) is a sufficient structural model to simulate P_{nd} in the period range of 5 to 40 seconds. Even with this simple model the conventional procedures for calculating synthetic seismograms in this distance range is expensive due to the large number of rays which must be summed and any systematic modeling of a large data set would be prohibitive. We will present a series of approximations to generalized ray theory which significantly reduce the cost of generating synthetics for crustal waveguides.

1.2 EVALUATION OF THE SYNTHETIC RESPONSE

We use the Cagniard-de Hoop technique to obtain the transient response for a generalized ray from a point shear dislocation in a layered stack. This technique was first applied to problems of seismological interest by *Pekeris et al.* (1965), and later refined by *Helmberger* (1968) to the form we start with. Since the problem of interest involves travel times which are very long compared to source duration, a logical starting point is the high frequency solution for the scalar potential (in cylindrical coordinates) for a given ray:

$$\Phi(r, z, t) = \dot{f}(t) * \frac{1}{\sqrt{t}} * \Psi(t) \quad (1.1)$$

$$\Psi(t) = \frac{1}{\pi} \sqrt{\frac{2}{r}} \operatorname{Im} \left[\prod_i R_i(p) \frac{\sqrt{p}}{\eta_1} \frac{dp}{dt} \right]_{\Gamma}$$

where

$f(t)$ = far field time history

p = ray parameter which is function of time

$$\eta_i = \left(\frac{1}{v_i^2} - p^2 \right)^{1/2}$$

$\prod_i R(p)_i$ = the product sum of the complex plane wave reflection coefficients

τ = range

Γ = the de Hoop contour

The geometry of the problem is specified in Figure 1-2 (we will restrict ourselves to the case where the source is in the crustal waveguide). To construct an adequate synthetic displacement response for a waveguide problem, an equation of the form (1.1) must be evaluated and summed for a large number of rays (see *Helmburger and Engen, 1980*). This is usually a tedious and expensive proposition. By simplifying (1.1) with a series of approximations the computational time can be significantly reduced.

The solution of (1.1) depends on the evaluation of the imaginary part of $\Psi(t)$ along the de Hoop contour. For a given ray, the travel time as a function of p is written:

$$t(p) = pr + \sum_{i=1}^N th_i \eta_i \quad (1.2)$$

where th_i is the vertical thickness of layer i which the ray travels through with velocity v_i . The values of p in (1.2) must make $t(p)$ real and increasing, so the contour defined by (1.2) leaves the real axis at some p_0 such that $\frac{dt}{dp}(p_0) = 0$, corresponding to the arrival time of the geometric arrival. Figure 1-3 is a typical contour for the structure in Figure 1-2. Since τ is large compared to the waveguide thickness, p_0 is greater than $\frac{1}{\alpha_2}$, (denoted p_c in Figure 1-3) and a headwave is present (the first

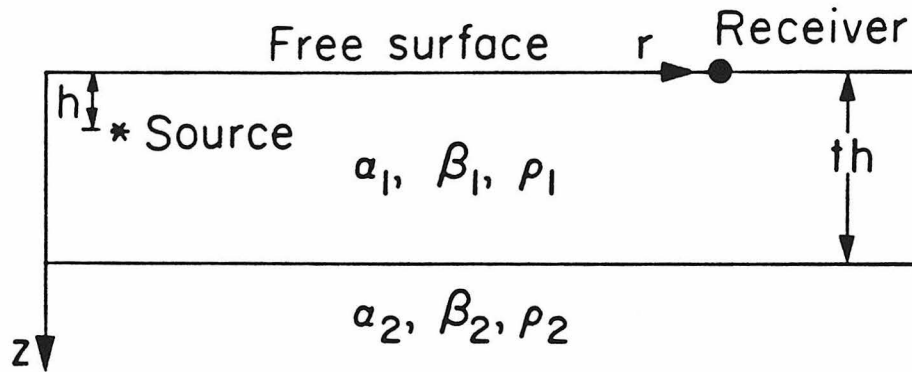


Figure 1-2: Source and receiver geometry.

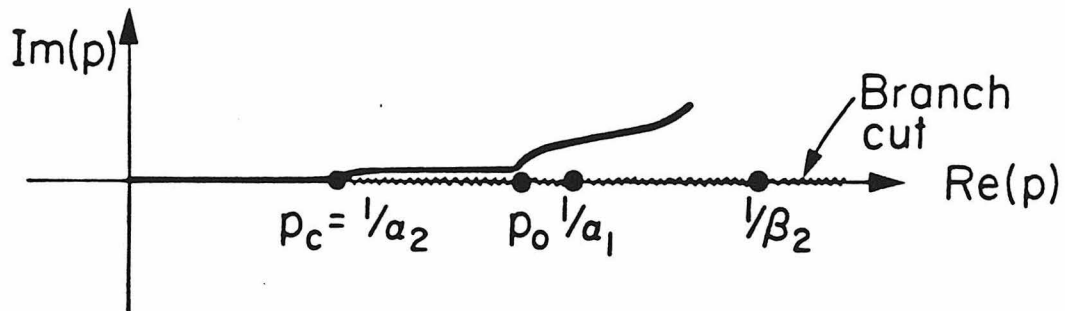


Figure 1-3: The complex p plane for a ray in the structure given in Figure 1-2. The de-Hoop contour is shown with the heavy line. There is a branch cut at p_c and runs along the real p axis.

arrival). If the generalized ray of interest has legs which travel at different velocities, such as would be the case when a converted phase is present (for example, leaves the source as an SV wave and is reflected off the free surface as a P wave), then the η 's of differing velocities are involved and the inversion of (1.2) is not analytic. In this case, the conventional approach is to find the contour numerically.

In the problem of the crustal waveguide over the mantle the poles along the real axis of p are well separated and the behavior of the contour before the arrival of the Rayleigh wave is smooth and predictable. The behavior of p in the vicinity of p_0 is, to first order, only influenced by α_1 . This allows us to approximate $t(p)$ such that $p(t)$ can be found analytically. We can rewrite (1.2) by considering all the "legs" of a ray which travel at velocities less than α_1 as time delay term $F(p)$:

$$t(p) = pr + \eta_{\alpha_1} th_{\alpha_1} + F(p) \quad (1.3)$$

where th_{α_1} is the total vertical distance traveled as a P wave. $F(p)$ can be expanded in Taylor series about p_0 ;

$$F(p) \approx F(p_0) + (p - p_0) \frac{dF}{dp}(p_0)$$

Rearranging the terms independent of p and the functions of p in (1.3) yields:

$$\tau(p) = p \hat{r} + \eta_{\alpha_1} th_{\alpha_1} \quad (1.4)$$

which, of course, can be inverted analytically:

$$p(t) = \frac{\hat{r}}{R^2} \tau \pm i \left[\tau^2 - \frac{R^2}{\alpha_1^2} \right]^{\frac{1}{2}} \frac{(th_{\alpha_1})}{R^2} \quad (1.5)$$

where

$$\tau = t - \sum_{i=1}^N \eta_i(p_0) t h_i + \sum \frac{p_0^2}{\eta_i}$$

$$\hat{r} = \tau - \sum_{i=1}^N \frac{p_0}{\eta_i(p_0)} t h_i$$

The use of the analytic contour simplifies the evaluation of the potential. As a test of the effect of the approximate contour on waveform we consider several examples. The first case is a ray which has several mode changes along its path. Figure 1-4 diagrams the ray path and shows a comparison of the displacement responses computed with the analytic contour and the iterative (exact) contour. Both synthetics have been convolved with a long-period WWSSN (15-100) instrument and a trapezoidal time function ($\delta t_1 = \delta t_2 = \delta t_3 = 1$ second). The instrument and time function are representative of the type of data we would like to model (moderate size earthquakes), so all further examples will be similarly filtered. Both the amplitude and waveform are fairly well matched in Figure 1-4a. A more severe test is to have the ray travel all but one of its legs as SV. Such a ray is shown in Figure 1-4b. Also shown in 1-4b is a comparison between the two different contour displacements. Most studies of continental crust have found that the velocities in the upper few kilometers are much slower than the average for the whole crust. This type of structural problem is an excellent test of the analytic contour. In Figure 1-5, the waveguide is divided into two layers where the top layer has a lower velocity than the bottom layer. The portions of the ray path in the upper layers are then a time delay. Also in Figure 1-5 is the comparison of waveforms, and as before the amplitude and waveforms are nearly identical.

In the simple waveguide problem each ray is basically two arrivals; a headwave and a reflected arrival. The step function response for the ray in Figure 1-4a is shown in Figure 1-6. the response is smooth except at the arrival time of the headwave

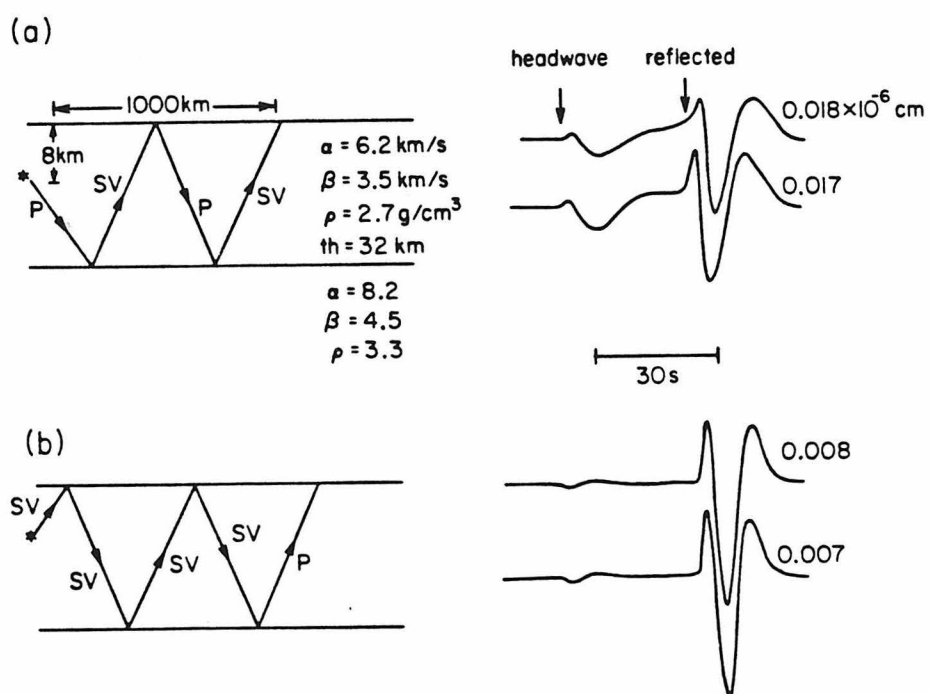


Figure 1-4: (a) A comparison between the waveforms of a synthetic computed with the exact (top trace) and approximate contour at a distance of 1000 km. The synthetics have been convolved with a WWSSN 15-100 instrument and a trapezoidal time function. The structure and ray description is shown to the left. (b) A comparison of the waveforms for a synthetic computed with the exact (top trace) and approximate contour at a distance of 1000 km. The structure and ray description are shown to the left.

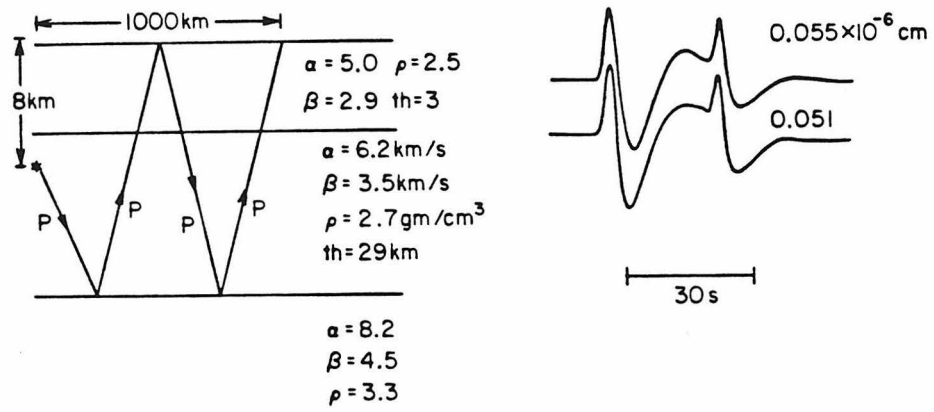


Figure 1-5: A comparison of the waveforms for a synthetic computed with the exact (top trace) and approximate contour at 1000 km. The two layered crustal model and ray description are shown to the left.

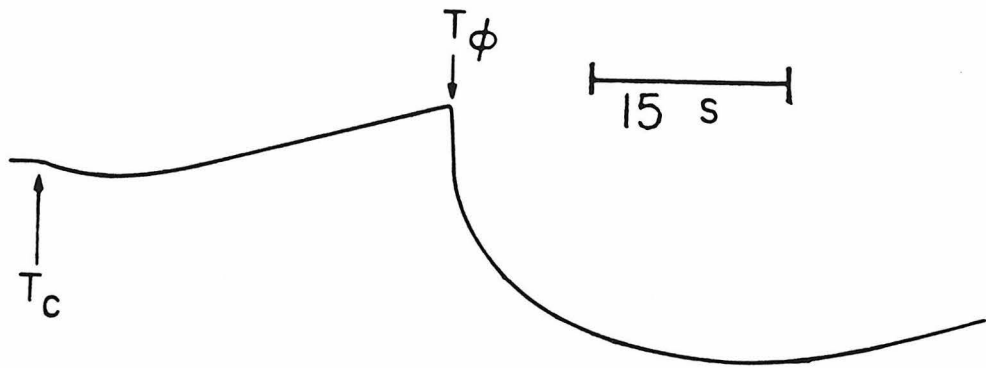


Figure 1-6: Step function response for the ray and structure in Figure 1-4a.

(t_c) and the reflected arrival (t_o). This suggests that the potential only need be evaluated at a few points around t_c and t_o and interpolated in between. The analytic contour allows the potential to be evaluated as a simple function of time; we have found that it is sufficient to describe the response of each ray with just 15 time points when dealing with frequencies in the pass band of a 15-100 instrument.

To produce a reliable synthetic P_{nl} requires summing multiples until the response is stable. *Helmberger and Engen (1980)* have shown that rays which bounce more than 3 times off the Moho do not affect the long-period response; taking advantage of kinematic redundancies, a reliable synthetic still requires over 250 rays. Figure 1-7 shows a comparison of P_{nl} synthetics for the vertical displacement response of the three fundamental faults (all fault orientations can be reduced to a linear combination of these three faults) computed for the analytic contour and 15 points per ray with that computed with the exact contour and approximately 50 points per ray. The relationship of the step function response of the fundamental faults and the potential amounts to putting in the vertical radiation pattern and receiver function. For example, the vertical response of the fundamental faults is given by:

$$W_j = \frac{1}{\pi} \sqrt{\frac{2}{r}} * \frac{1}{\sqrt{t}} * \left[\sum_{i=1}^N \text{Im} \left[\Pi_i R_i(p) \frac{\sqrt{p}}{\eta_\alpha} C_j(p) R_{NZ}(p) \frac{dp}{dt} \right] \right. \quad (1.6)$$

$$\left. + \sum_{i=1}^N \text{Im} \left[\Pi_i R_i(p) \frac{\sqrt{p}}{\eta_\beta} SV_j(p) R_{NZ}(p) \frac{dp}{dt} \right] \right]$$

where R_{NZ} is the receiver function, which is defined by either R_{pz} or R_{sz} depending on the mode of propagation upon arrival at the receiver;

$$R_{pz} = \frac{2\eta_\alpha(\eta_\beta^2 - p^2)}{\beta^2 R(p)} \quad (1.7)$$

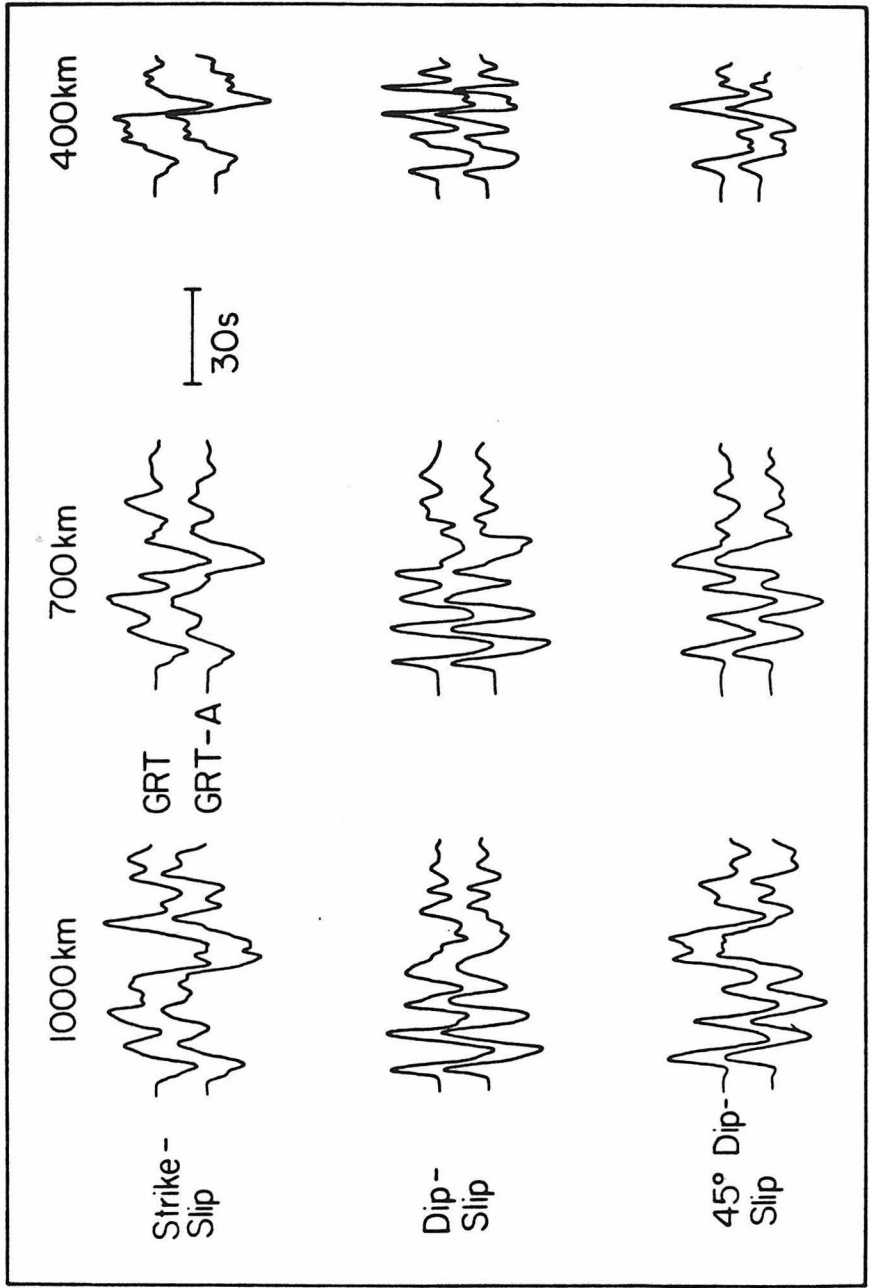


Figure 1-7: Comparison of the P_n waveforms for the three fundamental faults computed with the exact contour and 50 points per ray (GRT) and those computed with the approximate contour and 15 points per ray. The displacements have been convolved with a 15-100 instrument and a trapezoidal time function.

$$R_{sz} = \frac{\eta_\alpha \eta_\beta}{\beta^2 R(p)}$$

$$R(p) = (\eta_\beta^2 - p^2)^2 + 4p^2 \eta_\alpha \eta_\beta$$

The vertical radiation patterns are given by:

$$C_1 = -p^2 \quad SV_1 = -\varepsilon p \eta_\beta \quad (1.8)$$

$$C_2 = 2\varepsilon p \eta_\alpha \quad SV_2 = (\eta_\beta^2 - p^2)$$

$$C_3 = (p^2 - 2\eta_\alpha^2) \quad SV_3 = 3\varepsilon p \eta_\beta$$

$\varepsilon = +1$ if ray is upgoing
 $= -1$ if ray is downgoing

Three different ranges are shown in Figure 1-7; the agreement between the two techniques is good in both amplitude and waveform. Where disagreement occurs is only in the high frequency part of PL. The difference in computation time is about a factor of eight.

1.3 CHANGES IN MODEL PARAMETERS

One disadvantage of generalized rays is that even small changes in the structural model require that the entire synthetic be regenerated. If one is trying to fit a large set of observations this process is very time consuming. Various authors (*Mellman*, 1980; *Given*, 1983) have developed iterative inversion techniques to determine model perturbations, but the regeneration of the synthetics would be prohibitively expensive for regional distance seismograms. Fortunately, the simplicity of individual rays in P_{nl} allows us to map the changes in waveform as a function of

model change. Since each ray is basically a headwave and a reflected arrival the time separation between t_c and t_o is the parameter most strongly dependent on structure. In general, it is possible to "stretch" or "squeeze" the P_{nl} waveform of a representative model to simulate a small perturbation in structure.

The four parameters which influence the P_{nl} waveform are; (1) crustal thickness, (2) mean crustal P velocity, (3) mean crustal Poisson's ratio, and (4) the Pn velocity. Of these, crustal thickness shows the largest lateral variation. Figure 1-8 shows the displacements for a ray which bounces in the crust as a function of crustal thickness. In this case, as thickness increases the separation of t_c and t_o decreases (this is because the change in travel time is a function of $\eta_i \Delta th$ and $\eta(p_c)$ is much larger than $\eta(p_o)$). There is very little difference in waveform between the 29 km crust and the 37 km crust. In fact, the 29 km waveform is simply a "stretched" version of the 37 km waveform. Although the maximum amplitudes decrease by 15 per cent for the suite of thicknesses shown, the ratio of the Pn amplitude to the reflected wave amplitude does not change by more than a few per cent (each waveform in Figure 1-8 is normalized to the reflected wave amplitude). Certainly, given any of the waveforms it would be possible to predict the others. This type of stretching and squeezing can be applied to each of the rays in a P_{nl} response. Since the response is calculated at only 15 points it can be stored as a vector along with p_o , t_o , p_c , and t_c . Then, for any new structure the travel times of the headwave and reflected wave can be recalculated and the timing of the vector can be adjusted accordingly. Figure 1-9 shows the P_{nl} displacements at a range of 1000 km for the three fundamental faults for two different crustal thicknesses (the velocities for the model are given in Figure 1-4). The differences between the two structure's waveforms is most obvious in the case of the 90° dip-slip fault (this fault

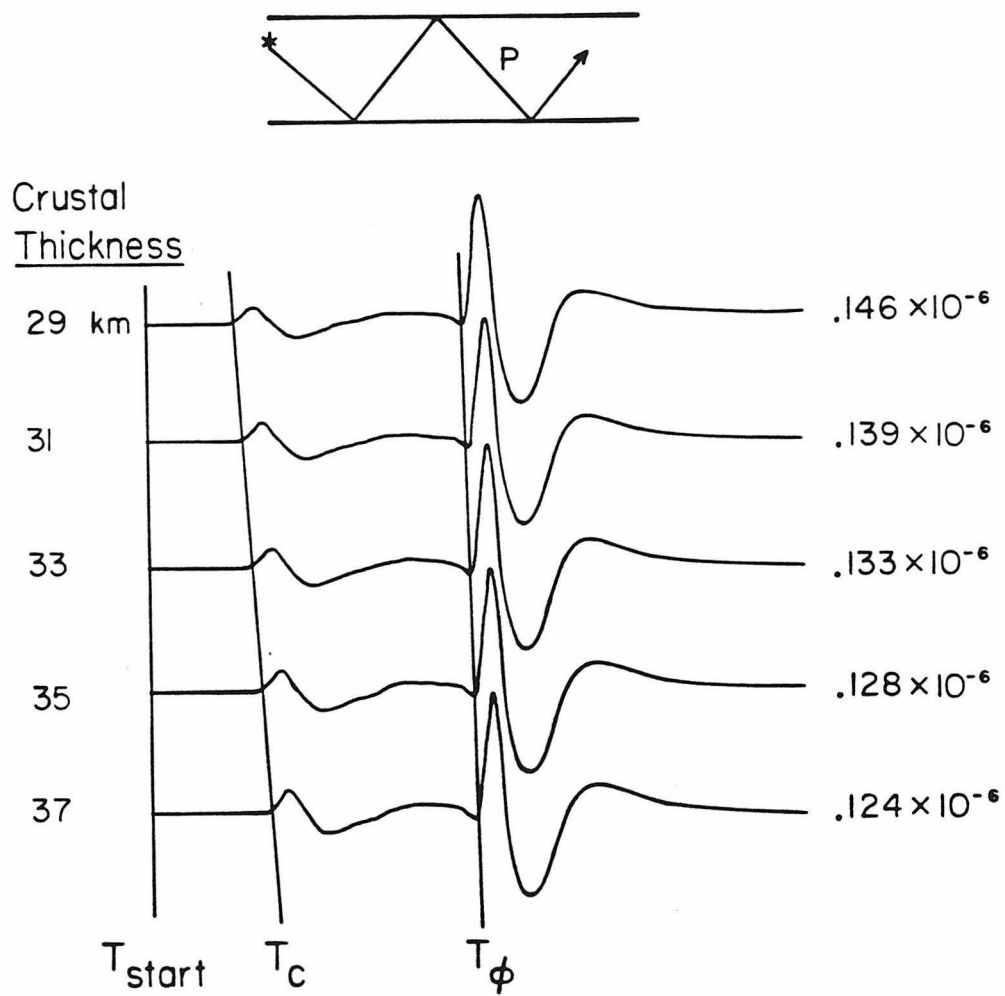


Figure 1-8: The effect of a change in crustal thickness on the waveform for the ray shown above. The distance is 1000 km, and the velocities are given in Figure 1-4.

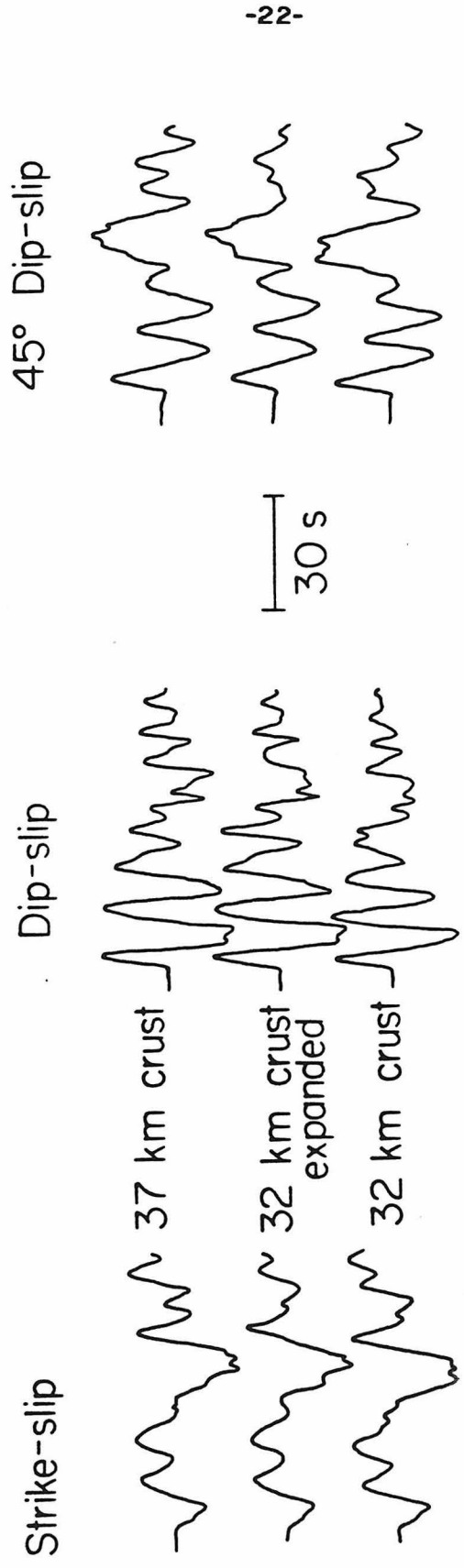


Figure 1-9: A comparison between the P_{n1} waveforms for a 37 km and 32 km thick crust at 1000 km. Also shown is a simulation of the 37 km crust.

orientation gives the highest frequency excitation). In general, the waveform from the thinner crust is less disperse. Also shown is a simulated 37 km crust generated by stretching the 32 km response. The stretched P_{sl} waveform is a good approximation of the actual synthetic for the thicker crust. Even details such as the interference pattern in the first down swing of the dip-slip response is preserved. The seismograms in Figure 1-9 are all normalized to their maximum amplitude.

The same exercise can be carried out for the other structural parameters. Figure 1-10 shows the displacements for two different Pn velocities (the crust is the same as in Figure 1-4). The higher Pn velocity stretches the waveform between Pn and PL. Shown between the pairs of waveforms in Figure 1-10 is an 8.2 km/sec waveform which has been compressed to simulate the slower Pn velocity of 7.8 km/sec. The change in reflection coefficient has only a small effect on the waveform shape.

Adjusting a "master" Green's function to account for changes in mean crustal P velocity or Poisson's ratio are not as easy as for the parameters discussed previously. This is because in addition to timing changes the receiver function and vertical radiation coefficient also change (see the dependence of the expressions in 1.5 and 1.6 on both α and β of the crust). Although the changes in both receiver function and radiation coefficient are small for small changes in velocity, they also depend on the ray parameter. Therefore, the relative amplitude of the headwave and the reflected arrival changes. It has been found that if the changes in velocity are limited to the order of 5 per cent the waveforms retain enough character to be useful. Figure 1-11 shows a comparison of waveforms for two different mean crustal P velocities (Poisson's ratio is constant 0.27). In between the two synthetics is a simulation of the slower velocity determined from the faster crust. Although the

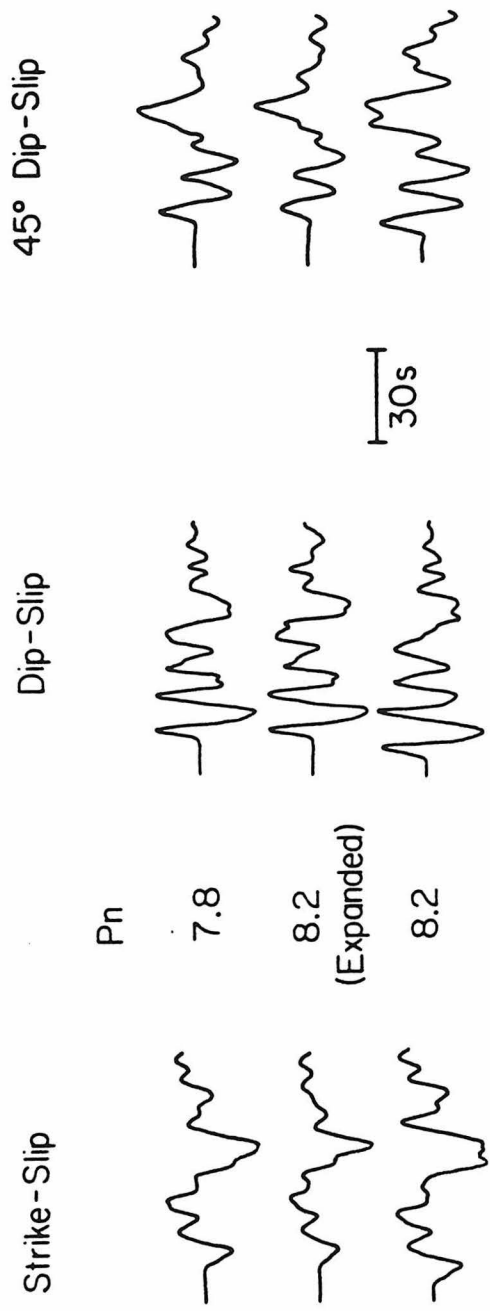


Figure 1-10: A comparison between the P_n waveforms for a 8.2 km/sec and a 7.8 km/sec Moho at 1000 km. Also shown is a simulation of the lower Pn velocity by compressing the 8.2 km/sec synthetic.

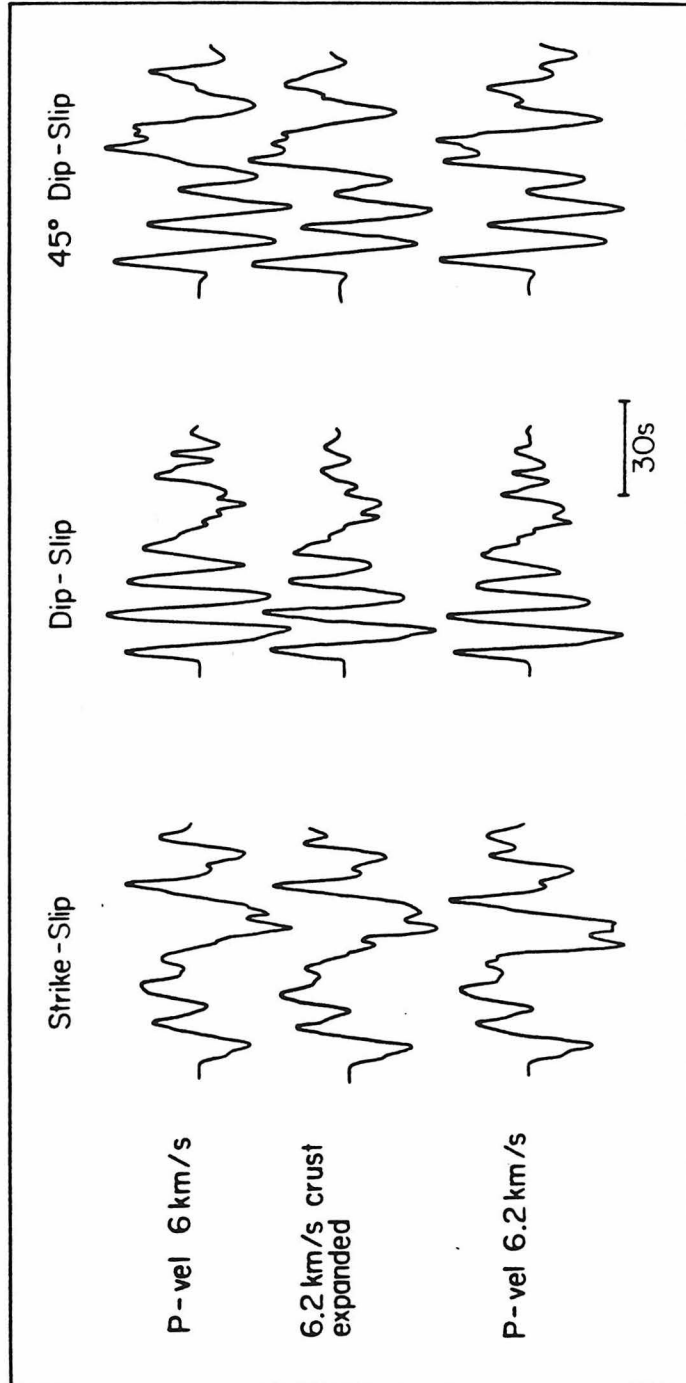


Figure 1-11: A comparison between the $P_{\pi i}$ waveforms for a crustal P velocity of 6.0 and 6.2 km/sec at 1000 km. Also shown is a simulation of the lower P velocity crust.

waveform fit is acceptable, the Pn to PL ratio is worse than the previously discussed examples. A change in crustal thickness has much the same effect as changing mean crustal velocity; the timing of the reflected arrivals is affected to the largest extent. Figure 1-12 shows a comparison for different mean crustal Poisson's ratios. The simulated waveform fit is the same quality as in the previous comparison.

1.4 DISCUSSION

It would seem rather amazing that such a simple model of a plane layer crust over a halfspace mantle would account for the character of observed P_{nl} . Figure 1-13 shows a profile of the P_{nl} of a moderate size earthquake (Sept. 12, 1966 at Truckee, California, $m_b = 5.7$) and a profile of synthetics. The earthquake is a pure strike-slip event so we can compare directly with the strike-slip fundamental fault response (the observed records have been corrected for radiation pattern). There are some differences between the observed and synthetics, but it is mainly at high frequencies, and in general the fit is quite good. The question is "why does it fit so well?" Most continental crustal structure models have at least three distinct layers; (1) a layer at the surface which is 2 to 10 km thick with P velocities between 5.5 and 6.0 km/sec, (2) the bulk of the crust which typically has velocities between 6.0 and 6.4 km/sec and (3) a layer below the Conrad surface at depths of 20 to 28 km with velocities between 6.7 and 7.2 km/sec (for a summary of crustal structures in the western U. S. see *Hill*, 1978; in Europe see *Sollogub*, 1969). An average of the vertical velocity is typically 6.2 to 6.4 km/sec, which is what we use as the P velocity of the entire crust. Since the boundaries between the upper two layers is gradual it has a limited effect on waveform at periods of 5 seconds or greater. On the other hand, the Conrad is a sharper boundary. *Langston* (1982) has studied the

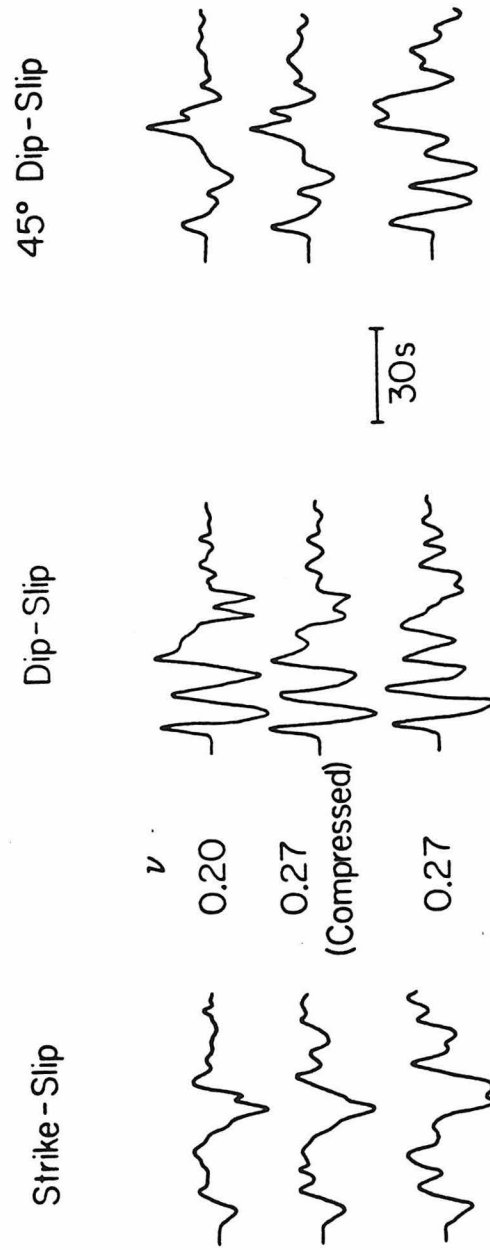


Figure 1-12: A comparison between the P_n waveforms for a crustal Poisson's ratio of 0.2 and 0.27 at 1000 km. Also shown is a simulation of the lower Poisson's ratio crust.

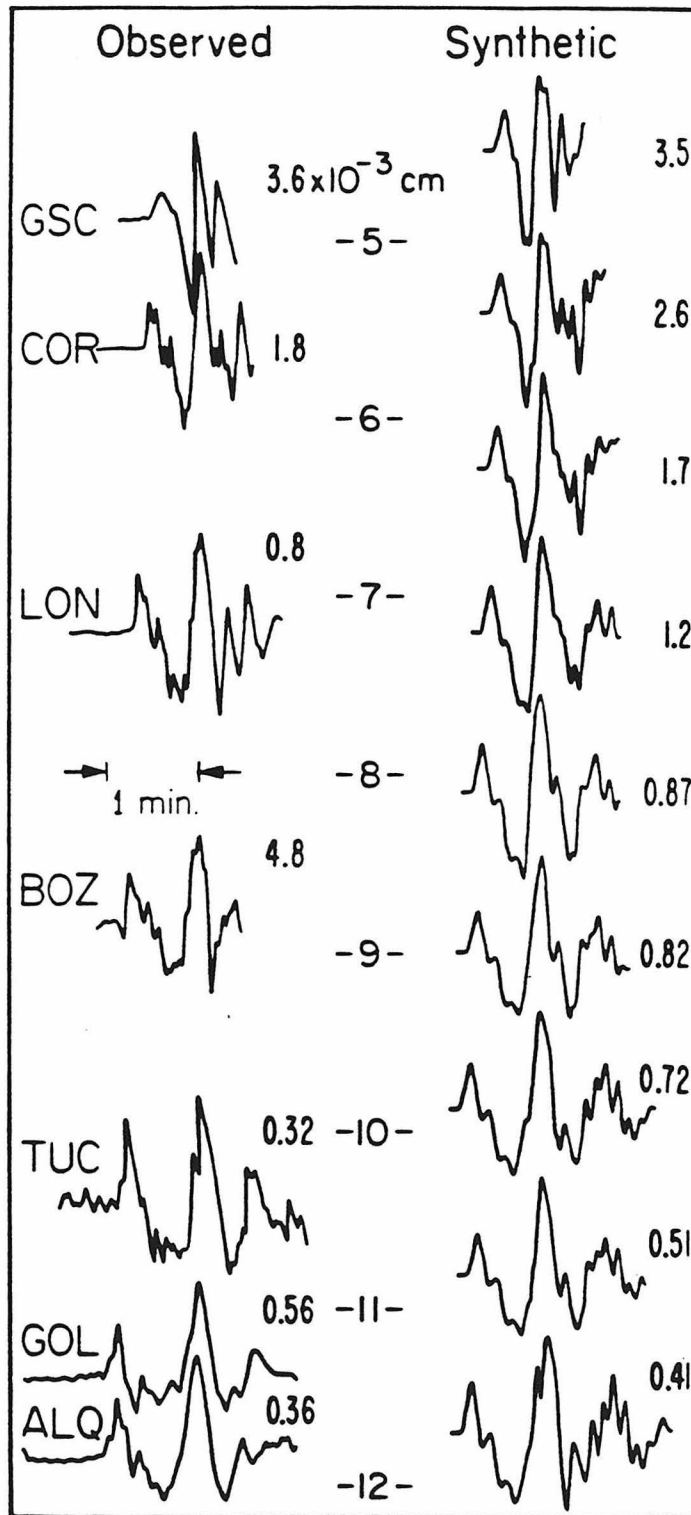


Figure 1-13: Truckee earthquake waveforms corrected for horizontal radiation pattern and plotted as a function of distance. The maximum amplitude is shown to the right of each trace. Note that the stations BOZ and TUC are very close to nodes.

short-period synthetics from such a two layered crust. The layering gives rise to two groups of arrivals; (1) P_g , which are multiples in the upper layer, and (2) P^* , which are post critical reflections within the lower crustal layer. At long periods there is no clear separation of phases. Figure 1-14 shows a comparison of long-period P_{nl} synthetics for a two layered crust with the single layer crust synthetics (the crustal models are also shown in the Figure). The velocity used in the single layer crust is an average of the vertical velocity in the two layered crust. There is very little difference between the two suites of synthetics; as long as the Conrad is not too thick or the velocity jump too great it is apparent that the one layered synthetics are sufficient. An extension of the two layered crust is to consider a Moho which is not sharp, but rather a transition layer. *Helmberger and Engen (1980)* examined the behavior of the reflection coefficients R_{pp} , R_{ps} and R_{sp} for various crust mantle boundaries and found that adding a transition layer up to 10 km does not drastically alter the long period behavior at post-critical angles. This is further supported by numerical experiments done by *Shaw and Orcutt (1979)*.

Another assumption which appears questionable is that of a flat Moho. Almost all crustal structures derived from short-period refraction experiments have the Moho changing character over a fairly short scale length; on the order of 50 to 100 km. This short scale length is apparently important, because no one crustal section dominates the long-period waveform. The timing of the sum of rays is a product of the "average" of the different crustal sections, hence the "average" crustal model used in the generation of the synthetics is sufficient. If the Moho is allowed to have a uniform dip over long ranges then the P_{nl} waveform begins to show significant differences from those of a flat Moho. Figure 1-15 documents these differences.

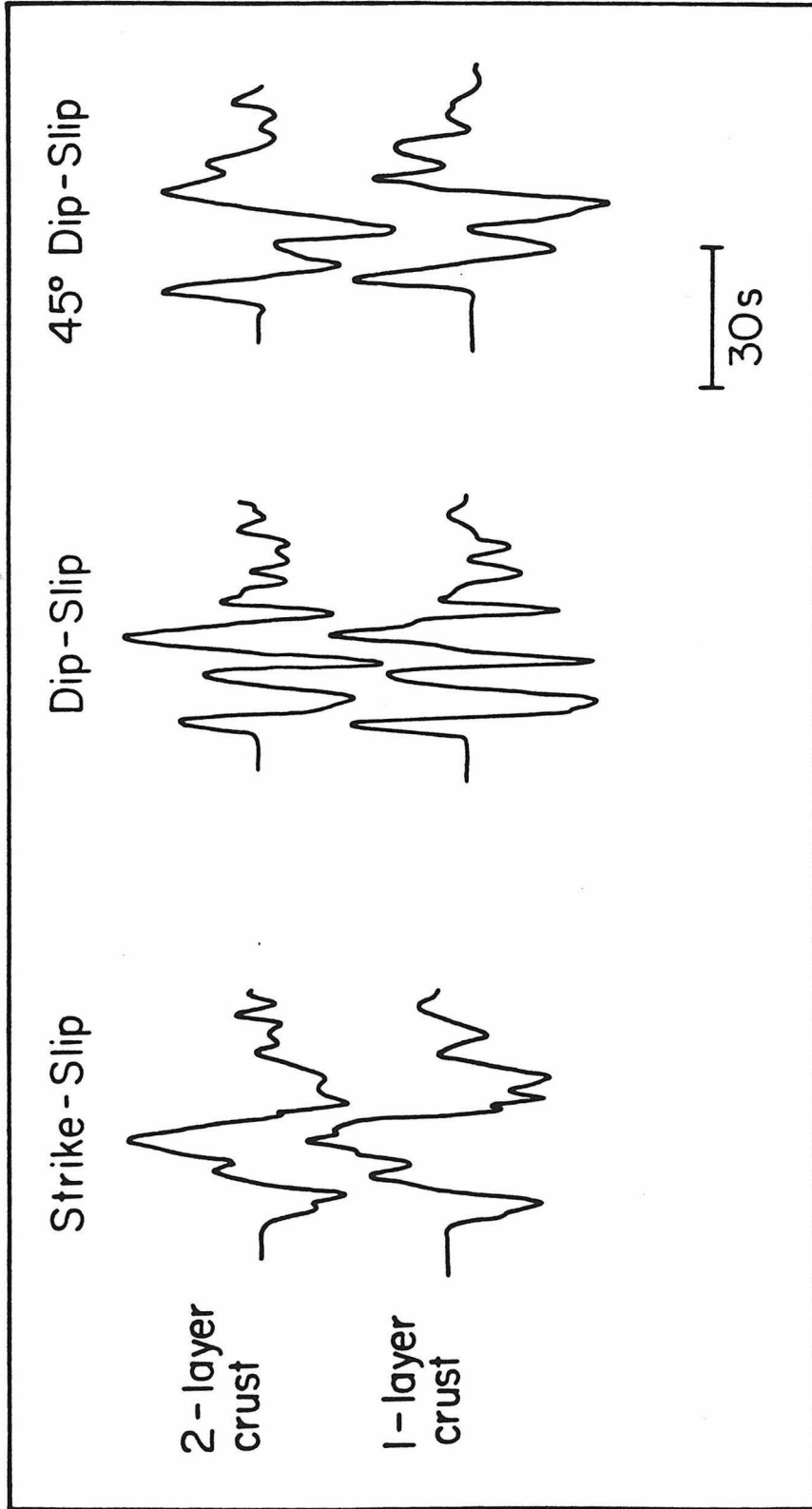


Figure 1-14: A comparison between the P_{nl} synthetics computed for a 1-layer and a 2-layer crust. Poisson's ratio is constant, and the P velocity is the 1-layer model is the average of the 2-layer model.

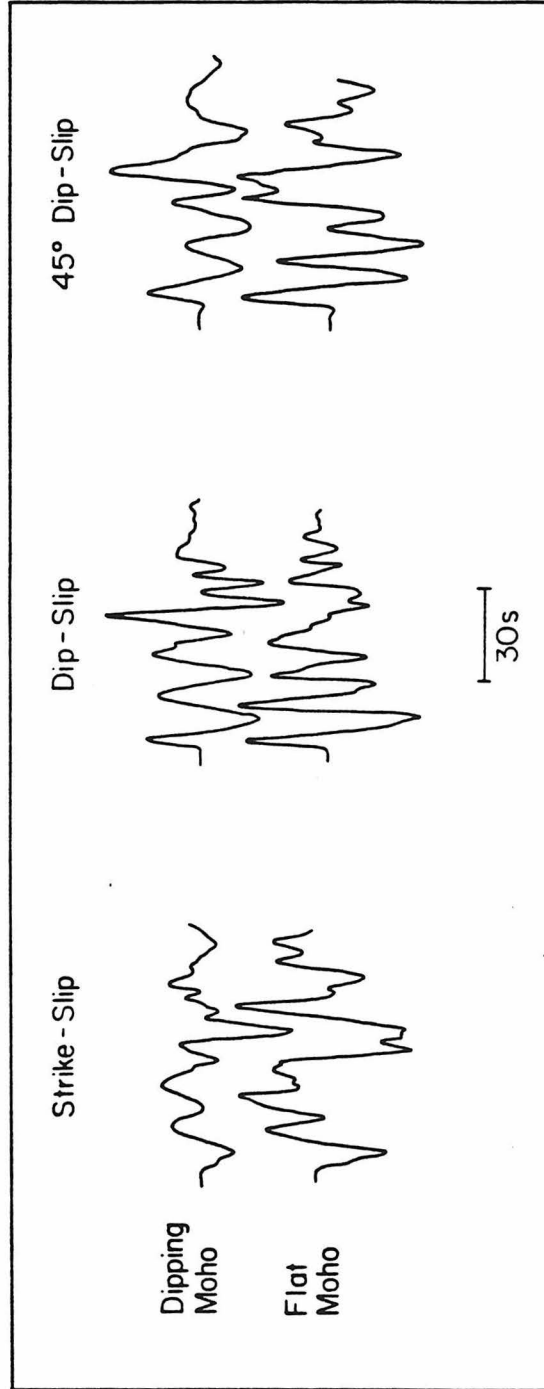


Figure 1-15: A comparison between the P_n synthetic computed for a dipping Moho and a flat Moho. The crustal thickness is 28 km at the source and 50 km at the receiver for the dipping model. The flat Moho model has a crustal thickness of 39 km, which is the average of the dipping structure.

The assumption of a halfspace mantle must break down at some point; at some distance a significant amount of energy will be present in the form of diving rays which have turned in the mantle. These diving rays will affect the ratio of the Pn to PL amplitudes. If there are significant gradients in the upper mantle the first arrival is sharper and larger amplitude than Pn. In Figure 1-13 the numbers to the right of each trace are amplitudes (the earthquake observations have been corrected for moment and azimuthal radiation pattern). There does not appear to be a systematic break-down in waveform shape or amplitude over the distance range of 4° - 12° . The stations at BOZ and TUC are nearly nodal, and thus their recording of amplitude are not particularly reliable. The assumption of a halfspace mantle, at least in the western U. S. is in agreement with the work of *Hill* (1971) which showed that the velocity gradients at the refracting horizon have a profound effect on the amplitude of headwaves. One can infer from *Hill's* work that the upper-most mantle in the western U. S. can be characterized with zero or negative gradients.

If the gradients in the upper mantle are positive, which is probably the case for regions such as the eastern U. S. and the Canadian shield, we can show the approximate effect on P_{nl} with a simple model. Rather than a halfspace mantle we consider a two layer system; the second layer is 100 km below the Moho and has a velocity jump of 0.1 km/sec. Figure 1-16 shows a comparison between a profile of synthetics for the two layered and halfspace mantles (the time function used is a trapezoid with $\delta t_1 = \delta t_2 = \delta t_3 = 0.5$ seconds). The waveforms begin to diverge between 900 and 1000 km, and the differences are quite pronounced at 1400 km. Note that the PL waveform does not change shape or amplitude between the two models, rather the relative importance of the first arrivals changes. The diving ray sharpens what would be interpreted as the Pn arrival. The gradient that is simulated with the two

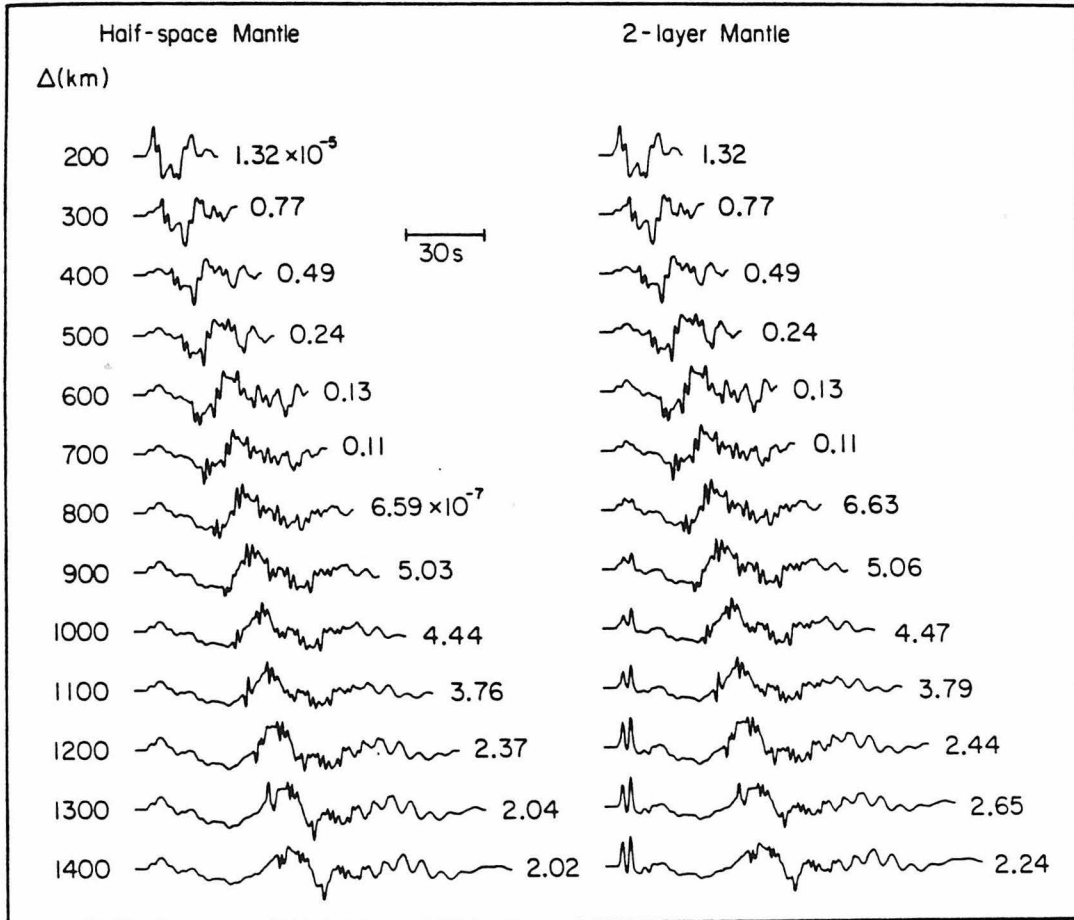


Figure 1-16: Profiles of the P_{nl} waveforms for a 1-layer and 2-layer mantle.

layered model corresponds to what would be predicted for very stable tectonic provinces; for example, for *Given* and *Helmberger's* (1980) K8, which is for northwestern Eurasia, the change in velocity would be .104 km/sec. Most models for tectonically active provinces have low velocity zones (see *Burdick* and *Helmberger*, 1978; *Walck*, 1983), and therefore negative gradients. A prudent approach to using the halfspace mantle P_{nl} synthetics would be distances less than 10° in shields and platforms, and out to 12° in more tectonically active provinces.

Within the constraints outlined in the preceding discussion P_{nl} can be modeled with a single layer over a halfspace. A big benefit of using such a simple model is that a single Green's function can be used to investigate a whole suite of structural models. Since small changes in structure are expressed in terms of timing of different rays, the partial derivatives of the waveform with respect to the different structural parameters can be easily calculated. This would be particularly useful for crustal structure studies; if the source orientation is fixed, the P_{nl} could be inverted for structure.

CONCLUSIONS

The long-period P_{nl} waveforms from many shallow continental earthquakes can be modeled with a layer over a halfspace. We have demonstrated that generalized ray theory and the Cagniard-de Hoop technique can be streamlined for this problem. An analytic contour simplifies the computation. The simplicity of the individual ray involved requires that the potential need only be evaluated at a small number of points. Therefore, not only is the computation process efficient, but a single Green's function can be used for a whole suite of models.

REFERENCES

- Burdick, L.J and D.V. Helmberger (1978). The upper mantle P-velocity structure of the western United States, *J. Geophys. Res.*, 83, 1699-1712.
- Fukao, Y. (1971). Seismic body waves for surface faults, *J. Phys. Earth*, 19, 271-281.
- Gilbert, F. and S.J. Laster (1962). Experimental investigations of PL modes in a single layer, *Bull. seismo. Soc. Am.*, 52, 59-66.
- Given, J.W. (1983). Inversion of seismic body waves for structure (in preparation).
- Given, J.W. and D.V. Helmberger (1980). Upper mantle structure of northwestern Eurasia, *J. Geophys. Res.*, 85, 7183-7194.
- Helmberger D.V. (1968). The crust mantle transition in the Bering Sea, *Bull. seismo. Soc. Am.*, 58, 179-214.
- Helmberger, D.V. (1974). Generalized ray theory for shear dislocations, *Bull. seismo. Soc. Am.*, 64, 45-64.
- Helmberger, D.V. and G.R. Engen (1980). Modeling the long-period body waves from shallow earthquakes at regional ranges, *Bull. seismo. Soc. Am.*, 70, 1699-1714.
- Hill, D.P. (1971). Velocity gradients and anelasticity for crustal body wave amplitudes, *J. Geophys. Res.*, 76, 3309-3325.
- Hill, D.P. (1978). Seismic evidence for the structure and Cenozoic tectonics of the Pacific Coast States, in *Cenozoic Tectonic and Regional Geophysics of the Western Cordillera*, **Geol. Soc. Am. Memoir 152** , R.B Smith and G.P Eaton,

- editors, 145-174.
- Langston, C.A. (1982). Aspects of Pn and Pg propagation at regional distances, *Bull. seismo. Soc. Am.*, 72, 457-472.
- Langston, C.A. and D.V. Helmberger (1975). A procedure for modeling shallow dislocations, *Geophys. J.*, 42, 117-130.
- McMechin, G. (1979). An amplitude constrained P-wave velocity profile for the upper mantle beneath the eastern United States, *Bull. seismo. Soc. Am.*, 69, 1733-1744.
- Mellman, G.R. (1980). A method of body-wave waveform inversion for the determination of earth structure, *Geophys. J.*, 62, 481-504.
- Oliver, J. (1964). Propagation of PL waves across the United States, *Bull. seismo. Soc. Am.*, 54, 151-160.
- Oliver, J. and M. Major (1960). Leaking mode and the PL phase, *Bull. seismo. Soc. Am.*, 50, 165-180.
- Pekeris, D.L., Z. Alterman, F. Abvamosvici and H. Jarosch (1965). Propagation of a compressional pulse in a layered solid, *Reviews of Geophys.*, 3, 25-47.
- Phinney, R. (1961). Leaking modes in the crustal wave-guide. 1. The Oceanic PL wave, *Bull. seismo. Soc. Am.*, 66, 1445-1467.
- Poupinet, G. (1972). Pl waves and crustal structure in Canada, *Can. J. Earth Sci.*, 9, 1014-1029.
- Rial, J.A. (1976). Seismic-wave transmission across the Caribbean plate: high attenuation on concave side of Lesser Antilles Island arc, *Bull. seismo. Soc. Am.*, 66, 1905-1920.
- Shaw P. and J. Orcutt (1979). The influence of source parameters and crustal structure on PL propagation, *Trans. Am. Geophys. Union*, 60, 895.

Sollogub, V.B. (1969). Seismic crustal studies in southeastern Europe, in *The Earth's Crust and Upper Mantle*, P.J. Hart editor, Am. Geophys. Union, 189-194.

Walck, M.C. (1983). The P-wave upper mantle structure beneath an active spreading center: the Gulf of California, (in preparation).

Wiggins R.A. and D.V. Helmberger (1973). Upper mantle structure of the western United States, *J. Geophys. Res.*, 78, 1870-1884.

Chapter II: The Inversion of Long-Period Regional Body Waves for Source Parameters

2.1 INTRODUCTION

Determining the source parameters of shallow, moderate size earthquakes (in the magnitude range between 5 and 6) is an important problem for several reasons. Earthquakes of this type have widespread geographic occurrence, and in some cases these earthquakes provide the only clue to the active tectonics of a region. The widespread occurrence makes these events desirable sources in crustal structure studies, and they are ideal for studying the upper mantle shear structure since they produce SH waves which are on scale at triplication distances. A considerable amount of effort has been expended to determine the source parameters of this size earthquake, although such determinations can be beset with difficulties. Ideally, a large amount of information can be derived from the modeling of long-period body waves (see *Helmberger, 1974; Langston and Helmberger, 1975*). Unfortunately, if an earthquake is too small to be well recorded teleseismically, which is the case for many events with magnitude less than 6, the fault-plane orientation must be constrained by local short-period data and the seismic moment usually cannot be determined unambiguously. The World Wide Standard Seismograph Network (WWSSN) supplemented by other long-period stations and arrays, provides sufficiently dense coverage in that most moderate-size earthquakes occurring in continental regions will produce some on-scale records of long-period body waves at regional distances. At

these regional distances, 1° - 12° , the waveguide properties of the crust produce complicated body wave signals as discussed in the previous chapter. However, in most cases the long-period waveforms are quite distinctive and sufficiently insensitive to details of the crustal structure to allow the separation of the source and structural information.

In this chapter we present a procedure for extracting the source parameters of moderate-size earthquakes from long-period regional phases (P_{nl}). The procedure involves an iterative inversion technique which minimizes the difference between a synthetic seismogram and the observation. The synthetic waveforms are constructed using Green's functions computed for a single, very simple structure. These Green's functions appear to be an adequate model for most continental regions, thus allowing a quick and approximate determination of fault parameters. The inversion is parameterized in terms of strike, dip and rake. The number of inversion parameters is kept to a minimum so that inadequacies in the Green's functions are not over-emphasized. Obviously, the structural model is more appropriate for certain regions than for others, so the inversion parameters chosen are those which are most robust. The main advantage of this technique is that it requires only a small data set. The general usefulness of this technique is illustrated by inverting regional data for earthquakes occurring in the western U.S., northern Canada and southern Europe.

2.2 THE GREEN'S FUNCTIONS

The basis of the inversion scheme is to be able to accurately fit an observation. This requires that we have a sufficiently accurate structural model so that the Green's functions will contain the desired detail. The techniques for constructing the Green's functions were first discussed by *Helmberger and Engen* (1980), and in a

simplified and more efficient form in the previous chapter. *Helmberger and Engen* (1980) successfully modeled the P_{nl} section of a long-period seismogram with a point shear dislocation in a layer (corresponding to the crust) over a half space (mantle). We have found no need to improve upon this model as long as the pass band of the the observation is on the order of a 15-100 instrument.

The Green's functions are constructed by summing the various contributions of the three fundamental faults. As an example, consider equation (1.4). The Green's function for vertical displacement (in cylindrical coordinates) can be written:

$$w(r, \theta, t) = \left[\frac{M_0}{4\pi\rho} \right] \dot{f}(t) * \sum_{i=1}^3 W_i(t) A_i \quad (2.1)$$

where $\dot{f}(t)$ is the far-field time history of the fault, ρ is the source region density, and M_0 the seismic moment. The W_i are the Green's functions for the fundamental faults: vertical strike-slip, vertical dip-slip, and 45° dip-slip step dislocations. The A_i are coefficients determined by the source orientation and are given by:

$$A_1(\theta, \lambda, \delta) = \sin 2\theta \cos \lambda \sin \delta + \frac{1}{2} \cos 2\theta \sin \lambda \sin 2\delta \quad (2.2)$$

$$A_2(\theta, \lambda, \delta) = \cos \theta \cos \lambda \cos \delta - \sin \theta \sin \lambda \cos 2\delta$$

$$A_3(\theta, \lambda, \delta) = \frac{1}{2} \sin \lambda \sin 2\theta$$

where θ is the receiver azimuth from the end of the fault plane, λ is the rake angle, and δ is the dip angle. The W_i contain the sum of the rays of up to 5 multiples (with kinematic redundancies this corresponds to 492 rays) in the structure given in Table 2-1. An example that these Green's functions are sufficient in predicting the observed P_{nl} is summarized in Figure 2-1. The Figure shows a comparison of the

TABLE 2-1
Crustal Model

P velocity (km/s)	S velocity (km/s)	Density (gm/cc)	Thickness (km)
6.2	3.5	2.7	32.
8.2	4.5	3.4	0.

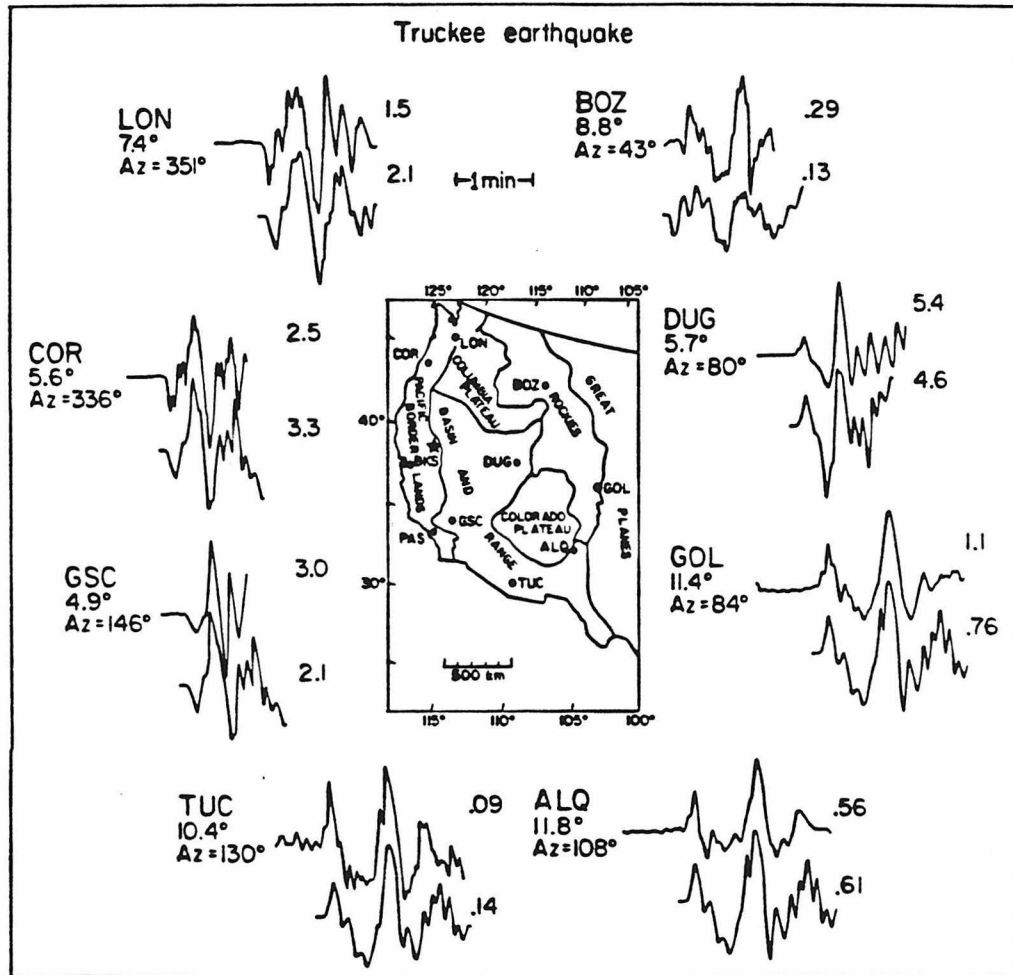


Figure 2-1: Vertical P_n waveforms from the Truckee earthquake. The star denotes the epicenter. The data are the top trace at each station, the trace below is the synthetic fit. The strike-slip mechanism has two nodal planes which project through the stations TUC and BOZ. To the right of each trace is the observed or predicted amplitude (on the basis of a moment of 0.8×10^{25} dyne-cm). in 10^{-3} cm.

synthetic waveforms and the records of the 1966 Truckee, California earthquake (which will be discussed in more detail later). The fault orientation was determined by the inversion of the data shown. In this case, the source time function and moment were determined by other methods, so that the synthetic amplitudes can be viewed as predictions. The numbers on the traces are maximum peak to peak amplitudes. The only noticeable difference between the data and the synthetic waveform is the high frequency content, which can be caused by two factors: (1) the effects of attenuation in the crust have not been added to the synthetic waveforms, and (2) the very sharp boundaries in our model are efficient in trapping short-period energy (the real crust, which is structurally more complicated, probably has smooth boundaries). Overall, the fit of the synthetic waveforms justifies the use of the simple model, and the high frequency content of the synthetic waveforms does not affect our ability to determine the source parameters.

We assume for source parameter studies that the regional observations can be modeled by rounding off the epicentral distance to an even 100 km. Figures 2-2 and 2-3 give the vertical and radial responses for the three fundamental faults for the distances of 500-1400 km. Most earthquakes which produce on-scale P_{nl} at WWSSN stations have similar time functions (which is a reflection of event size). In Figures 2-2 and 2-3 a trapezoid ($\delta t_1 = \delta t_2 = \delta t_3 = 1$ second) is used for the far-field time history. The displacements have also been convolved with the response function for a 15-100 instrument. Because of differences in high frequency content between the data and the synthetic waveforms, the displacement responses have also been filtered. The filter has an impulse response represented by a triangle which has a 2 second rise and fall. When comparing these displacements with data, the observations should be similarly filtered. Once the response for the three

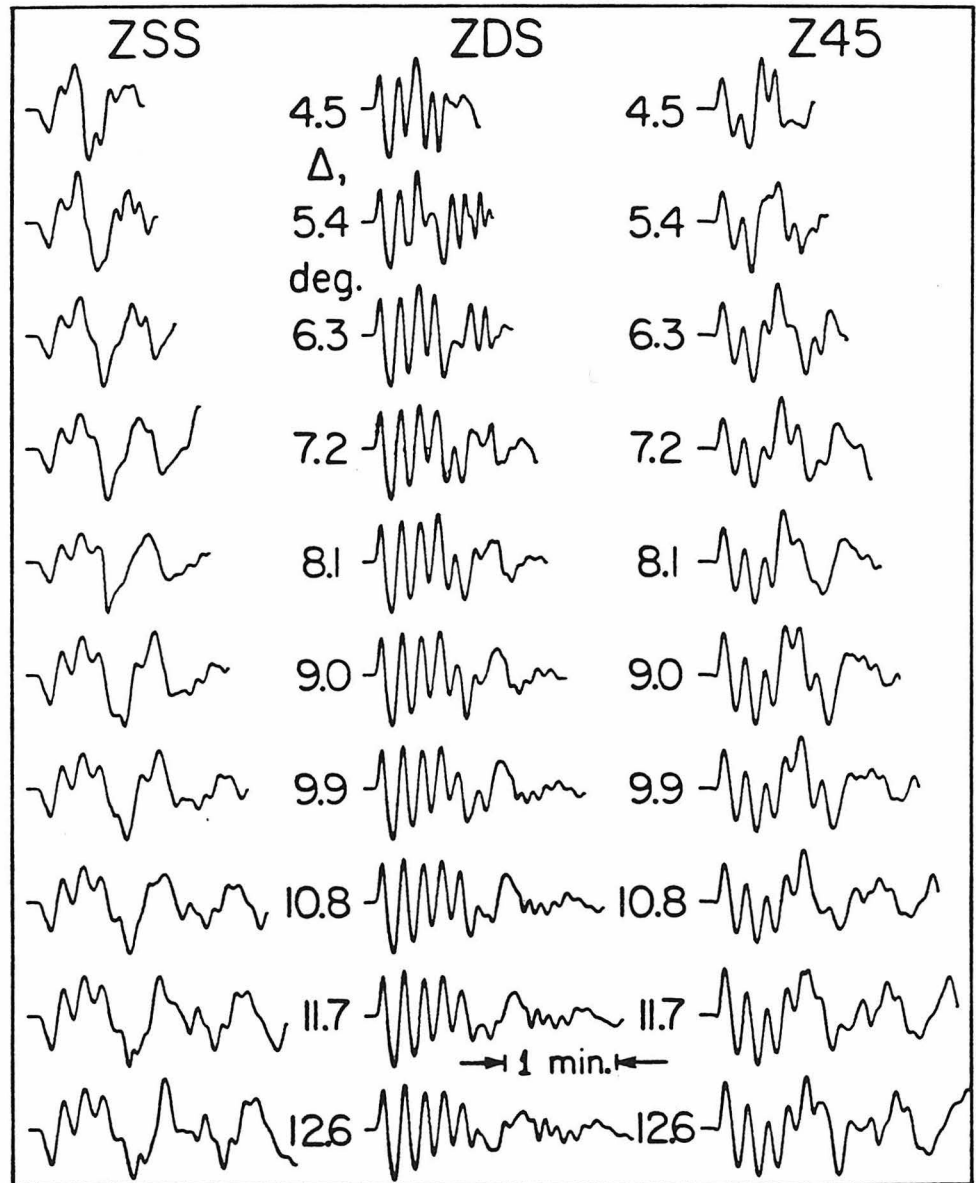


Figure 2-2: Theoretical displacement profiles for the vertical component. The Green's functions were computed from the model presented in Table 2-1 and have been convolved with a source time function represented by a trapezoid ($\delta t_1 = \delta t_2 = \delta t_3 = 1$ s), a triangular filter (2 s rise and fall), and the response function for a WWSSN long-period instrument.

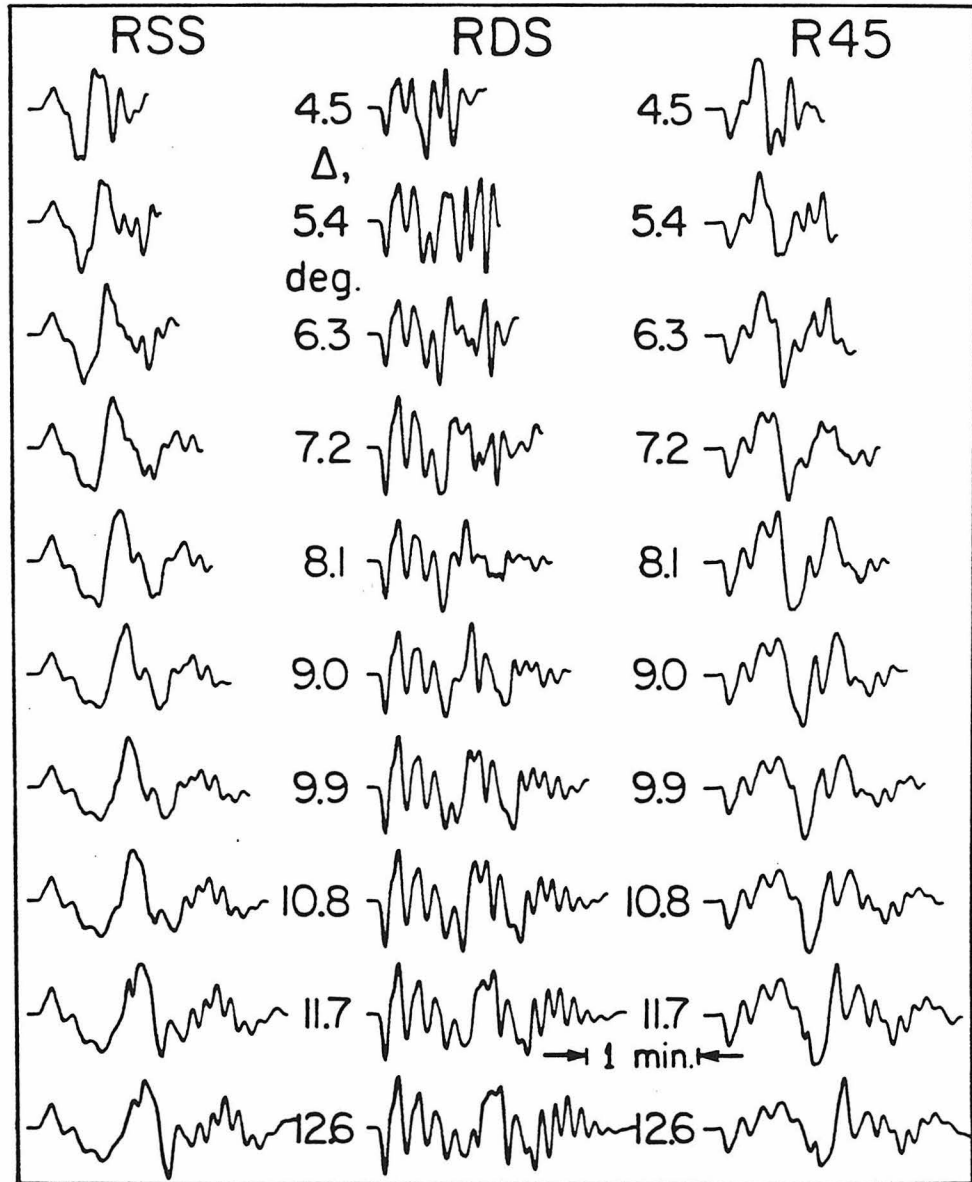


Figure 2-3: Theoretical displacement profiles for the radial component. The Green's functions are computed every 100 km. They have been convolved with the time function, instrument response and filter described in Figure 2-2.

fundamental faults is known, any seismogram can be constructed by a linear combination of them.

The displacements in Figures 2-2 and 2-3 were computed for a source depth of 8 km. Varying the source depth between 5 and 15 km has only a small effect on the waveform. This is easily understood by considering that to first order, a change in source depth affects only the travel time of the first segment of any ray. Figure 2-4 shows a comparison of the synthetic waveforms at 1000 km for these different source depths. After doubling the source depth (from 8 to 16 km), the essential character of the waveform is still preserved and the source information determined with Green's functions computed at an inappropriate depth is reliable. In contrast, a similar change in crustal thickness would affect the travel time of each leg of a given ray, hence significantly changing the waveform dispersion (see Figure 1-9). The insensitivity of the displacements to source depth allows the responses in Figures 2-2 and 2-3 to be used, at least in a qualitative fashion, to determine the source parameters of most crustal earthquakes.

The only other major question concerning the applicability of the displacements presented relates to the structure used in their calculation. The experience gained through inverting several events indicates that the simplistic model adopted is justified. The model in Table 2-1 is an average developed for the western United States, although it appears sufficient for most continental regions in the world. The waveform dispersion is dependent on crustal thickness and on the contrast between the upper mantle P velocity and mean crustal P velocity, so obviously for regions such as the Tibetan Plateau, the responses in Figures 2-2 and 2-3 would be inadequate. Also, as discussed in Chapter I, the use of the half space to approximate the upper mantle must cease to be valid at some point (when significant amounts of energy are

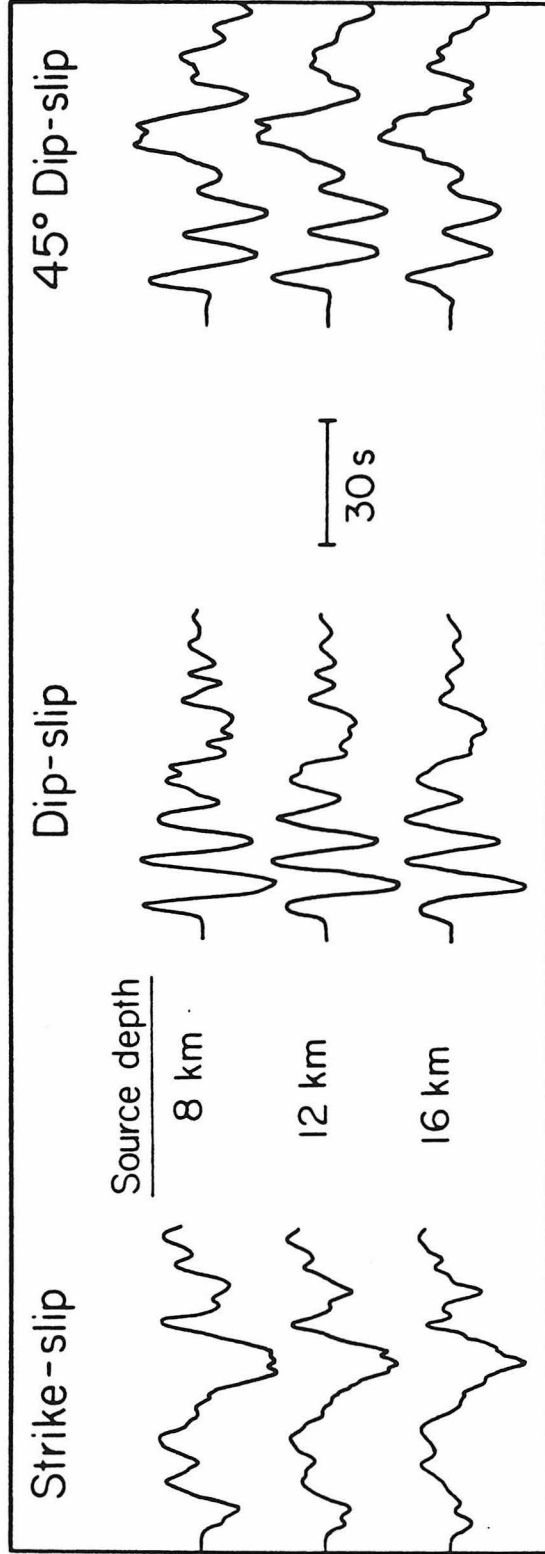


Figure 2-4: P_n waveforms at 1000 km for three different source depths.

present in the form of diving rays which have turned in the upper mantle). For this reason we rarely try to invert any data beyond 12°.

2.3 INVERSION TECHNIQUE

The comparison of an observation to a synthetic requires some assessment of the quality of the fit. The least-squares waveform inversion which we use makes use of an error function determined by the cross-correlation of a long-period seismogram and a synthetic waveform:

$$e = 1 - \frac{\int fg}{(\int f^2)^{1/2}(\int g^2)^{1/2}} \quad (2.3)$$

where f is the observed record, g is the synthetic waveform, and the integral is a zero lag cross-correlation. The limits of integration are the time length of the window in which the waveforms are correlated. The denominator serves to normalize both the data and the synthetics. This normalization makes the error function insensitive to the absolute amplitudes. To minimize the error, which corresponds to maximizing the correlation, f and g are allowed to optimally align themselves with regard to waveform; f and g are aligned a priori in time by matching first breaks and ignoring absolute travel time. Equation 2.3 can be rewritten considering that the synthetic seismogram is a construction of the three fundamental faults:

$$e = 1 - \frac{\sum_{i=1}^3 A_i \int u_{di} f}{\left[\sum_{i=1}^3 \sum_{k=1}^3 A_i A_k \int u_{di} u_{dk} \right]^{1/2}} \quad (2.4)$$

where f is now normalized. The u_{di} , where $d = w$ or q corresponding to the vertical

(W_i) or radial (Q_i), are the fundamental fault Green's functions convolved with the source time history, Instrument and any filters. The A_i are the coefficients in (2.2). For a given distance the cross-correlations are constant, and the errors are minimized by varying the A_i 's.

An objective function ε , which is the sum of the squares of the error functions, is minimized in terms of the three fault parameters. The problem can be stated formally by considering a starting model vector m^0 with an associated waveform error vector e^0 ; then we want to find a model change δm that minimizes the objective function:

$$\varepsilon^2 = \sum_{j=1}^N e_j^2 \quad (2.5)$$

where

$$\varepsilon_j^2(\delta m) = (e_j^0 + \delta e_j)(e_j^0 + \delta e_j)$$

Now consider δe_j ; from (2-4) we can write

$$\frac{\delta e_j}{\delta \Theta_k} \delta \Theta_k = \delta e_j \quad (2.6)$$

where Θ_k are the fault parameters strike, dip and rake. We can write the partial of the error function w.r.t. fault parameters as an $N \times 3$ matrix A , where N is the number of error functions, and we can write $\delta \Theta_k$ as a vector:

$$A \delta \Theta = A \Phi = \delta e \quad (2.7)$$

Rewriting (2-5):

$$\varepsilon^2 = (e + A \Phi)^T (e + A \Phi) \quad (2.8)$$

which can be expanded as:

$$\varepsilon^2(\delta m) = e^T e - e^T A \Phi - \Phi^T A^T e + \Phi^T A^T A \Phi \quad (2.9)$$

Now performing a first order perturbation in $\delta \Phi$ of (2.9) and setting to zero yields:

$$\Phi = (A^T A)^{-1} A^T e \quad (2.10)$$

This is the result that we require, which is the classical linear least squares solution (see *Wiggins*, 1972). This gives an inversion which is nonlinear, but a simple iterative technique is used to converge on the correct fault parameters. At each step the error functions and their partials must be recalculated, but the cross correlations only have to be calculated once. This makes recalculating the error function and partials trivial and therefore the procedure is efficient. In practice, we usually weight the data station by station and add some factor stabilizing the inverse; so we write (2.10) as

$$\Phi = (A^T W^2 A + \sigma I)^{-1} A^T W e \quad (2.11)$$

where W is the weighting matrix, whose diagonal terms are the weights assigned to each station. The weights range from 0.1 to 1.0, with the largest values assigned to the stations with the cleanest recordings. As with most geophysical inverse problems, some stabilizing factor must be added to the matrix to be inverted to insure proper convergence. If the damping factor σ is too small, the iterative process will take steps which are too large and may skip over the minima. If σ is too large, a prohibitively large number of iterations are required for convergence. For this particular problem, σ is adjusted during the inversion. At the start of the inversion, σ is set to some large value, usually 0.05, and then is adjusted to be proportional to the sum

of the trace of $A^T W^2 A$. The stability of the inversion depends on the quality and size of the data set. It is also possible to incorporate absolute amplitude information in the inversion, depending upon the circumstances. This is done by calculating a second error function for amplitude. For P_{nl} inversion, the amplitude partial is expensive and does not add much in the way of stability. Once the source orientation is fixed, the seismic moment of an earthquake can be determined by comparing the amplitudes of the synthetic waveform and the observations. Adopting the units of *Helmburger and Malone (1975)*, expressing the range in km, time in sec, density in $g\text{-cm}^{-3}$, velocity in km-s^{-1} , the moment in dyne-cm, and displacement in cm yields:

$$M_o = 4\pi\rho 10^{20} \left(\frac{\text{data amplitude}}{\text{synthetic amplitude}} \right) \quad (2.12)$$

A moment can be determined by comparing the maximum peak-to-peak amplitudes for any time window used for the correlation. It has been found that the moment should be determined for a few peaks at a given station. The ratio of the moment at each station to the mean is a measure of the amplitude stability. In general, the moments determined from P_{nl} are in very good agreement with those determined teleseismically, using the assumption of $t^* = 1$ s.

Figure 2-5 shows a test of the inversion procedure. The data were generated at various ranges and azimuths for a source with a strike of 10° , a rake of 80° , and a dip of 50° . Stations 1,4, and 5 are long-period WWSSN (15-100) records, while stations 2 and 3 are long-period LRSM records. Since the data were generated assuming a dip-slip orientation, the starting model was backed off to a strike-slip orientation. The cross-correlation coefficients between the data and the model are shown on the front of each trace. At the top of each column is the sum of error functions.

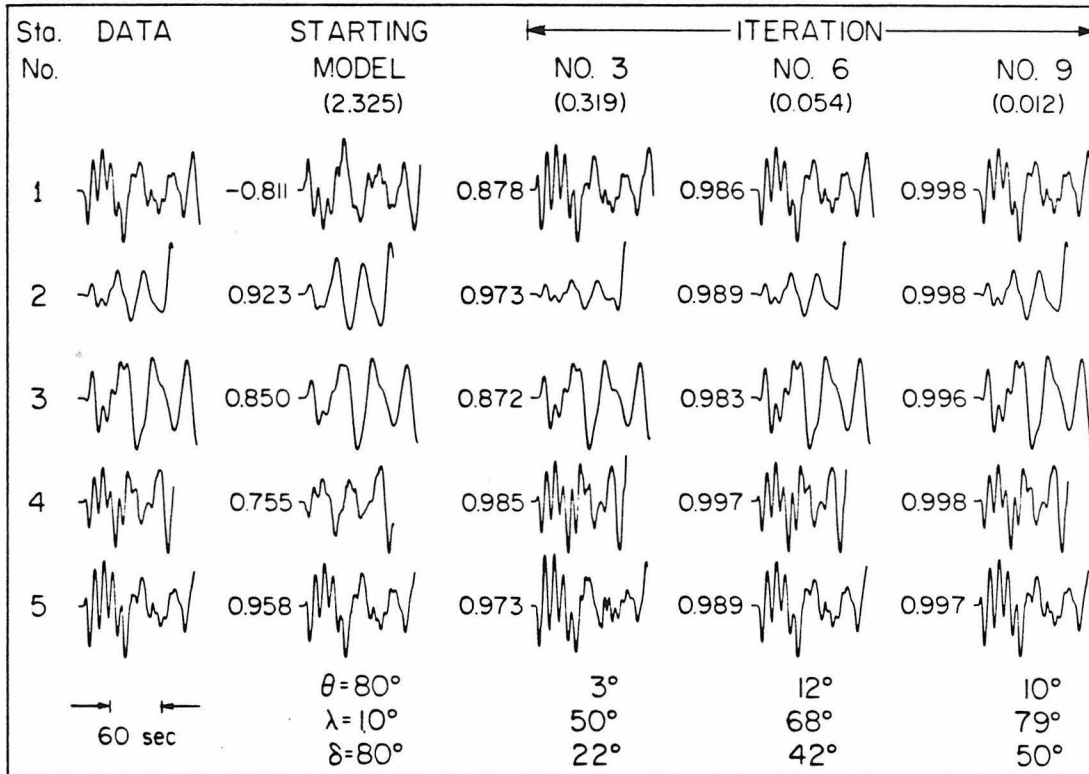


Figure 2-5: A test of the inversion program. The data was generated for a dip-slip earthquake and starting model has a strike-slip orientation. The cross-correlation coefficients between data and model are shown before each trace. At the top of each column is the sum of the error functions.

The rate at which the sum decreases is a measure of the rate of convergence. After three iterations the strike is essentially picked, and after six iterations the waveforms are in fair agreement. After nine iterations the starting model has been essentially reproduced.

When we invert real data the epicentral distances are rounded off to the nearest 100 km. This spacing in Green's function is usually adequate, since increasing the range mainly increases the separation between P_n and PL . Since both the data and synthetics are usually filtered (as in Figures 2-2 and 2-3) the time function, $f(t)$ does not greatly affect the shape of the synthetic (the trapezoid duration is shorter than the filter and contains more high frequencies), and it is assumed a priori. A mismatch between the first pulse width (P_n) in the data and the synthetics results when an inadequate time function is used; in this case the time function is altered until the mismatch disappears.

2.4 EXAMPLES

We show the results of the inversion of the P_{nl} waveforms from 7 earthquakes to demonstrate the utility of the technique. Five of the earthquakes occurred in the western United States. Two other earthquakes, one in Baffin Bay in the Arctic and the other in Turkey, have been included to demonstrate that the Green's functions are not unique to the Western U.S. Both dip-slip and strike-slip mechanisms are represented in the suite of examples.

Truckee, CA (9/12/66)

The Truckee earthquake was a strike-slip event at 10 km depth which produced excellent regional records but very few teleseismic body wave records, as is typical

of moderate-size strike-slip events. The Truckee earthquake ($m_b = 5.7$) has been studied by numerous authors (*Ryall et al.*, 1968; *Tsai and Aki*, 1970; *Burdick*, 1977), making it a good test case. *Tsai and Aki* (1970), from first motion studies and modeling of surface waves, determined this event to be pure strike-slip on a fault plane striking N44°E and dipping 80°SE. The surface wave moment was determined to be 0.83×10^{25} dyne-cm. Figure 2-1 shows the locations of the epicenter and the recording station. Figure 2-6 summarizes the analysis. Shown are the filtered data and corresponding synthetics, the correlation coefficient and moment determined from a given record. The stations at BOZ and TUC (LPZ) are nearly nodal, and it was judged that the waveform amplitudes were not sufficiently above the noise to be useful in the inversion procedure. The fact that those stations are nodal provides a valuable constraint on the mechanism, and any inversion solution must be consistent with this observation.

The inversion result for Truckee was very similar to the solution of *Tsai and Aki* (1970); a strike of N43°E, a dip of 76°SE, and a rake of -11°. The only significant difference is the slight dip-slip component, which is also acceptable on the basis of the first motion data. The moment determined from the inversion is 0.87×10^{25} dyne-cm, which is in excellent agreement with *Tsai and Aki's* (1970) moment. The moments determined at the different stations only show two anomalies; (1) a low amplitude at LON and (2) a large Pn to PL ratio at TUC. Both of these features occur for other events, suggesting anomalous structure.

El Golfo, Mexico (8/7/66)

The El Golfo earthquake ($m_b = 6.3$, $M_s = 6.3$) was a strike-slip event which occurred near the mouth of the Colorado River at the northern end of the Gulf of

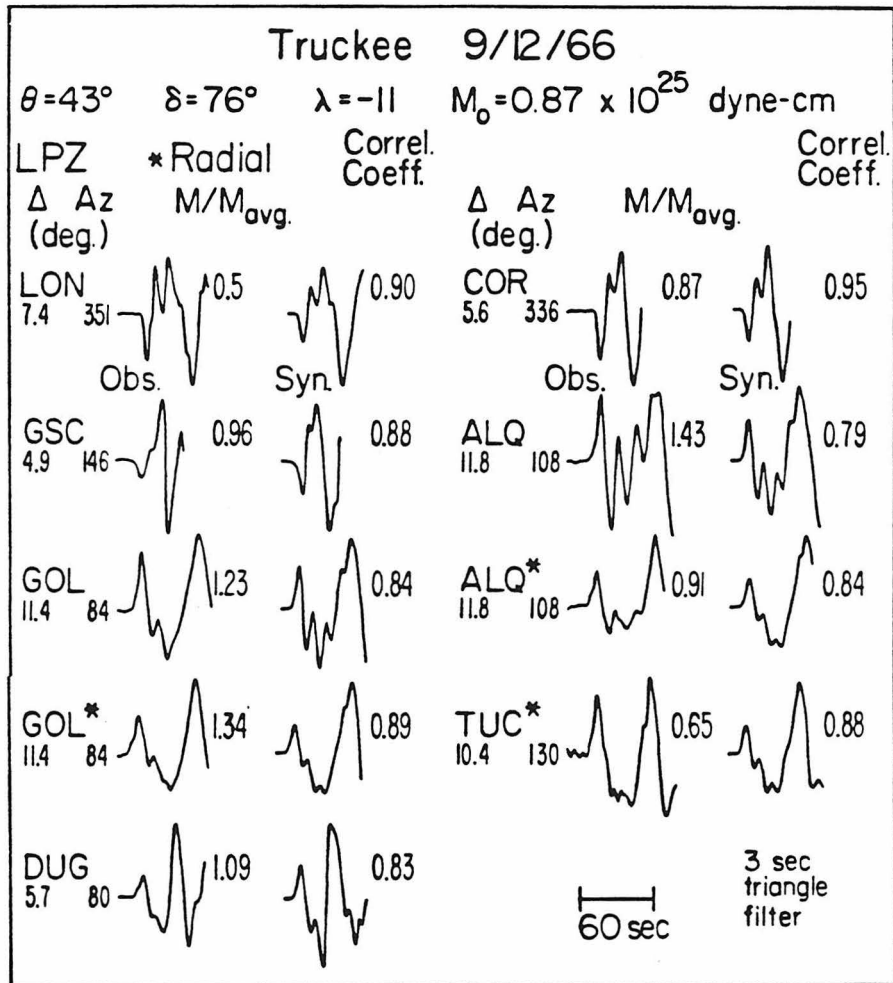


Figure 2-6: The filtered data and synthetics from the inversion solution for the Truckee earthquake. Along each trace the ratios of the station moment to the average moment is shown as a measure of amplitude stability. Also shown is the cross-correlation coefficient for the data and synthetic.

California. *Ebel et al.* (1978) determined the fault plane to be striking E140° S, dipping 85° to the southwest, and with a rake of 183°, and determined the depth of the event to be 10 km. Using teleseismic, long-period P waves, they determined a moment of 5×10^{25} dyne-cm.

El Golfo is about the maximum size event which can be used in the inversion technique. The P_{nl} records are barely on scale at the stations used. Figure 2-7 shows the location of the epicenter, the recording stations, and the waveforms. In this case, the time function is a triangle with a 2 second rise and fall; the impulse is a reflection of the event size. The long-period time function allows us to dispense with the use of a filter. In Figure 2-7, shown below the observed waveforms are the synthetic waveforms for the inversion solution; the strike is E137° S, a dip of 87°, and a rake of 175°. The inversion is in good agreement with results of *Ebel et al.* (1978). The moment determined from the P_{nl} waveforms is 4.6×10^{25} dyne-cm.

Pocatello, Idaho (3/28/75)

The Pocatello ($m_b = 6.7$) earthquake was a dip-slip event in eastern Idaho and, again, is well studied (*Bache et al.*, 1980; *Arabasaz et al.*, 1975). This earthquake occurred in a region which is frequented by moderate size events. *Bache et al.* (1980) determined the fault plane to be striking N45° E, to be dipping 39° to the west, and to have a rake of -53° (the fault plane is shown in Figure 2-8), and they determined a focal depth of 8.7 km. Using long-period teleseismic data only, they obtained a moment of 2.2×10^{25} dyne-cm, and with their preferred model using both short- and long-period data obtained a moment of 1.5×10^{25} dyne-cm. *Williams* (1979) obtained a moment of 1.2×10^{25} dyne-cm from surface waves.

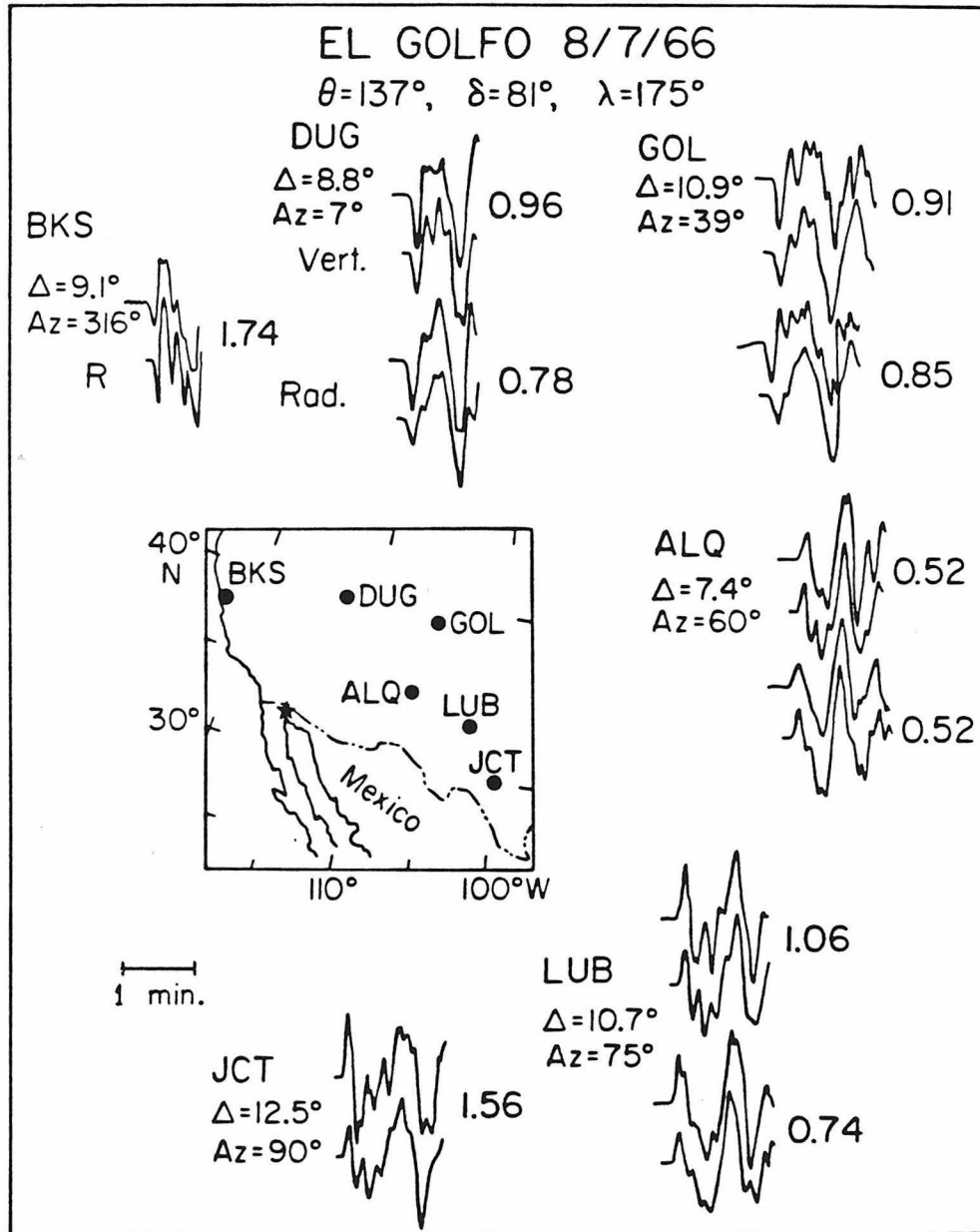


Figure 2-7: Data and synthetic waveforms for the El Golfo earthquake. The map gives the location of the event (star) and the recording stations. Along each trace is the ratio of the station moment to the average moment.

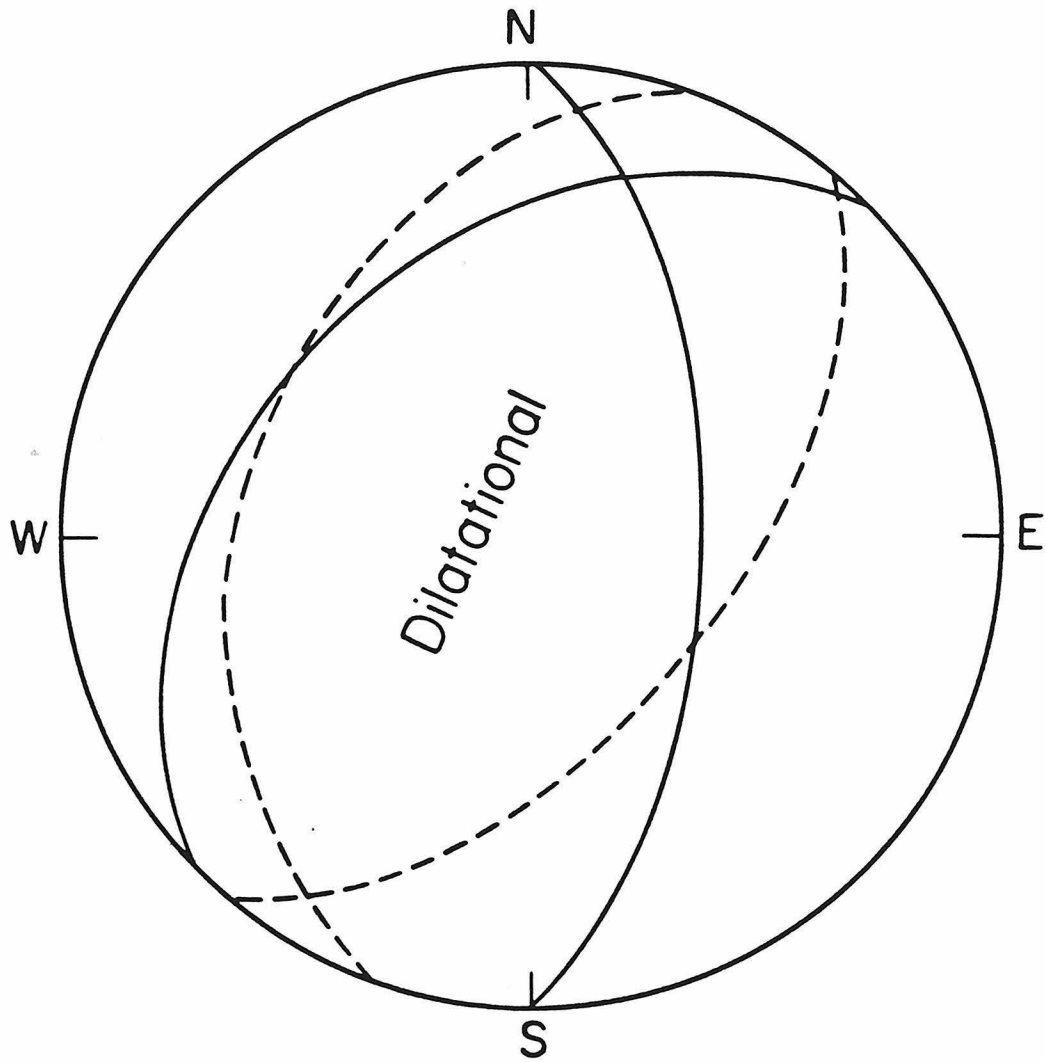


Figure 2-8: Fault plane solutions of the Pocatello earthquake. The solid line gives the *Bache et al.* (1980) solution, while the dashed lines give our solution.

The inversion solution for the Pocatello event appears superficially different from that of *Bache et al.* (1980), but Figure 2-8 shows both their fault plane solutions and ours; in fact, the solutions are similar. We found a strike of N20°E, a dip of 38° to the west, and a rake of -110°. The inversion solution is fairly consistent with the local first motion data. The moment determined from the regional data is 1.6×10^{25} dyne-cm, which is in good agreement with the various authors' determinations. Figure 2-9 shows the data and the synthetics. Figure 2-10 shows why the *Bache et al.* (1980) solution was altered in the inversion. Although most stations were fit well by either model, PAS and TUC were fit poorly by the *Bache et al.* (1980) solution as compared to the solution found with the P_{nl} data.

Cache Valley, Utah (8/30/62)

The Cache Valley earthquake occurred during the time of the most dense deployment of the LRSM network. The magnitude was 5.7, and a fault plane solution has been determined by *Smith and Sbar* (1974). The earthquake epicenter is within 60 km of the Pocatello epicenter so we would expect the regional stress patterns to be similar. The location of the event, recording stations, and seismograms are shown in Figure 2-11. Although the depth of the earthquake is not precisely known, it is assumed that it is shallow from the similarity of the waveforms to those of the Pocatello earthquake. The inversion yields a solution with a fault plane striking N33°E, dipping 34° to the east and having a rake of -64°, which is similar to *Smith and Sbar's* (1974) solution, although it violates a few more of the local first motions. The moment determination is 0.71×10^{25} dyne-cm. Figure 2-12 shows the filtered data and synthetics, with the ratio of the moments.

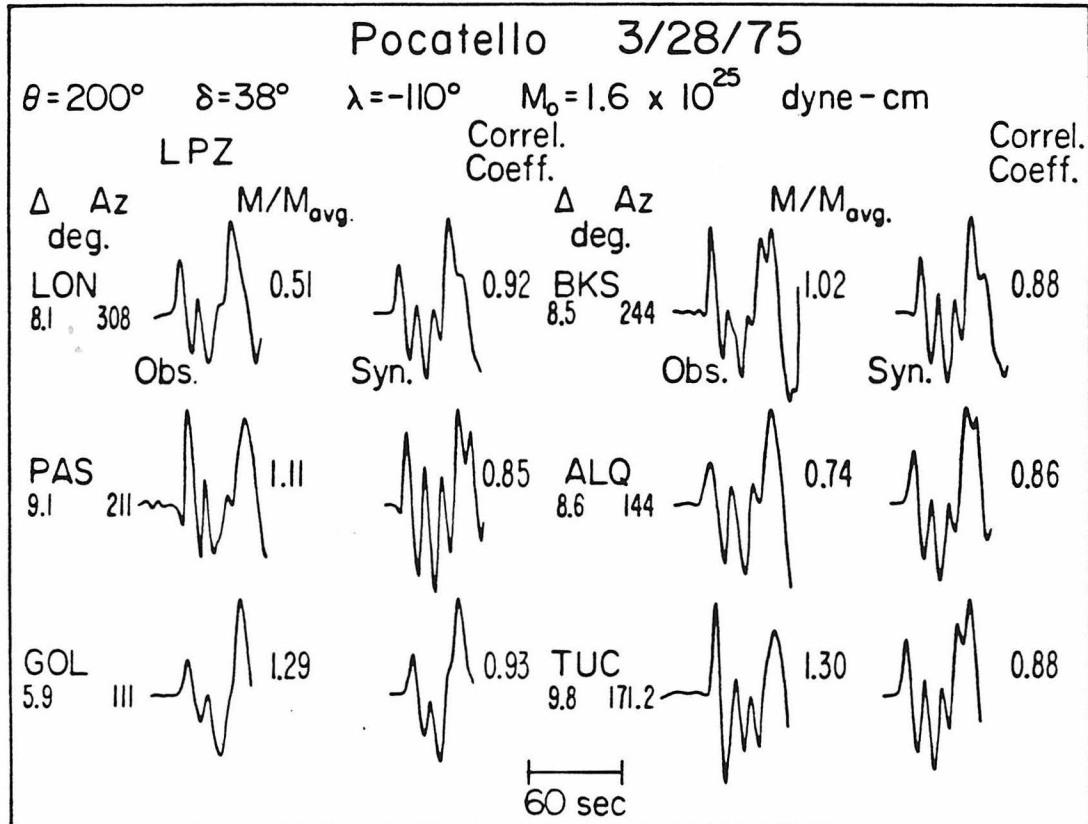


Figure 2-9: The filtered data and synthetics from the Pocatello earthquake. The data and synthetics are filtered with a 3 second triangle. Along each trace is the ratio of the station and average moment as well as the cross-correlation coefficient.

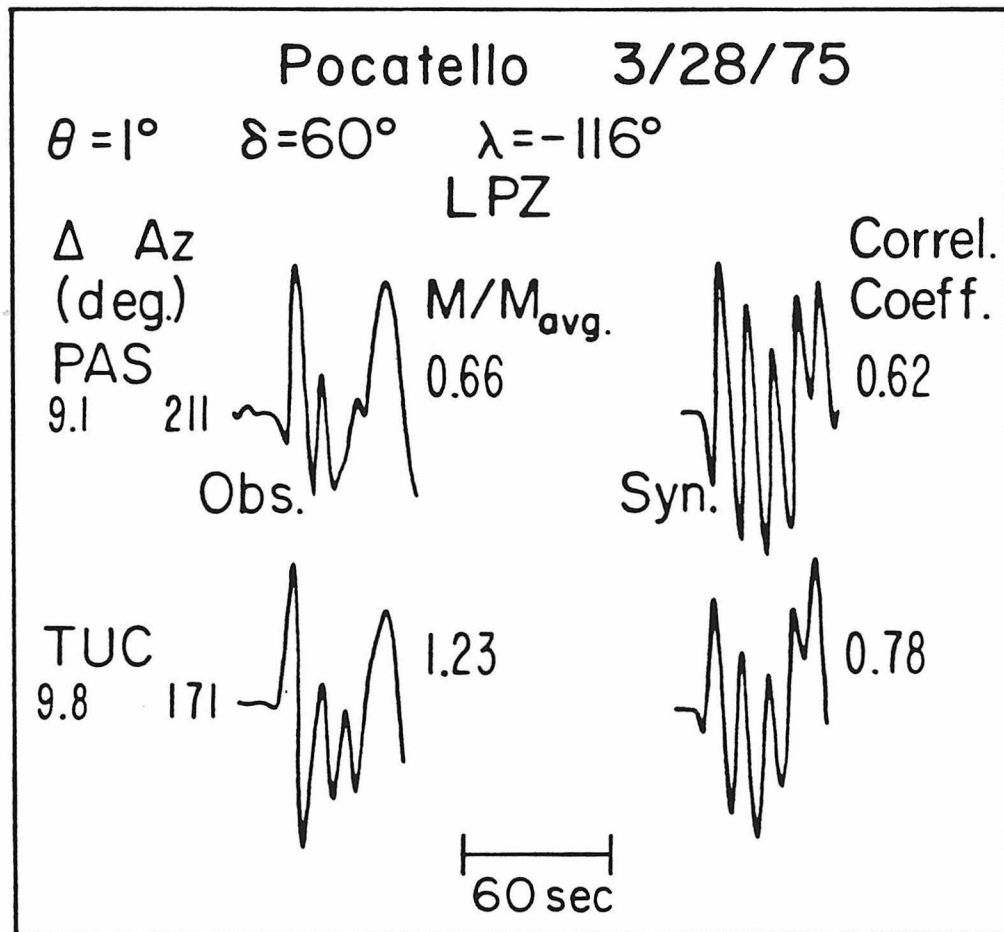


Figure 2-10: The filtered data and synthetics using the *Bache et al.* fault plane solution. Note the first motion is incorrect at TUC and the relative amplitudes at PAS are bad.

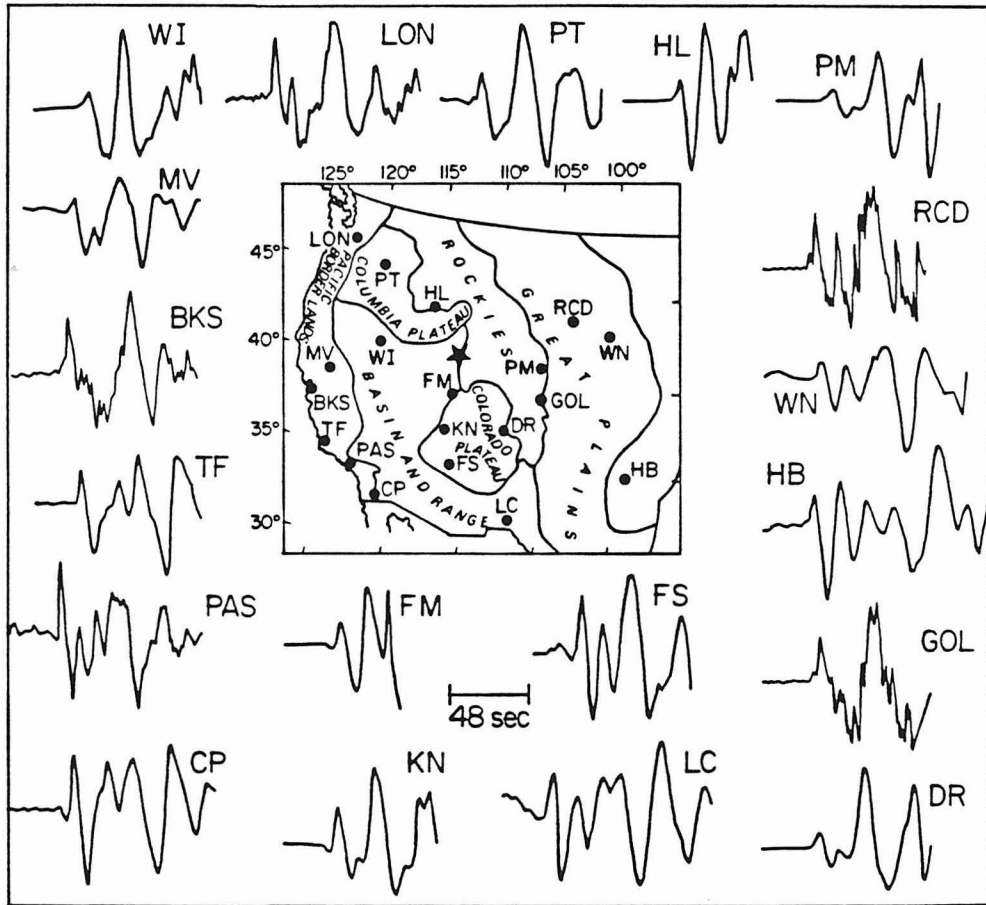


Figure 2-11: Location of the Cache Valley event and the stations recording it. The stations with two letter abbreviations are long-period LRSM instruments, and the others are WWSSN instruments. All records shown are vertical components.

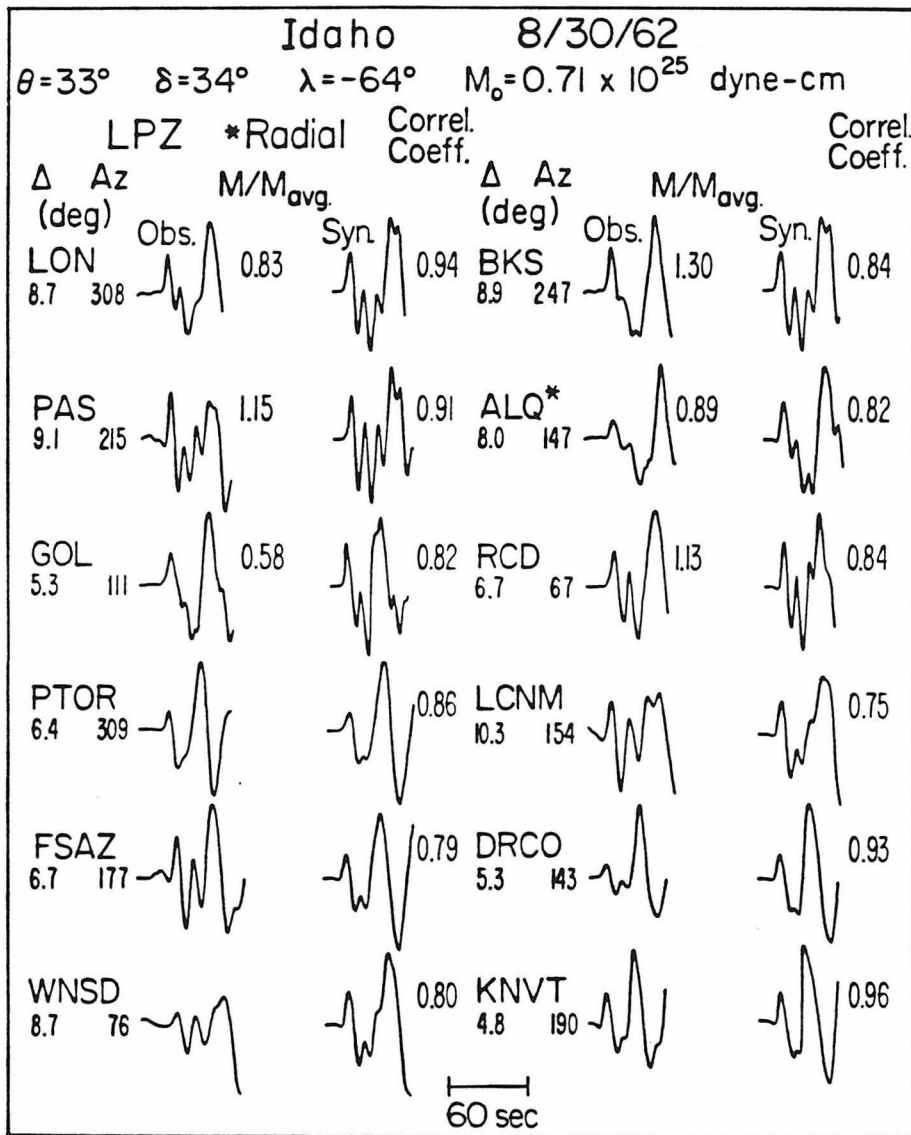


Figure 2-12: The filtered data and synthetics for the 1962 Cache Valley earthquake. The moment was determined from the WWSSN stations, and the moment ratios are shown for these stations. The cross-correlation coefficients are shown.

Oroville, California (1/8/75)

The Oroville earthquake ($M_s = 5.6$) was a normal faulting event and is interesting because the surface wave (*Hart et al.*, 1977) and the body wave (*Langston and Butler*, 1976) analysis yield substantially different moments. *Langston and Butler* (1976) determined the strike to be 180° , with a dip of 65° , and a rake of -70° . Their moment determination is 5.7×10^{24} dyne-cm. *Hart et al.* (1977) suggested that the surface waves are consistent with the body wave mechanism but that the moment is larger by a factor of 3 (1.9×10^{25} dyne-cm). Figure 2-13 shows the location of the event, of the stations used in the inversion analysis, and the filtered data and synthetic waveforms. The inversion solution has shifted the mechanism to a strike of 204° , dipping 66° with a rake of -85° . This new solution violates only a few first motions, but the aftershock trend tends to support the 180° strike (*C. Langston*, personal communication, 1981). The moment determined from the P_{nd} data is 6.9×10^{24} dyne-cm.

Baffin Bay, Canada (9/4/63)

The Baffin Bay earthquake ($M = 5.9$) was a normal event associated with the Canadian continental margin. The travel path to each of the stations used in the inversion includes portions of continental and oceanic regions, which makes it an ideal event to test the applicability of the Green's functions. *Liu and Kanamori* (1980) modeled the body waves and determined a fault-plane solution with a strike of 98° , a dip of $66^\circ N$, and a rake of -103° . The location of the event, and the filtered data and synthetic waveforms are shown in Figure 2-14. The inversion solution has a mechanism striking 74° , dipping 66° , and a rake of -100° . The only appreciable

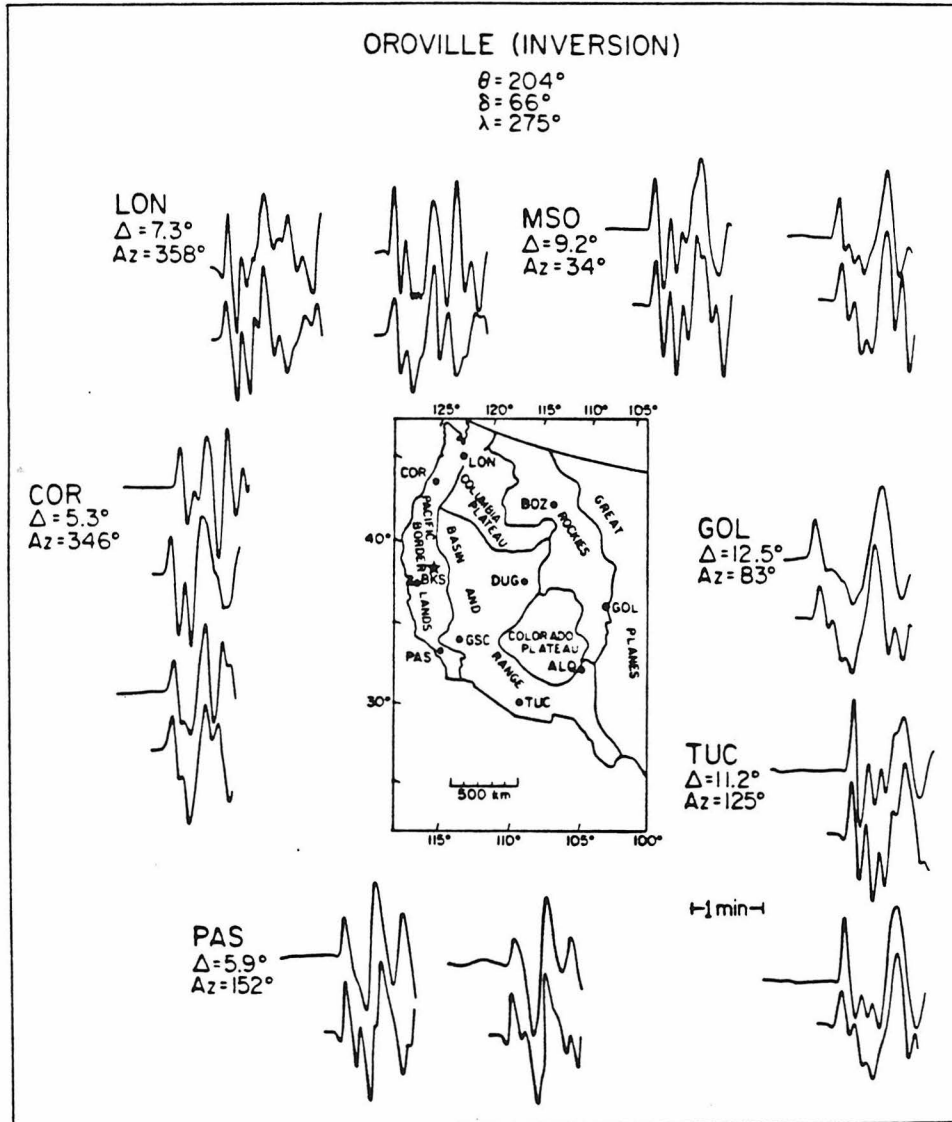


Figure 2-13: Filtered data and synthetic waveforms for the Oroville earthquake. At all the stations except GOL both the vertical (the first trace pair) and radial components are shown.

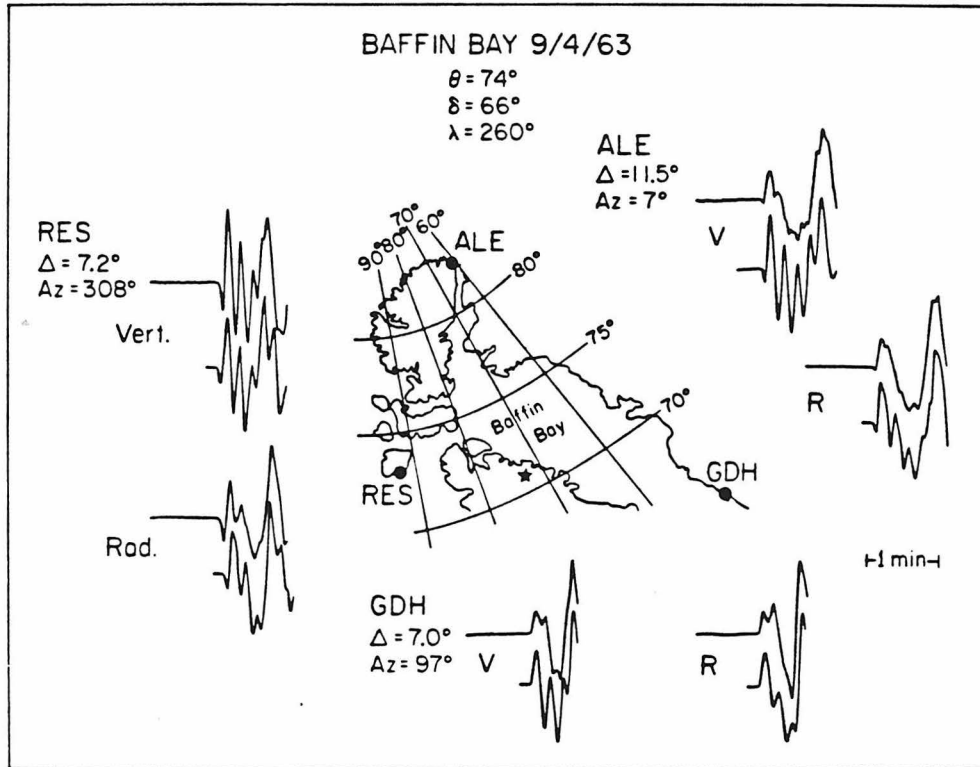


Figure 2-14: Location of the Baffin Bay earthquake (star) and the recording stations. Filtered data and synthetic waveforms for both the vertical and radial components are shown.

difference between the regional and teleseismic analysis is the difference of 20° in strike which can be considered as the resolution for dip-slip events.

Southwest Turkey (6/13/65)

The Turkish event ($M = 5.7$) was a shallow, normal event which occurred in southwest Turkey in a region of north-south extension. *McKenzie* (1972) used first-motion data to determine a pure normal mechanism with a strike of 101° and dipping 70° to the south, although it is not well constrained. There were three WWSSN stations at regional distances which could be used in the inversion process. Figure 2-15 shows the locations of the event and the recording stations. The filtered data and the fit of the synthetic waveforms are also shown. The inversion solution (strike 131° , dip 68° , rake -88°) is consistent with the first motion data, although it differs in strike from *McKenzie*'s solution. Again the three-station solution is quite acceptable, considering the quality of the first-motion data.

2.5 DISCUSSION

Determining the fault plane orientation of moderate size earthquakes is often a frustrating experience, owing to the paucity of high quality data. Earthquakes in the magnitude range 5-6 are quite important and are often the only "measurable" expression of the present tectonic environment. All of the available data must be used to extract the source parameters of these moderate size events, and the modeling of P_{ni} waveforms can provide a valuable constraint in the process. Every situation will probably be unique and it is difficult to predict which data set will be the most definitive. Nevertheless, it appears worthwhile to consider the P_{ni} inversion separately and its resolvability dependence on source orientation.

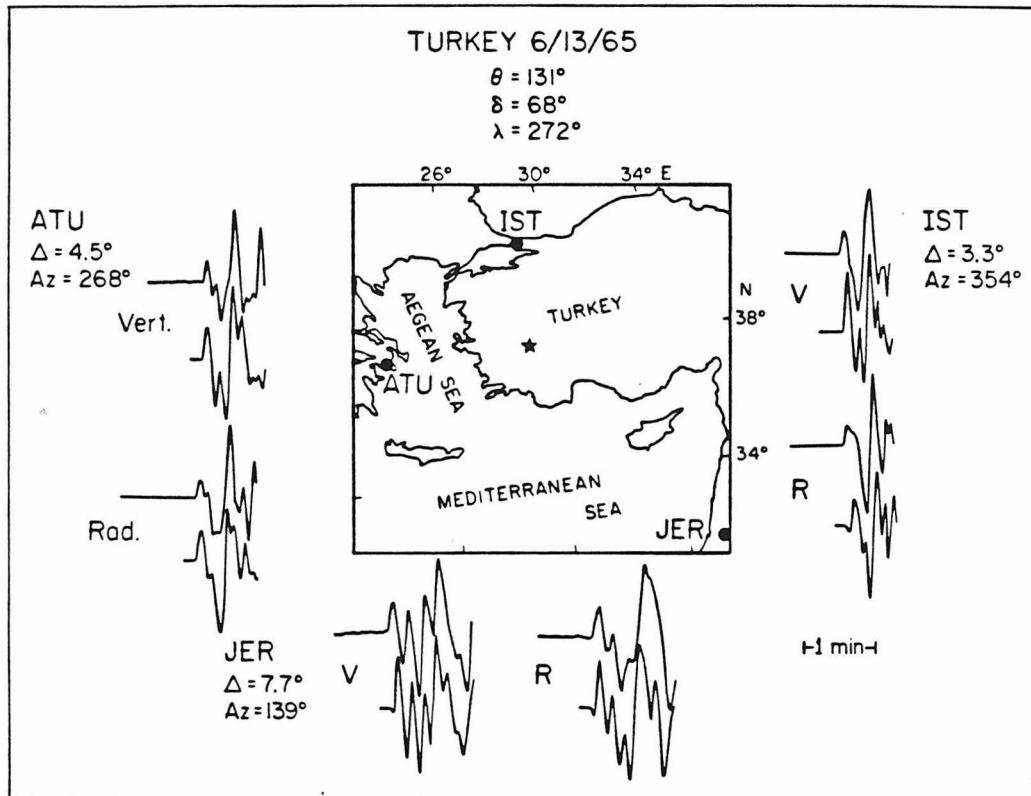


Figure 2-15: Location of the Turkey earthquake (star) and recording stations. Filtered data and synthetic waveforms for both the vertical and radial components are shown.

The inversion process discussed requires only a small data set. With ideal azimuthal separation, a data set comprising just three stations (vertical and radial components) can yield good solutions (it is possible to construct a case where the inversion is unstable, but in practice this has never happened). In almost all cases four recording stations are sufficient. P_{ni} should be polarized in the vertical and radial planes. Rotation of the horizontal components for a number of events indicates that there is very little energy on the tangential component, implying little contamination from such effects as multipathing. Therefore, it is usually sufficient to take the largest of the horizontal components to be the radial waveform in the inversion. The resolving ability of the inversion (or conversely, the error) depends on the type of earthquake. The experience gained by considering the examples presented in the last Section indicates that the mechanisms of strike-slip earthquakes can be determined quite well using data from relatively few stations. The strike is usually determined to within 5° of that determined by other methods. The rake is the least resolvable parameter for strike-slip events and can vary by up to 15° from that determined by first-motion studies. The mechanisms of dip-slip earthquakes are more difficult to determine. Although the dip and rake are usually determined in good agreement with other studies, the strike may vary by up to 20° . This feature is illustrated by considering a 45° dipping normal fault. In this case, most regional stations lie within the compressional region of the focal sphere and any given azimuth will produce remarkably similar waveforms. Fortunately, dip-slip events have rather strong teleseismic P waves, but again the waveforms are all the same, with little dependence on azimuth. In this case the stations lie in the center of the focal sphere and are all dilatational. As an example consider Figure 2-16, which displays the focal sphere and the teleseismic waveforms for the Oroville earthquake. Note that the P waveforms are all

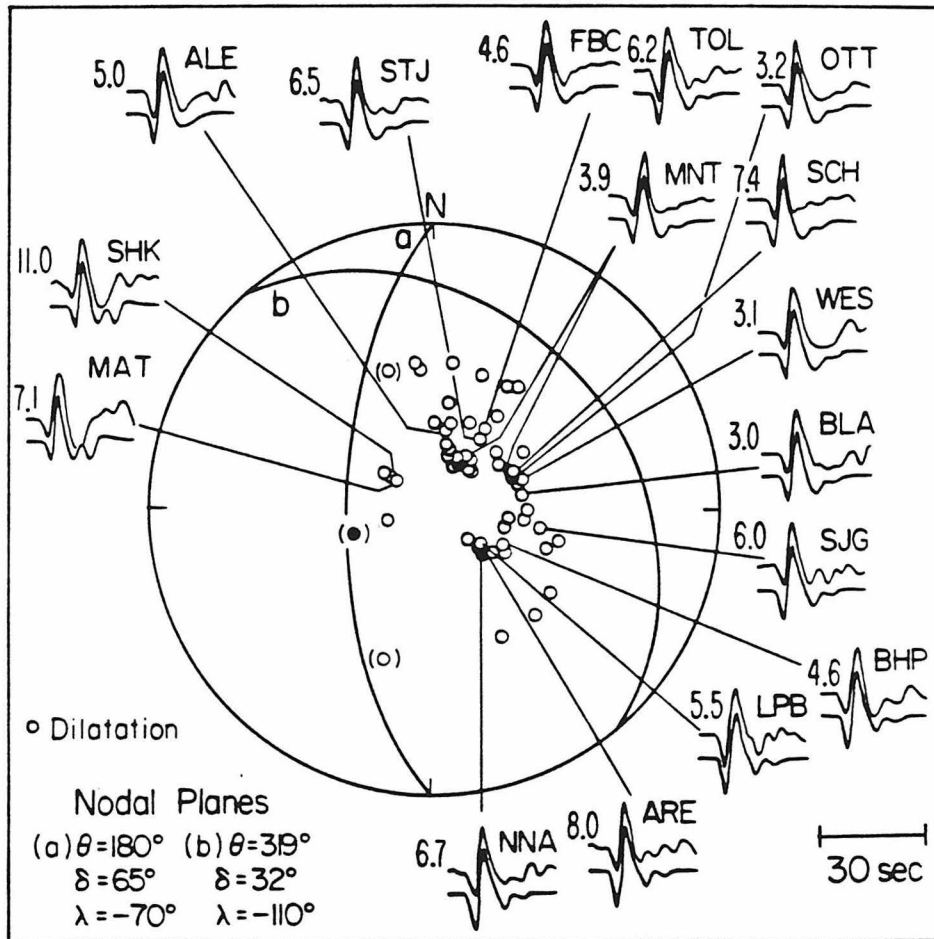


Figure 2-16: Teleseismic first motions from the Oroville earthquake. Note the similarity of waveforms for all azimuths. Shown on each trace is the moment ($\times 10^{25}$ dyne-cm) determined at that station. Note the scatter over a factor of 3 (Figure from *Langston and Butler, 1976*).

similar, and the synthetic waveforms (*Langson and Butler, 1976*) do not add much insight into determining the strike of the fault. Figure 2-17 shows the filtered regional data and the synthetic waveforms computed from the teleseismic fault-parameter determinations. A comparison of Figures 2-17 and 2-13 shows that the regional data-inversion solution improves the fit of the synthetic waveforms, in particular PAS. This suggests that a logical approach would be to invert some teleseismic data and the regional data simultaneously. Since the inversion technique relies on the cross-correlation of data and a synthetic waveform, the joint inversion is quite tractable.

The higher resolution of the strike-slip events is actually fortuitous. Moderate-size strike-slip earthquakes rarely produce usable teleseismic P waves, owing to their inefficiency in radiating energy straight down. On the other hand, strike-slip events produce very good regional waveforms. This allows the inclusion of a larger data set in the inversion, and hence the resolution problem is at least partly resolved.

It is reasonable to consider what effect the structural model has on the inversion results. As a test of the insensitivity of the fault orientation to small changes in crustal parameters the El Golfo earthquake was reinverted with a different structure. The crustal thickness was reduced to 24 km, the source depth was moved 12 km, and the Pn velocity reduced to 7.8 km-sec^{-1} . Although the quality of the fit decreases significantly the mechanism returned by the inversion is similar; strike 138° , dip 82° , and rake 181° . The moment increases to 6.9×10^{25} dyne-cm.

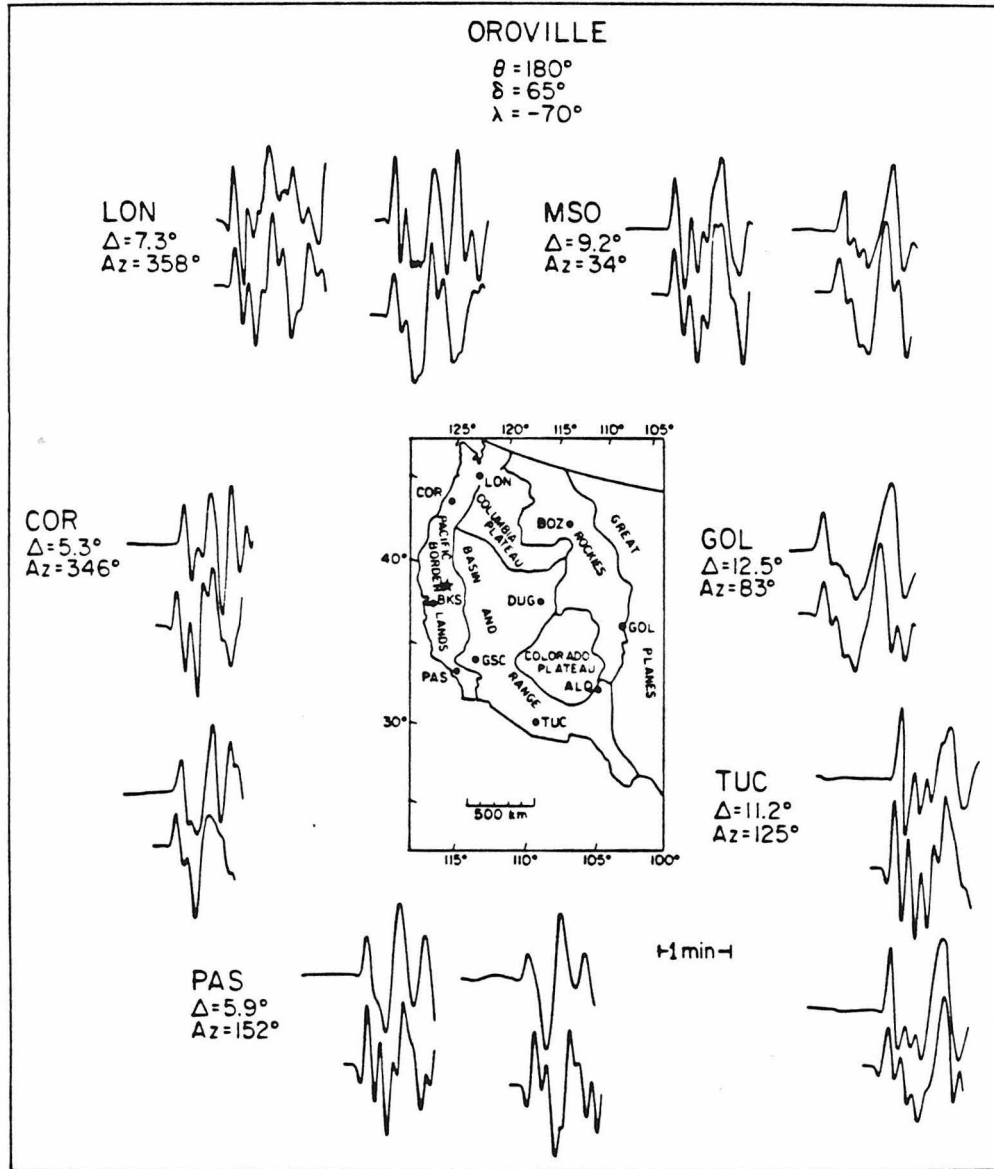


Figure 2-17: Filtered P_{nl} waveforms from the Oroville earthquake. The synthetic waveforms were computed with the telesismic fault-plane solution.

2.6 CONCLUSIONS

It is possible to extract the source parameters of moderate-size earthquakes for the long-period regional body waves. The procedure requires the comparison of the observed with a synthetic waveform; the synthetic waveforms can be generated by a linear combination of the waveforms of the three fundamental faults, shown in Figures 2-2 and 2-3. Although these synthetic waveforms are for a simple model, the inversion parameters (fault strike, dip and rake) are fairly insensitive to small changes in crustal thickness, Pn velocity and mean crustal velocity. This allows this single set of Green's functions to be used for most continental earthquakes. The inversion procedure requires only a small data set, and is particularly ideal for strike-slip earthquakes.

REFERENCES

- Arabasz, W.J., W.D. Richins C.J. Langer (1975). Detailed characteristics of the March 1975, Idaho-Utah border earthquake sequence (abstract), *EOS* 56, 1022.
- Bache, T.C., D.G. Lambert and T.G. Barker (1980). A source model for the March 28, 1975 Pocatello Valley earthquake for time domain modeling of teleseismic P waves, *Bull. seismo. Soc. Am.*, 70, 405-418.
- Burdick, L.J. (1977). Broad-band seismic studies of body waves, Ph.D. thesis, Calif. Inst. of Technol., Pasadena.
- Ebel, J.E., L.J. Burdick and G.S. Stewart (1978). The source mechanism of the August 7, 1966 El Golfo earthquake, *Bull. seismo. Soc. Am.*, 68, 1281-1297.
- Hart, R.S., R. Butler and H. Kanamori (1977). Surface-wave constraints on the August 1, 1975 Oroville earthquake, *Bull. seismo. Soc. Am.*, 68, 301-316.
- Helmberger, D.V. (1974). Generalized ray theory for shear dislocations, *Bull. seismo. Soc. Am.*, 64, 45-64.
- Helmberger, D.V. and S.D. Malone (1975). Modeling local earthquakes as dislocations in a layered half space, *J. Geophys. Res.*, 80, 4881-4888.
- Helmberger, D.V. and G.R. Engen (1980). Modeling the long-period body waves from shallow earthquakes at regional distances, *Bull. seismo. Soc. Am.*, 70, 1699-1714.
- Langston, C.A. and D.V. Helmberger (1975). A procedure for modeling shallow dislocations, *Geophys. J.* 42, 117-130.
- Langston, C.A. and R. Butler (1976). Focal mechanism of the August 1, 1975 Oroville

- earthquake, *Bull. seismo. Soc. Am.*, 66, 1111-1120.
- Liu, H.L. and H. Kanamori (1980). Determination of source parameters of mid-plate earthquakes from waveforms of body waves, *Bull. seismo. Soc. Am.*, 70, 1989-2004.
- McKenzie, D. (1972). Active tectonics of the Mediterranean region, *Geophys. J.*, 30, 109-185.
- Ryall, A. J.D. Van Wormer and A.J. Jones (1968). Triggering of microearthquakes by eartides and other features of the Truckee, California earthquake sequence of September, 1966, *Bull. seismo. Soc. Am.*, 66, 215-248.
- Smith, R.B. and M.L. Sbar (1974). Contemporary tectonics and seismicity of the western United States with emphasis on the Intermountain Seismic Belt, *Geol. Soc. Am. Bull.*, 85, 1205-1218.
- Tsai, Y.B. and K. Aki (1970). Source mechanism of the Truckee, California earthquake of September 12, 1966, *Bull. seismo. Soc. Am.*, 60, 1199-1208.
- Wiggins, R. (1972). The general linear inverse problem: Implications of surface waves and free oscillations for earth structure, *Rev. Geophys. Space Phys.*, 10, 251-285.
- Williams, B.R. (1979). M_0 calculations from a generalized AR parameter method for WWSSN instruments, *Bull. seismo. Soc. Am.*, 69, 329-351.

Chapter III: The Inversion of Long-Period Regional Body Waves for Crustal Structure

3.1 INTRODUCTION

Determining the structure of the crust has long been an important objective in the science of geophysics. Certainly more money has been spent on this problem than any other in seismology with the possible exception of discrimination. The reasons for this are many-fold. First, the Moho is a major discontinuity which is relatively accessible; the data which is required can be as simple as Pn travel times. Secondly, crustal structure is a valuable tool in resource geology. And finally, crustal thickness and Pn velocity are often a reflection of the regional tectonics. *Pakiser* (1963) first noted that Pn velocities and crustal thickness are related. *Black* and *Braille* (1982) demonstrated that in the western U.S. there is a statistically significant relationship between the Pn velocity and heat flow. Heat flow has also been related to crustal age (*Polyak* and *Smirnov*, 1968) and to the thickness of the lithosphere (*Pollack* and *Chapman*, 1977). These results taken together suggest the thickening of the lithosphere and the increase in upper mantle Pn velocity are related processes caused by the cooling of the continental lithosphere with time after a thermo-tectonic event (*Black* and *Braille*, 1982). Therefore, variations in Pn velocity and crustal thickness can be used as a measure of the regional differences in temperature at the Moho discontinuity.

The standard procedures for determining the crustal structure include seismic refraction, time-term analysis of earthquake travel times, dispersion of surface waves, and most recently, seismic reflection (COCORP). In seismic refraction work the short-period arrival times (see *Prodehl*, 1970 for example) along a profile of recording stations are used to construct a travel time curve. More recently, (see *Braille et al.*, 1982 for example) the short-period seismograms have been modeled with the reflectivity technique. Seismic refraction studies require clearly defining the arrivals, and therefore, it is best when the station density is high. Earthquake travel-times can also be used (for example, see *Hearn*, 1983), but again to apply the time-term method high station density is required. In any case, the crustal structure models which are derived from refraction surveys are detailed, but to develop a map of crustal thickness or Pn velocity over a large area is very expensive in terms of time and effort. On the other hand, surface wave dispersion studies (see *Langston and Helmberger*, 1974; *Poupinet*, 1972 for examples) are quite useful in determining the regional crustal structure. Unfortunately, the resolution is usually poor.

In this chapter we present a technique for the inversion of long-period regional body waves for crustal structure. If the seismic source is known, then the differences between the observed P_{nl} and synthetic can be parameterized in terms of structure along the travel path. Figure 3-1 shows the P_{nl} waveforms for several strike-slip earthquakes in the western U.S. The travel path lengths for all these events are approximately the same, yet there is a difference in the timing (or dispersion) of the arrivals. These differences can be attributed to lateral variations in such parameters as crustal thickness and Pn velocity. We can take advantage of the fact that a single Green's function computed for an average model can be "stretched" or

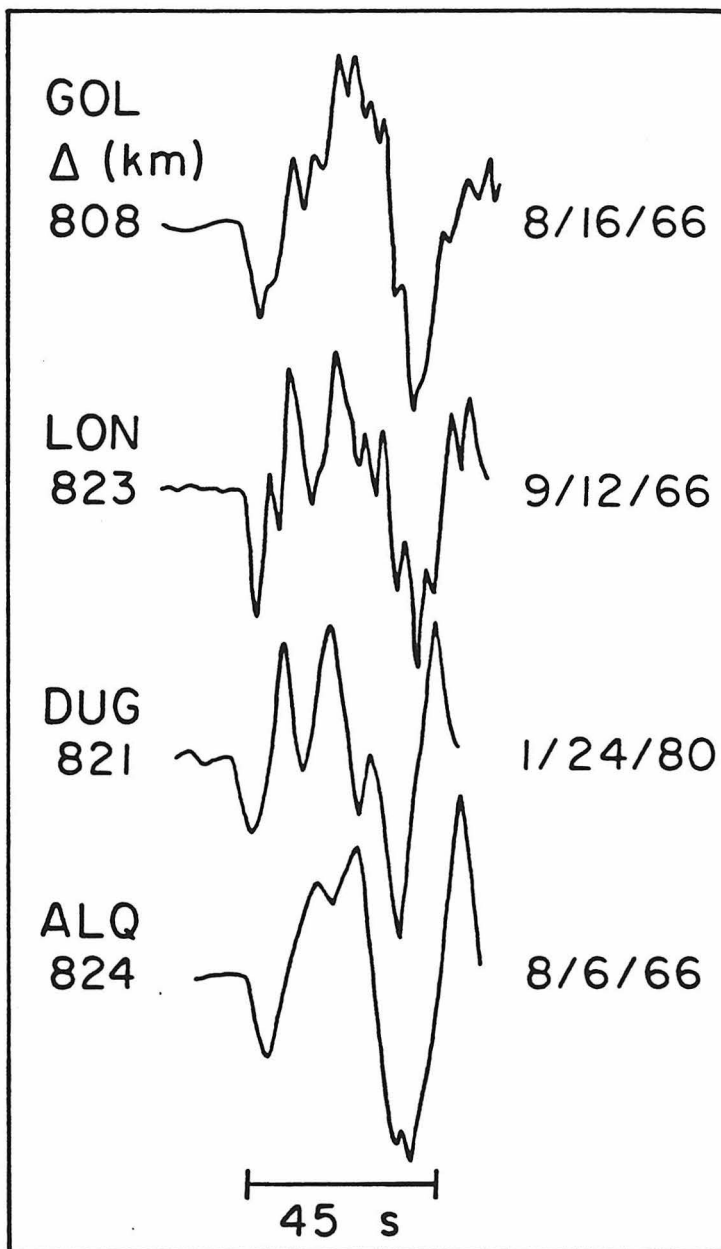


Figure 3-1: The *PnL* waveforms from four western U.S. strike-slip earthquakes. All the events have approximately the same travel path length. Note the differences in the separation between Pn and PL.

"squeezed" to simulate a range of structures. Therefore, the synthetic can be adjusted until the fit to the observation is maximized. Since the Green's functions are not recomputed the procedure is economical. The technique is ideal for an area such as the western U.S. since there is an abundance of sources and long-period recording stations.

3.2 INVERSION PROCEDURE

We use a least squares waveform inversion which is based on the same error function that was described in chapter II. Namely, the cross-correlation of a long-period seismogram (f) and a synthetic (g):

$$e = 1 - \frac{\int fg}{(\int f^2)^{1/2} (\int g^2)^{1/2}} \quad (3.1)$$

g is the synthetic, which is a function of n structural parameters:

$$g = F(x_1, x_2, \dots, x_n) \quad (3.2)$$

The limits of integration are time length of the window in which the waveforms are correlated. The autocorrelations in the denominator normalize the numerator, and therefore the error function is insensitive to absolute amplitudes. f and g are aligned a priori in time by matching first breaks; the absolute travel time is used to determine the starting model's Pn velocity. The error in (3.1) is minimized in terms of structural parameters in (3.2). This is done with numerical derivatives of e with respect to (x_1, x_2, \dots, x_n) :

$$\frac{\partial e}{\partial x_i} = \frac{(e(x_i + \Delta x_i) - e(x_i))}{\Delta x_i} \quad (3.3)$$

The numerical partial derivative is easily computed since the P_{ni} waveform of the starting model can be "stretched" or "squeezed" to simulate the P_{ni} waveform of the Δx_i structure. The inversion is an iterative process. We have a starting model \hat{m}^0 and an associated error e . A change in the the starting model, $\delta\hat{m}$, is determined such that the error is decreased. $\hat{m}^0 + \delta\hat{m}$ now becomes the starting model and the process is repeated.

In theory, any number of structural parameters could be used in the inversion. Of course, since only one seismogram is fit at a time, it is an underdetermined problem, and the question of non-uniqueness arises. There are two physical quantities which can be measured; (1) the absolute travel time, and (2) the waveform shape. In chapter I the dependence of the P_{ni} waveform shape on crustal thickness, Pn velocity, crustal P velocity and crustal Poisson's ratio are shown in Figures 1-9, 1-10, 1-11, 1-12 respectively. A change in crustal P velocity has a very similar effect on waveform as a change in the crustal thickness. This is similarly true for Poisson's ratio. For this reason, we decided to parameterize the inversion in terms of only two parameters; (1) Pn velocity and (2) the crustal thickness. A justification for this approach is that over large regions the mean crustal P velocity is suprisingly constant (at least compared to the variations in crustal thickness). *McConnell* and *McTaggart-Cowan* (1963) compiled all the available refraction results and found that the average crustal P velocity is between 6.0 and 6.2 km/sec down to about 20 km. The scatter in the data is 0.2 km/sec. Also, the range of P velocities which can be simulated with a starting model Green's function are limited due to the changes in the receiver functions and the vertical radiation coefficients. The two-parameter inversion is an approximation, and must be treated as such, but the technique is valuable for comparison of structures of different paths.

The operational procedure which we have developed is to assume a starting model thickness, and then use the absolute travel time of the Pn pulse to determine the Pn velocity. Using this Pn velocity and the starting model thickness the starting model synthetic is computed for the exact epicentral distance. The error function (3.1) is then minimized only in terms of crustal thickness. After 5 iterations the new crustal thickness is used to redetermine the Pn velocity. If it has changed appreciably, then the inversion procedure is repeated with the new Pn velocity. Pn velocity can be determined nearly independent of crustal thickness, and usually does not require adjustment with the new crustal thickness. This can be understood by noting that in the travel time equation (eq. (1.3) in chapter 1) the pr term dominates for direct Pn, and the $\eta_{\alpha}th$ term only amounts to about 5 percent of the total travel time at 1000 km.

Figure 3-2 shows a test of the inversion procedure. The observations are the three fundamental faults, viewed at 1000 km, convolved with a long period WWSSN (15-100) instrument. The observations were generated with a crustal thickness of 40 km and a Pn velocity of 7.8 km/sec. The starting model has a crustal thickness of 32 km and on the basis of timing, the starting Pn velocity is 7.7 km/sec. The synthetic and model parameters for the inversion solution after a single iteration are also shown in Figure 3-2. In all cases the single step inversion model closely matches the observed model.

Figure 3-3 is an example using real data, the 1966 El Golfo earthquake recorded at GOL. The travel path crosses the Colorado Plateau, and the starting model crustal thickness of 32 km is obviously too small. This is most apparent by comparing the relative timing of PL to Pn; the observation is much more disperse. After 5 iterations the inversion has increased the crustal thickness to 46 km, and the fit of the

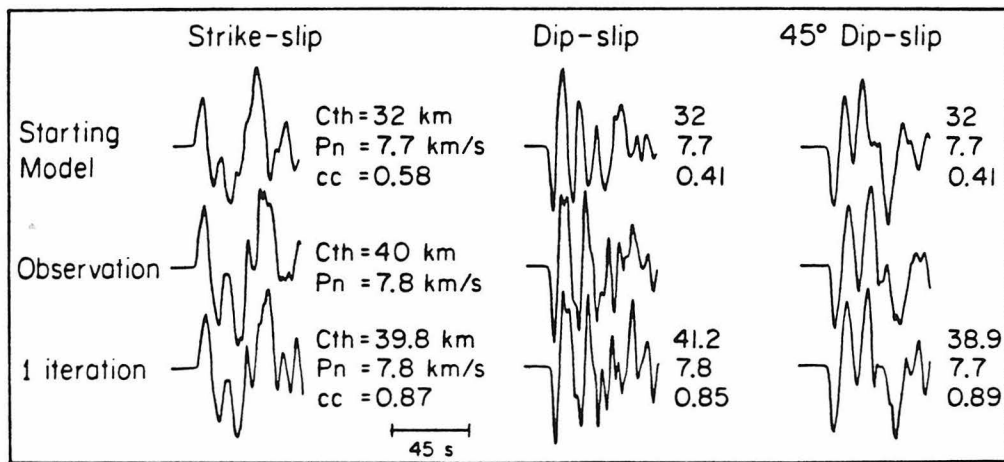


Figure 3-2: A test of the inversion procedure. Cth is the crustal thickness, Pn is the Pn velocity and cc is the cross-correlation coefficient. After a single iteration the inversion returns a structure which is in good agreement with the observed model.

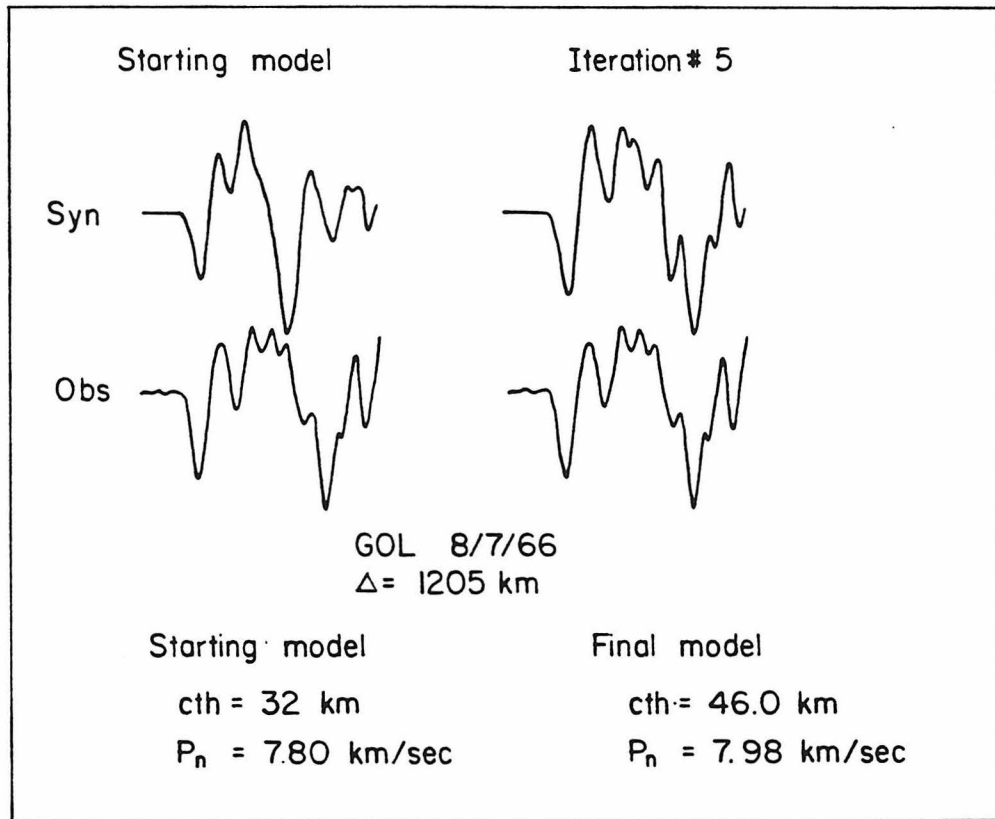


Figure 3-3: Inversion of the P_nI waveform from the 1966 El Golfo earthquake at GOL.

synthetic to the observation is quite good.

An error function (3.1) based on the cross-correlation of the data and synthetic P_{nl} is a very good norm for the problem of structure inversion. The error function is most sensitive to zero crossings, and thus tends to align the peaks, but is not overly sensitive to fine structure in the waveform. Increasing the crustal thickness has, to first order, the effect of stretching out the P_{nl} waveform. This means that the timing of the different peaks changes, which is the quantity to which the error function is most sensitive. Quite often it is impossible to match an observed P_{nl} very well due to the fine detail of the waveform, but nearly always there is a clearly defined minimum in the error function in terms of crustal thickness.

The inversion scheme which was outlined in the preceding paragraphs is based on the idea of an "average" crustal structure along the travel path. If the crust along a given path can be represented as a series of blocks with different thicknesses, or the Moho can be represented as a series of segments with different dips, then the concept of an average crust is sufficient for the purpose of a synthetic P_{nl} . On the other hand, if the Moho has a uniform dip then a flat layered model does a poor job in predicting the observed waveform (this is discussed in more detail in chapter I and Figure 1-15). It would appear that one of the worst possible cases to retrieve structural information would be when there is a uniformly dipping Moho. As a test of the inversion procedure a synthetic with a dipping Moho was used as an observation. The results are summarized in Figure 3-4. The crustal thickness increases from 28 km at the source to 50 km at the receiver which is 1000 km away. The two observations are for (1) a fault which is predominately strike-slip and (2) a fault which is predominately dip-slip. The starting model in the inversion has a crustal thickness of 32 km, and the fit to the observations is poor, both in the timing of the

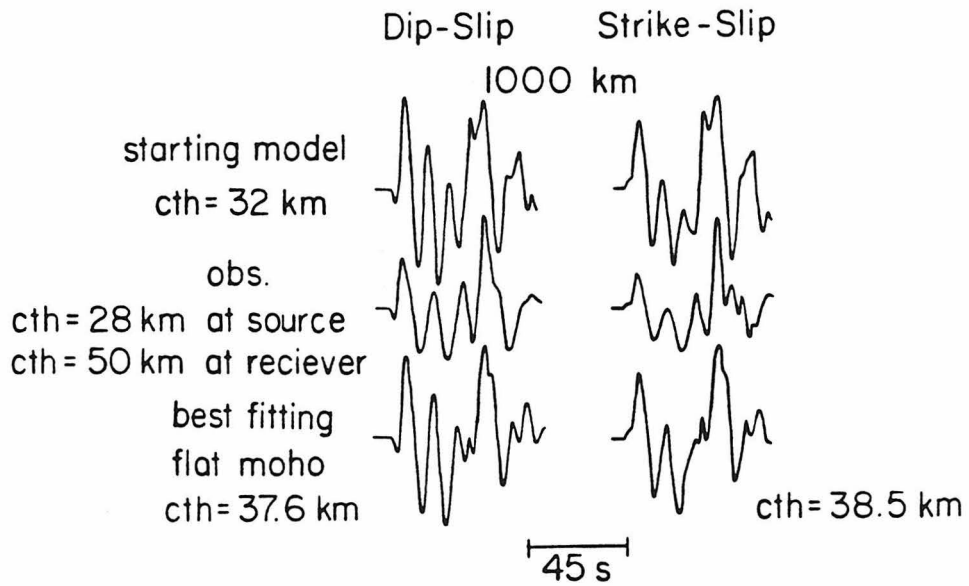


Figure 3-4: Inversion of "data" for a dipping Moho. The starting model thickness is 32 km. The inversion for a flat Moho is shown as the bottom trace in each column (5 iterations).

peaks and the overall shape of the waveform. After 5 iterations the inversion has returned a crustal thickness which is a surprisingly good average of the crustal thickness along the dipping Moho. The fit of the flat Moho synthetic is not particularly good, but the timing of the peaks has been shifted from the starting model. This test gives us confidence that it is possible to retrieve the "average" crustal structure from most P_{nl} records.

3.3 EXAMPLE: THE WESTERN U.S.

The western U.S. is an ideal area to use P_{nl} data to determine the regionalized crustal structure. There are a large number of moderate size earthquakes and 10 WWSSN long-period stations. In addition, there has been a significant number of refraction surveys and surface wave dispersion studies so that the results of the regionalization can be tested. The data base is 10 earthquakes which are listed in Table 3-1. The focal mechanisms of all these events are well known; either with well constrained first motion studies (and some teleseismic modeling) or with the inversion of P_{nl} data as described in chapter II.

Once the "average" crustal parameters are known for a large number of paths in an area, the regionalized map is produced by a least-squares inversion. The area is divided into a set of provinces or blocks and the ray paths criss-cross this network. We assume that the average thickness and Pn velocity of a given path are the sum of the percentage of travel path in a given block multiplied by the thickness or the Pn velocity of that block. In other words;

$$\bar{x}_j = \sum_{i=1}^n x_i \frac{d_{ij}}{D_j} \quad (3.4)$$

TABLE 3-1				
Earthquake sources				
Date	OT	Lat(N)	Long(W)	Depth
5/27/80	14:51	37.506	118.826	14.0
6/09/80	03:28	32.220	114.985	5.0
8/16/66	18:03	37.420	114.190	6.0
12/22/64	20:55	31.810	117.130	8.0
3/28/75	02:31	42.061	112.548	8.0
9/12/66	16:41	39.438	120.160	10.0
1/24/80	19:00	37.852	121.815	11.0
8/06/66	17:36	31.720	114.420	10.0
3/15/79	21:07	34.317	116.450	2.0
10/4/78	16:42	37.493	118.678	8.0

where \bar{x}_j is the average parameter for path j , x_i is the like parameter for block i , d_{ij} is the distance traveled in block i by the ray path j , and D_j is the total ray path length. The least-squares formulation is:

$$\Phi = (A^T A + \sigma I)^{-1} A^T V \quad (3.5)$$

where A is a $N \times n$ matrix (N is the number of travel paths, while n is the number of blocks) which contains the d_{ij}/D_j terms. V is a $N \times 2$ matrix which contains the average crustal thickness and P_n velocity for each path. The values assigned to each block are sensitive to the density of the ray paths which cross it; the ideal case is to sample a block from all directions. Unfortunately, this is seldom the case. It is possible to check the dependence of the value determined for one block on another by looking at the $A^T A$ matrix. If the diagonal terms are much larger than the off diagonal terms then the blocks are relatively independent. On the other hand, if certain off diagonal terms are large compared to the diagonal then blocks are coupled. The most common example of this is when the ray paths are all in one direction; to sample block A the ray path must always cross block B . The interpretation of any results for the inversion should always be considered with this in mind.

We have divided the western U.S. into 10 blocks on the basis of surface geology. The provinces are shown in Figure 3-5. Care was taken to make the blocks big enough so that they are adequately sampled, but at the same time they can not be so big as to smooth out the type of variations which are interesting. For this reason the Basin and Range was divided into three blocks, and a transition was put in between the northern Basin and Range and the Colorado Plateau. The coastal province (#2 in Figure 3-5) is actually in exclusion of the oceanic material. Figure 3-6 shows the different ray paths for the 10 events and recording stations. There are

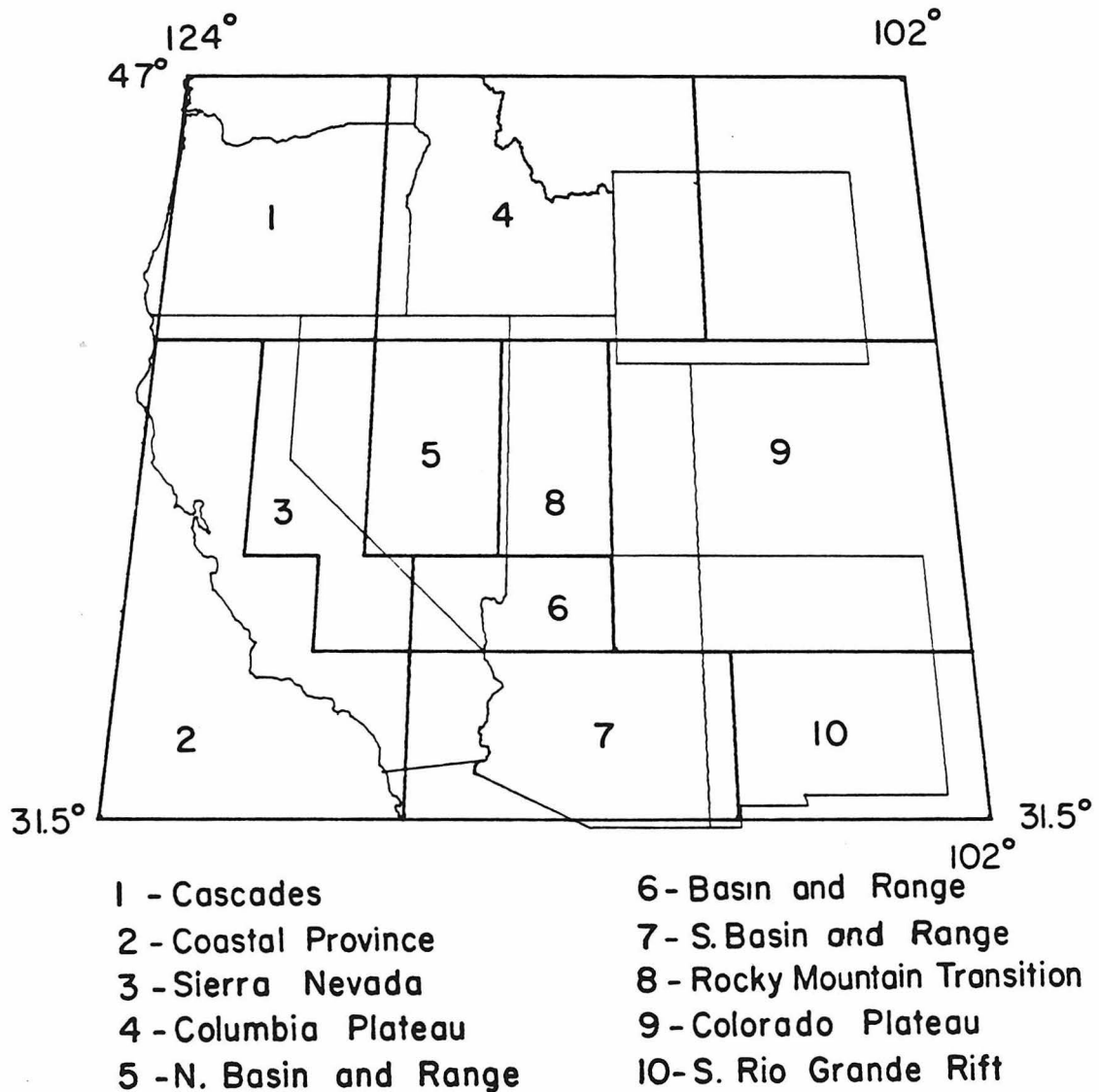


Figure 3-5: Geological provinces used in the regionalized inversion.

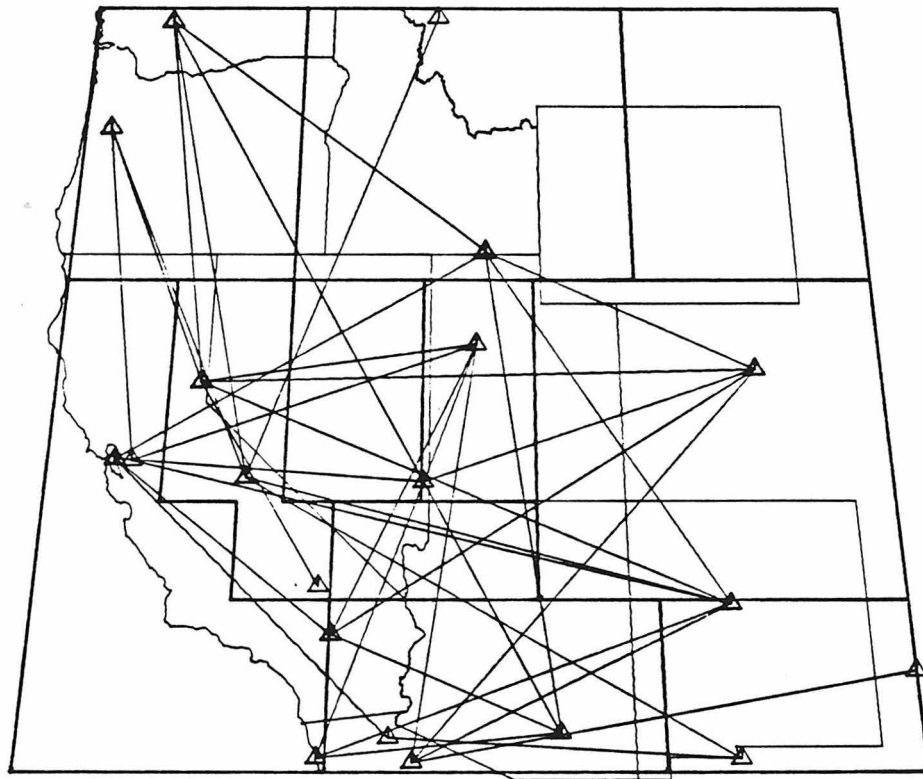


Figure 3-6: Ray paths for the earthquake-receiver pairs used in the regionalization.

47 ray paths shown here. The blocks in the center of the grid (Basin and Range, Sierra Nevada and Rocky Mountain transition) are well sampled, but some of the border blocks are poorly sampled. In particular, the southern Rio Grande Rift has essentially one ray path. One of the most common criticisms of using earthquake travel times for Pn velocities is the relatively poor quality of the origin time. By mixing many travel paths the effect of inconsistent data is minimized.

The results of the inversion are shown in Figure 3-7. The dominant feature is the Colorado Plateau. As expected, it has a crustal thickness which is much thicker than the surrounding area. The northern Basin and Range shows some crustal thinning. There is not a particularly big crustal thickness signature of the Sierra Nevada, but considering that other studies have shown that the Sierra Nevada root is a narrow feature (*Hill, 1978, Smith, 1978*), there probably is not adequate path sampling along its spine. In addition some of the Basin and Range is lumped into the northern part of the Sierra Nevada block. As for Pn velocities, the Basin and Range and Rocky Mountain transition is uniformly low. The Pn velocity of the Colorado Plateau is quite high (compared to 8.1 of *Jaksha and Evans, 1982*), and may represent some trade off with crustal thickness. The crustal thickness in the southern Rio Grande Rift is unexpectedly large, but considering that the solution is dependent on a single ray path, this value should be weighted low.

It is interesting to compare the results of the P_{nl} regionalization with a compilation of refraction and surface wave dispersion studies. Figure 3-8 shows our regionalized crustal thickness and superimposed on it are contours taken from *Soller et al. (1980)*. The agreement is surprisingly good. Where several contours cross a block, such as in the central Basin and Range, the P_{nl} inversion value of crustal thickness is very close to the average of the contours. As stated before, the one

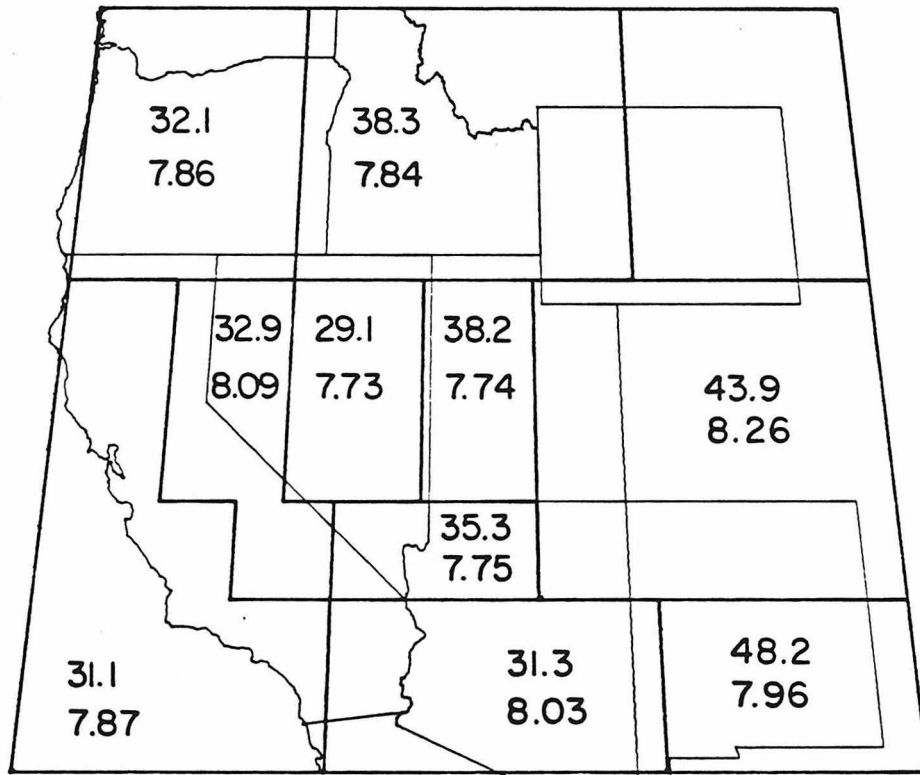


Figure 3-7: Regionalization of the western U.S. on the basis of *Pn* inversion. Top number in each block is the crustal thickness in km and the second number is the *Pn* velocity in km/sec.

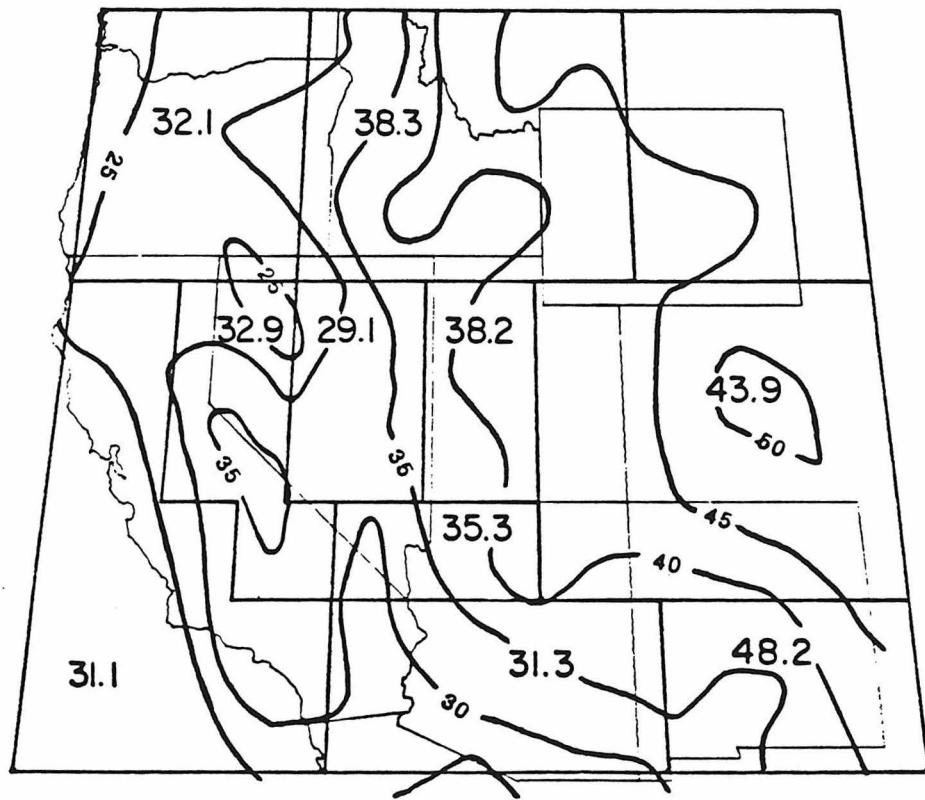


Figure 3-8: A comparison of the regionalization done with *Pnl* inversion and compilation of refraction surveys and surface wave studies. The heavy contours were taken from *Soller et al.* (1980).

region which is in severe disagreement is the Southern Rio Grande Rift. There is little doubt that more earthquake paths should be used before the regionalized structure is complete, but it is apparent that the technique of inversion of P_{nl} data for crustal structure is quite useful.

The mean crustal P and S velocities probably do show some variation in the western U.S. For example, *Warren* (1969) has shown a well developed Conrad near the Mogollon rim (southern part of the Colorado Plateau). In this case, the assumption of the constant crustal velocities results in a thinner crust than is actually present. The differences are small. The paths which crossed the Colorado Plateau were reinverted using a mean crustal P velocity of 6.4 km/sec. The new regional value for the crustal thickness of the Colorado Plateau was 46.2 km and the Pn velocity 8.18 km/sec. Considering the gross scale of the regionalization, these differences are not significant.

3.4 DISCUSSION

One of the most difficult problems in seismology is separating the effects of the seismic source and propagation. In chapter II it was shown that at long periods the P_{nl} waveforms are insensitive enough to fine details of the crustal structure to extract the source parameters of moderate-size earthquakes. This is a result of the long-period nature of the waveform. At higher frequencies an average model for a region as large as the western U.S. simply is not sufficient. If the seismic source information is to be retrieved from a higher frequency recording a regionalized crustal structure should be used. The development of structural models such as in Figure 3-7 will be helpful in studying the source parameters of earthquakes with magnitudes less than 5. Events of this size seldom write long-period records but are well

recorded on broad band instruments such as the Benioff 1-90. The same is true for studying historic earthquakes. There were over 50 events with magnitude greater than 6 in the western U.S. between 1932 and 1960. The waveforms of most of these events have not been studied in detail because the recording instruments are short period and low gain (for example, the Wood Anderson torsion). Determining the detailed mechanisms and moments of these events would be a valuable addition to the earthquake catalogue which presently contains just location and magnitude.

Using P_{21} to determine gross crustal structure should be valuable in regions which are inaccessible to refraction work. Most refraction surveys have been conducted in North America or Europe. Regions such as South America and southern Africa are ideal for the type of analysis discussed here.

3.5 CONCLUSIONS

Long-period regional body waves can be inverted for crustal structure. The procedure makes use of the fact that small changes in structure can be expressed, to first order, in terms of timing of the different arrivals. There is almost always a clearly defined minima in the cross-correlation error function in terms of crustal thickness and P_n velocity. If the average structure of many paths are known, then the information can be combined to produce a regionalized map. The quality of the regionalization depends on the path coverage, but in general the technique can be used as an alternative to refraction studies for gross structure.

REFERENCES

- Black, P.R. and L.W. Braile (1982). Pn velocity and cooling of the lithosphere, *J. Geophys. Res.*, **87**, 10557-10568.
- Braile, L.W., R.B. Smith, J. Ansorge, M.R. Baker, M. Sparlin, C. Prodehl, M.M. Schilly, J.H. Healy, St. Mueller, and K.H. Olsen (1982). The Yellowstone-Snake River plain seismic profiling experiment: crustal structure of the eastern Snake River plain, *J. Geophys. Res.*, **87**, 2597-2609.
- Hearn, T. (1983). Pn travel times in southern California (submitted to *J. Geophys. Res.*, 1983).
- Hill, D.P. (1978). Seismic evidence for the structure and Cenozoic tectonics of the Pacific Coast States, in *Cenozoic Tectonics and Regional Geophysics of the Western Cordilera*, *Geol. Soc. Am. Memoir 152*, R.B. Smith and G.P. Eaton, editors, 145-174.
- Jaksha, L.H. and D.H. Evans (1982). Reconnaissance seismic refraction-reflection survey in northwestern New Mexico (abstract), *EOS*, **63**, 1036.
- Langston, C.A. and D.V. Helmberger (1974). Interpretation of body and Rayleigh waves from NTS to Tucson, *Bull. seismo. Soc. Am.*, **64**, 1919-1929.
- Pakiser, L.C. (1963). Structure of the crust and upper mantle in the western United States, *J. Geophys. Res.*, **68**, 5747-5756.
- Pollack, H.N. and D.S. Chapman (1977). On regional variation of heat flow, geotherms, and lithospheric thickness, *Tectonophysics*, **38**, 279-296.
- Polyak, B.G. and Ya. B. Smirnov (1968). Relationship between terrestrial heat flow

- and the tectonics of continents, *Geotectonics*, 4, 205-213.
- Poupinet G. (1972). PL waves and crustal structure in Canada, *Can. J. Earth Sci.*, 9, 1014-1029.
- Prodehl, C. (1970). Seismic refraction study of crustal structure in the western United States, *Bull. Geol. Soc. Am.*, 81, 2629-2646.
- Smith R.B. (1978). Seismicity, crustal structure and intraplate tectonics of the interior of the western Cordillera, in *Cenozoic Tectonics and Regional Geophysics of the Western Cordillera*, **Geol. Soc. Am. Memoir 152**, R.B. Smith and G. P. Eaton, editors, 145-174.
- Soller, D.R., R.D. Ray and R.D. Brown (1981). *A Global Crustal Thickness Map*, Phoenix Corp., McLean Virginia.
- Warren, D.H. (1969). A seismic-refraction survey of crustal structure in central Arizona, *Geol. Soc. Am. Bull.*, 80, 257-282.

Chapter IV: Analysis of Several Earthquakes Near the Long Valley Caldera

4.1 INTRODUCTION

The 1980 Mammoth Lakes earthquake sequence represents one of the largest seismic strain release episodes in California since the 1971 San Fernando earthquake. During a 48 hour period which began on May 25, there were four events with $M_L > 6$. Aftershock activity continued for over one year, with a large ($M_L = 5.8$) event occurring on September 30, 1981. The 1980 sequence was part of a general increase in seismicity throughout California (McNally, 1981) in the late 1970s. In addition, the earthquake sequence was preceded by several years of local anomalous seismicity (Ryall and Ryall, 1981a), the onset of which is clearly defined by the October 4, 1978 Bishop earthquake ($M_L = 5.7$). Figure 4-1 locates the epicenter of the three largest events in the May 1980 sequence, two of the largest aftershocks and the 1978 Bishop event.

The earthquakes in Figure 4-1 are associated with the intersection of the eastern frontal fault system of the Sierra Nevada and Long Valley Caldera. Long Valley Caldera is an elliptical depression 30 km by 15 km which was formed by the collapse and subsidence of the area after a violent eruption 0.7 my ago; active volcanism may have taken place as recently as 450 years ago (Bailey et al., 1976). The most important fault in the epicentral region is the Hilton Creek fault, which Bailey et al. (1976) estimate to have undergone several hundred meters of pure normal fault

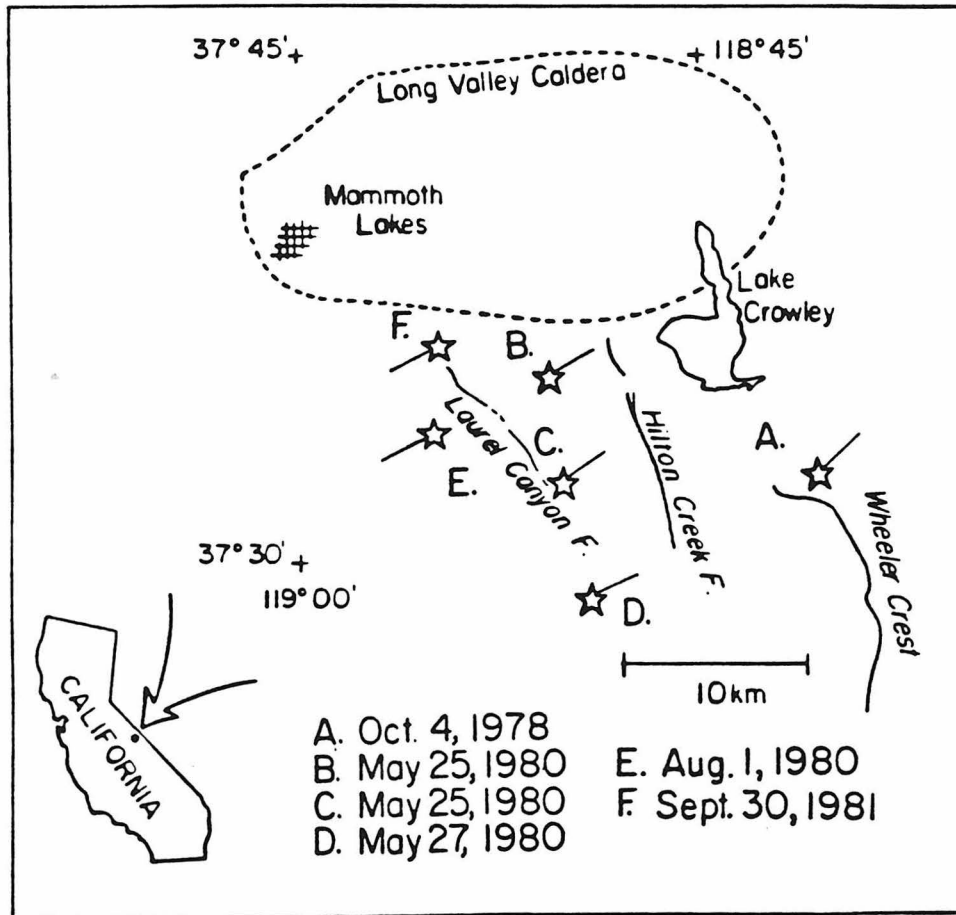


Figure 4-1: Location map of the Long Valley Caldera region. The stars denote the epicenters of the events studied. The lines from each star point in the direction of the T axis determined for the long-period focal mechanism.

displacement since the formation of the caldera. Within the caldera, the offset appears much smaller; *Bailey et al.* (1976) suggest that the motion is taken up on boundary faults to the west and southwest of Long Valley. Extension of the Hilton Creek fault zone into the caldera appears to have occurred as recently as 0.3 my ago, possibly indicating that the caldera had cooled enough by then to support stresses large enough to generate earthquakes.

Surface breakage associated with the 1980 earthquake sequence seems to be confined to the Hilton Creek fault and its extension into Long Valley (*Clark and Yount, 1981; Taylor and Bryant, 1980*). Although earthquakes of this size often rupture to the surface, it is debatable whether this breakage actually represents coseismic fault displacement. The epicenters are located to the west of the surface trace of the Hilton Creek fault (see Figure 4-1). Assuming a 60° eastward dip on the fault plane and a depth of 10 km for the hypocenters, the epicenters would have to be moved almost 10 km to the east if the earthquakes occurred on the Hilton Creek fault.

The strain release of all the earthquakes in Figure 4-1 is complicated. Despite the surface expression of Holocene normal faulting, investigators who have determined the fault mechanisms of the events on the basis of local short-period first motions suggest that the faulting was pure strike-slip on north-south, steeply-dipping planes (*Cramer and Toppozada, 1980; Ryall and Ryall, 1981a*). If the fault plane is taken to be east-west trending, right-lateral slip then this would be compatible with the *Bailey et al.* model of the southwest and west wall of the Long Valley Caldera accommodating movement on the frontal fault system. On the other hand, it is clear from Figure 4-1 that several of the earthquake epicenters are a considerable distance from the Caldera boundary. The strike-slip faulting contrasts

sharply with the modeling of the long-period teleseismic body and surface waves (Given, Wallace and Kanamori, 1982), which indicates an oblique-slip mechanism on moderately dipping ($\sim 45^\circ$) north-south planes. The purpose of this chapter is to investigate this apparent discrepancy between mechanisms determined by the analysis of the long- and short-period waveforms.

4.2 LONG PERIOD MECHANISMS

The primary analysis done was the determination of the source parameter of the six events in Figure 4-1 (and an additional event north of the Caldera) by the modeling of the long-period body and surface waves. Long-period waveform modeling provides a much more robust method of determining the overall or "average" source parameters of an earthquake than analyzing the distribution and polarities of short-period P and S-wave first motions.

The May 1980 Sequence

The first event in the 1980 sequence (event B in Figure 4-1) produced very good surface waves (first and second passage of the fundamental-mode Rayleigh and Love waves) on the Global Digital Seismograph Network (GDSN) and usable body waves on the WWSSN network. The surface waves were inverted for source using the method described by Kanamori and Given (1981). The moment tensor inversion technique works best at long periods where the phase velocity and Q are most accurately known. For event B, the longest period which yielded good results was about 200 seconds. At this period, the Rayleigh-wave amplitude and phase data could be used for determination of the source strength and initial phase. The Love-wave amplitude data were also considered reliable, although the Love-wave phase data

were not used since the phase velocities are not determined accurately enough. At shorter period (<200 secs) we used only amplitude data for both wave types.

The hypocentral depth of the first event was about 10 km, so at periods greater than 100 sec., the source is effectively at the free surface and only three components of the moment tensor, M_{xx} , M_{yy} , and M_{xy} are resolvable (for a discussion of the effect of the free surface on the moment tensor see *Kanamori and Given, 1981*). Fortunately, the constraints introduced from the modeling of the long-period P waves (to be discussed later) help resolve the mechanism. We first inverted for the moment tensor at the periods of 197 and 150 seconds with M_{zz} and M_{yz} constrained to be zero. The results are virtually the same at each period and are summarized as solution 1 in Table 4-1 and Figures 4-2 and 4-3. The moment tensor can be visualized as three orthogonal force couples, given by the eigenvalues and eigenvectors of the moment tensor; a vertically oriented compressional couple of magnitude 1.33×10^{25} dyne-cm, a compressional couple oriented N22°W with magnitude 1.35×10^{25} dyne-dm, and an extensional couple oriented N68°E with magnitude 2.68×10^{25} dyne-cm. The constraints ($M_{zz} = M_{yz} = 0$) limit the solution to be a combination of pure strike-slip fault (strike = N23°E, dip = 45°, rake = -90°, moment = 1.33×10^{25} dyne-cm). This result can be interpreted in two ways: (1) the source is complex and cannot be represented by a single fault model, or (2) the existence of the second fault is an artifact of the constraints $M_{zz} = M_{yz} = 0$, and the source can be represented by a single fault with significant oblique slip.

Assuming that the single fault model is correct, we first found the double-couple solutions consistent with solution 1 in Table 4-1 which have the minimum scalar moment. Then, using the long-period teleseismic first motions and the alignment of epicenters the mechanism was determined to be: strike = N12°E, dip = 50°, rake =

TABLE 4-1

<u>Event 1</u>	<u>T = 197 sec</u>	<u>T = 150 sec</u>
<u>Solution 1</u>	$M_{xz} = M_{yz} = 0$, Constrained	
M_{xy}	-1.28 ± 0.15	-1.42 ± 0.11
$M_{yy} - M_{xx}$	3.11 ± 0.24	2.99 ± 0.19
$M_{yy} + M_{xx}$	1.33 ± 0.22	1.59 ± 0.16
RMS error	1.937	1.732
<u>Solution 2</u>		
M_{xy}	-1.28	-1.28
$M_{yy} - M_{xx}$	3.09	3.09
$M_{yy} + M_{xx}$	1.50	1.50
θ	12° (126°)	12° (126°)
δ	50° (64°)	50° (64°)
λ	-35° (-134°)	-35° (-134°)
M_o	2.85	2.85
RMS error	1.955	1.706
<u>Solution 3</u>	Best 45° dip-slip solution	
θ	-20° (160°)	-21° (161°)
δ	45° (45°)	45° (45°)
λ	-90° (-90°)	-90° (-90°)
M_o	2.56	2.56
RMS error	2.600	2.57
<u>Solution 4</u>	Best strike-slip solution	
θ	27° (-63°)	28° (-62°)
δ	90° (90°)	90° (90°)
λ	0° (0°)	0° (180°)
M_o	2.07	2.15
RMS error	2.384	2.65

θ , δ , λ , M_o : strike, dip, slip, moment.

Auxiliary planes are given in parentheses.

All moments in units of 10^{25} dyne-cm.

RMS error units are 10^{-2} cm-sec.

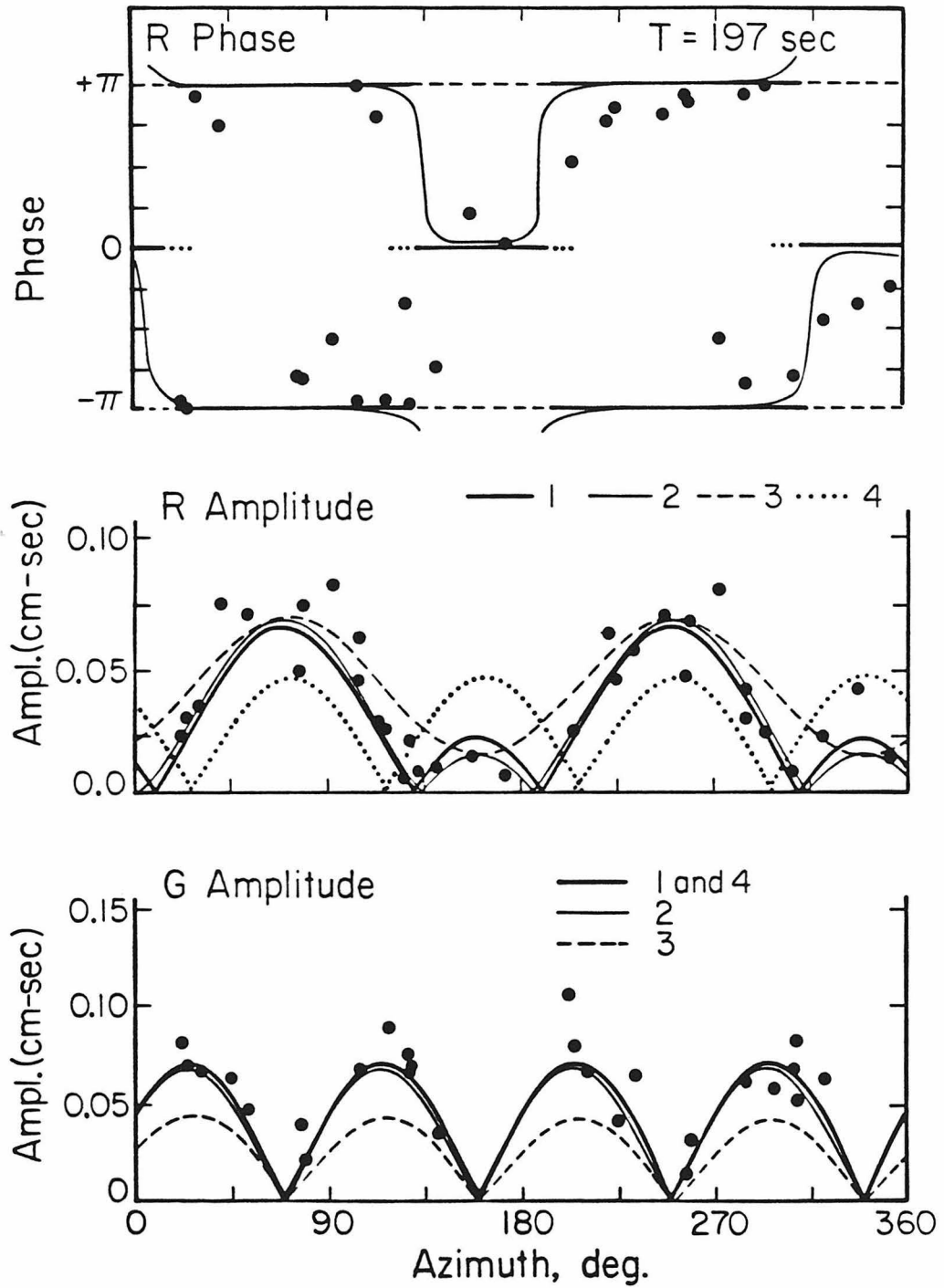


Figure 4-2: Inversion results at period of 197 sec. The numbers refer to source models in Table 4-1. Poorly fitting phase data is associated with low-amplitude signals.

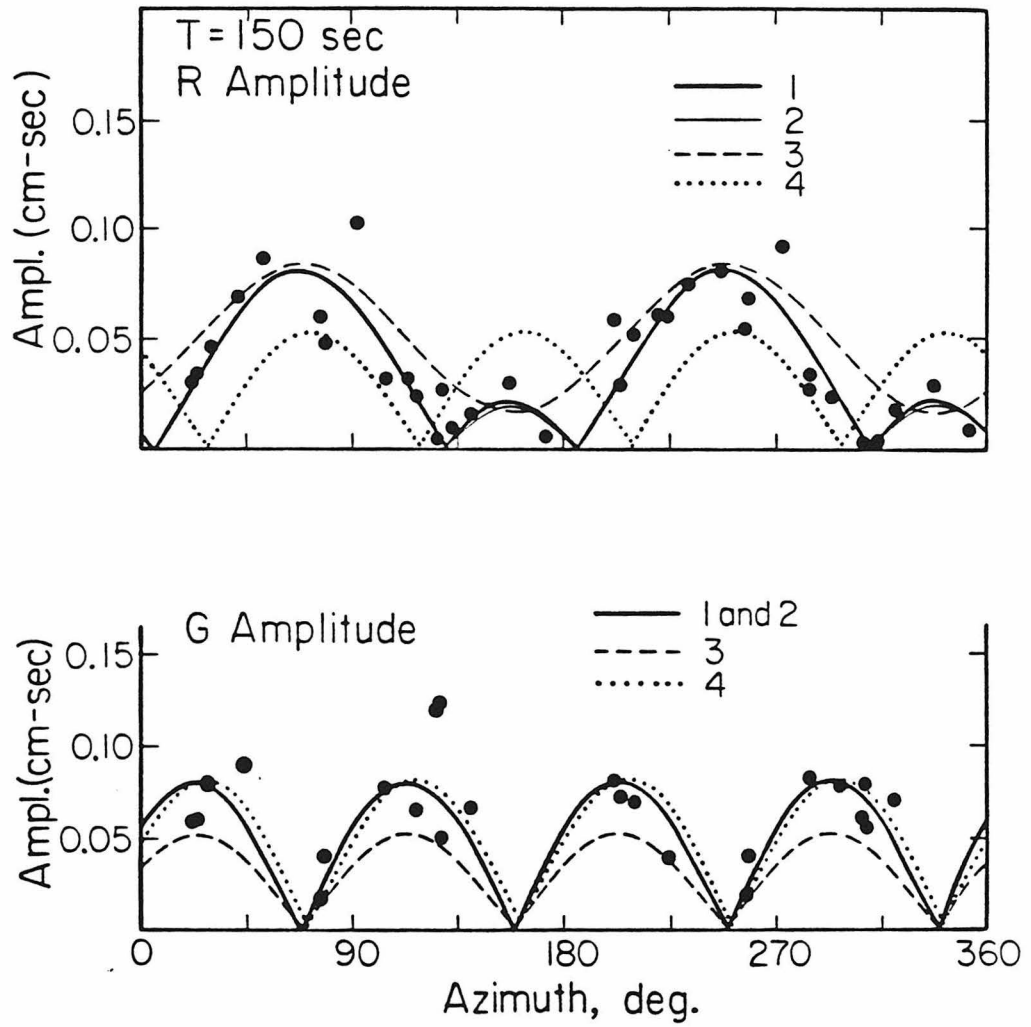


Figure 4-3: Inversion results from amplitudes only at a period of 150 sec. See Table 4-1 for details of the models.

-35°, and the moment = 2.85×10^{25} dyne-cm. Figure 4-4 shows the fault and the long- period first motions. The fit of this solution is shown in Table 4-1 and Figures 4-2 and 4-3.

We examined other possible solutions by constraining the solution to be either a pure strike-slip fault (as suggested by *Cramer and Topozada*, (1980); and *Ryall and Ryall* (1981a)), or a dip-slip fault (from consideration of the major geologic structures in the area). The solutions are all compared in Figure 4-2 and 4-3 and Table 4-1. From the rms of the error it is clear that neither is as good a solution as the oblique-slip mechanism.

The other two large events in the Mammoth Lakes sequence (events C and D in Figure 4-1) are noticeably different from the first, largest event. Figures 4-5 and 4-6 show a comparison of the filtered seismograms for the three events. In these figures, the amplitude scale is the same at a given station although it varies from station to station. The azimuthal distribution of the spectral amplitudes (at a period of 150 seconds) of the equalized surface waves from event B are shown in Figures 4-5 and 4-6. These are given to show where on the radiation pattern the seismograms are from and to give an approximate idea of the scaling used to plot each seismogram. For receivers in loop directions (e.g. the Rayleigh waves at SNZO, BCO, CTAO, and KONO and the Love waves at SNZO, MAJO, BOCO, GUMO, and KONO), the waveforms for all the events appear very similar, with the first event consistently about twice as large as the second, which in turn is slightly larger than the third event. However, the Rayleigh waves at certain nodal stations are quite different. Specifically, R_1 and R_2 for CHTO is larger than the second event than for the first; GUMO, although quite visible for the first event, is nodal for the second; GAR and CMO show very similar levels of excitation for the first two events; and BOCO and MAJO

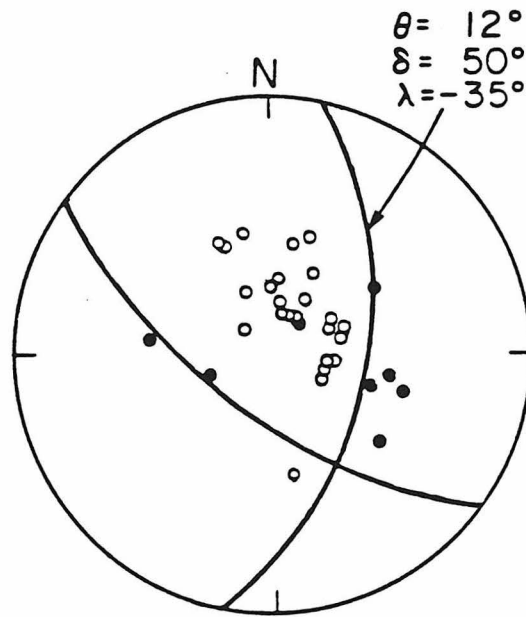


Figure 4-4: Long-period first motion data and mechanism for event B.

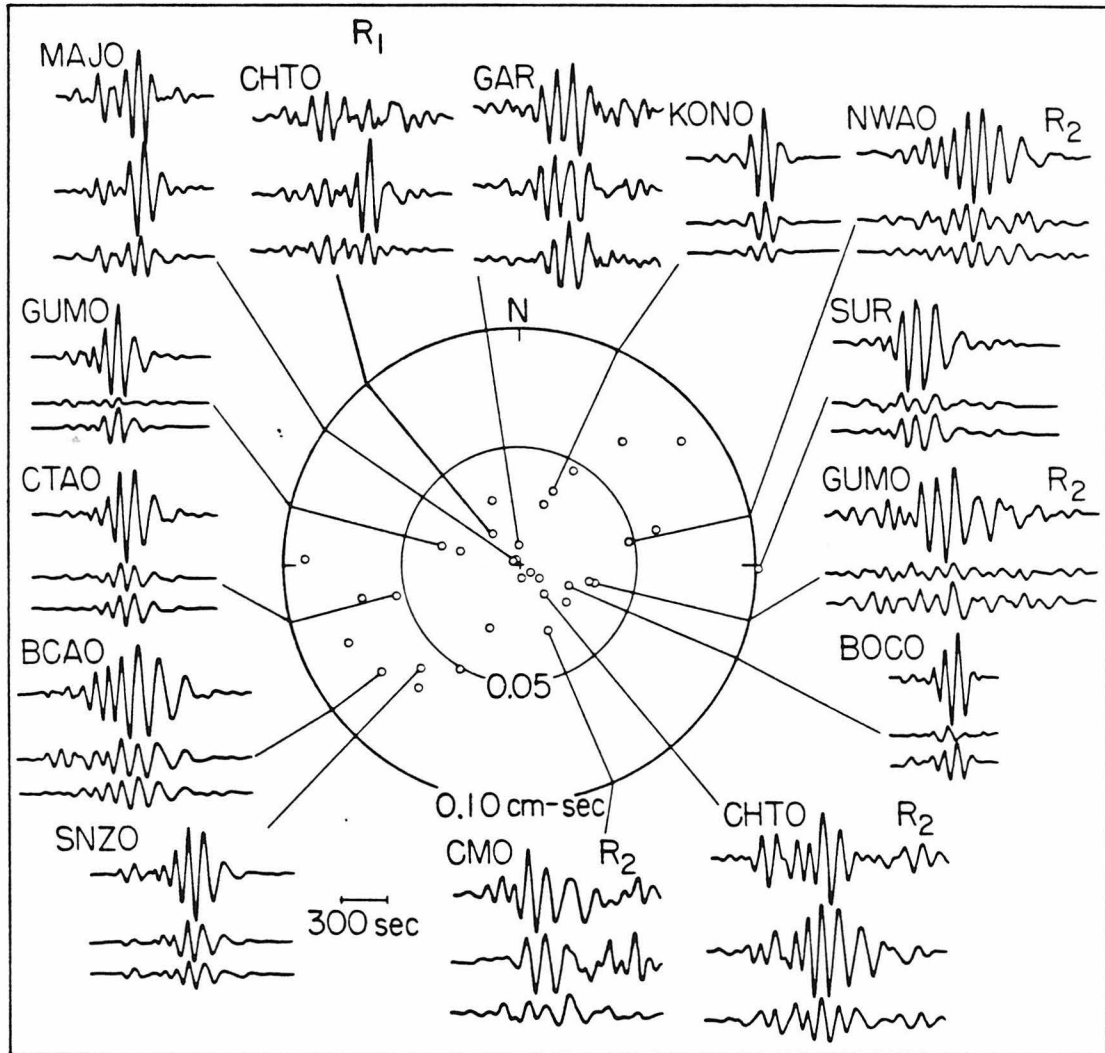


Figure 4-5: Representative sample of Rayleigh waves used in this study. The seismograms have been filtered with a band-pass filter between 80 and 1500 sec. At each station, the amplitude scale is the same; the amplitude scale varies from station to station. The radiation pattern at 150 sec for event B, corrected for propagation, is plotted in the center of the Figure.

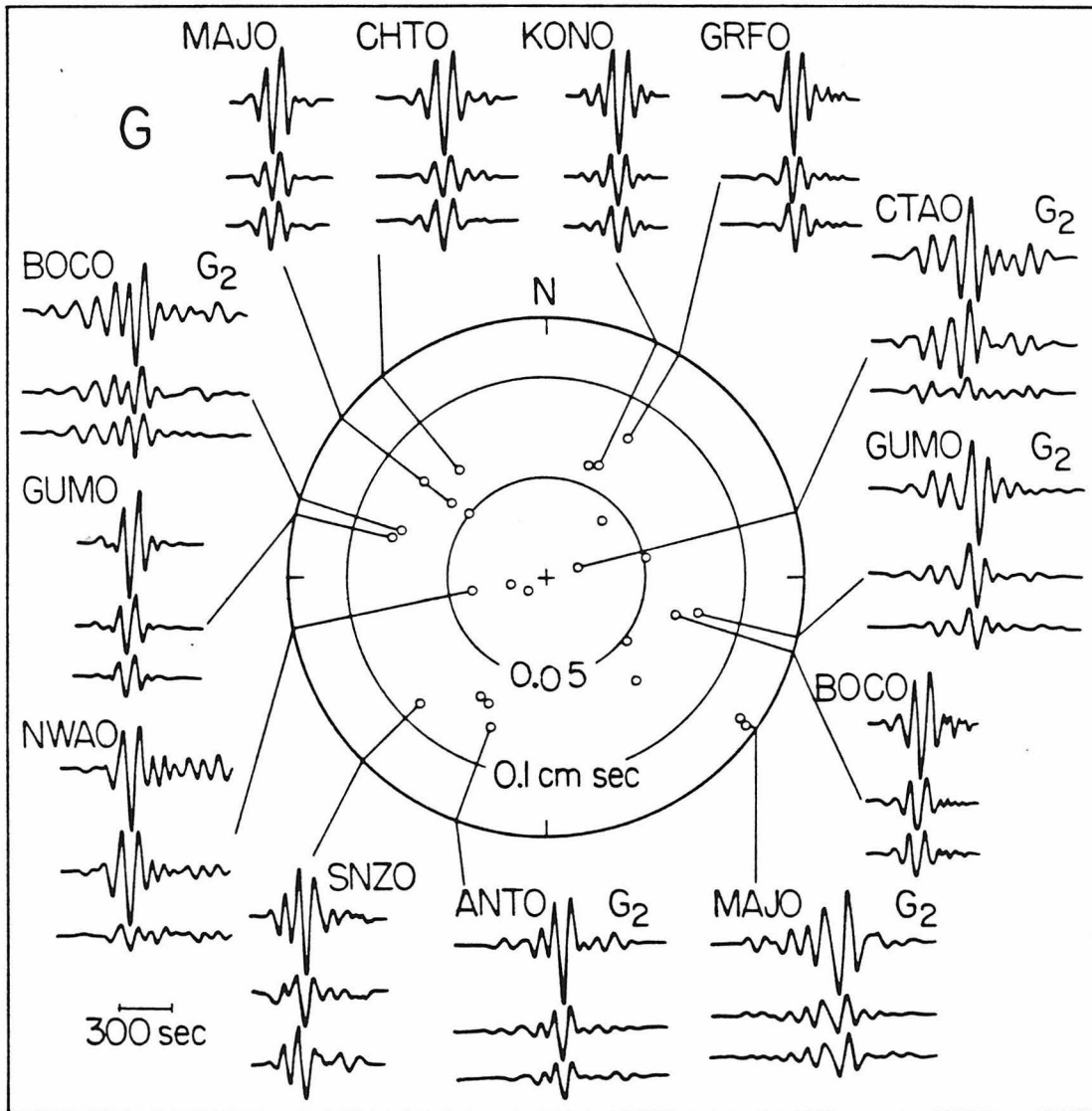


Figure 4-8: Sample of the Love waves used in this study. The filter and amplitude scale variation is the same as Figure 4-5.

Rayleigh waves show a change in phase between the first two events. All of these differences suggest a Rayleigh-wave radiation pattern for the second event which is more four-lobed than the first event, indicating a mechanism with more of a strike-slip component.

Events C and D were too small to invert accurately using the scheme used for event B. We therefore devised a relative inversion technique which used the differences apparent in waveform amplitudes and therefore reduced errors due to inadequate knowledge of the propagation path. The results of the relative inversion for event C are shown in Figure 4-7 and Table 4-2. Solutions 1 and 2 in Table 4-2 fit the data equally well. For solution 1 the mechanism was constrained to be on a fault plane with the same dip angle as the source model preferred for event B. The slip angle is much less, as we expected from visual examination of the seismograms. The strike is virtually identical, indicating that the first and second events in the 1980 sequence could have occurred on a plane of similar orientation. The second mechanism, which was obtained without constraints, has a large strike-slip component. It must be remembered that the dip angle is poorly resolved.

The results of the inversion of event D are given in Figure 4-8 and Table 4-3. Although the differences between events B and D are more subtle, a fault model with a similarly oriented plane, but with more strike-slip motion, is preferred on the basis of a smaller rms of error. The mechanisms derived for C and D depend on the solution chosen for B. Specifically, the excitation of M_{xx} and M_{yz} terms become large enough at 80 seconds to contribute to the solution; these components are poorly constrained for the first event. In terms of fault-plane parameters, these components relate to the dip of the fault plane which we have fixed by the long-period body wave modeling.

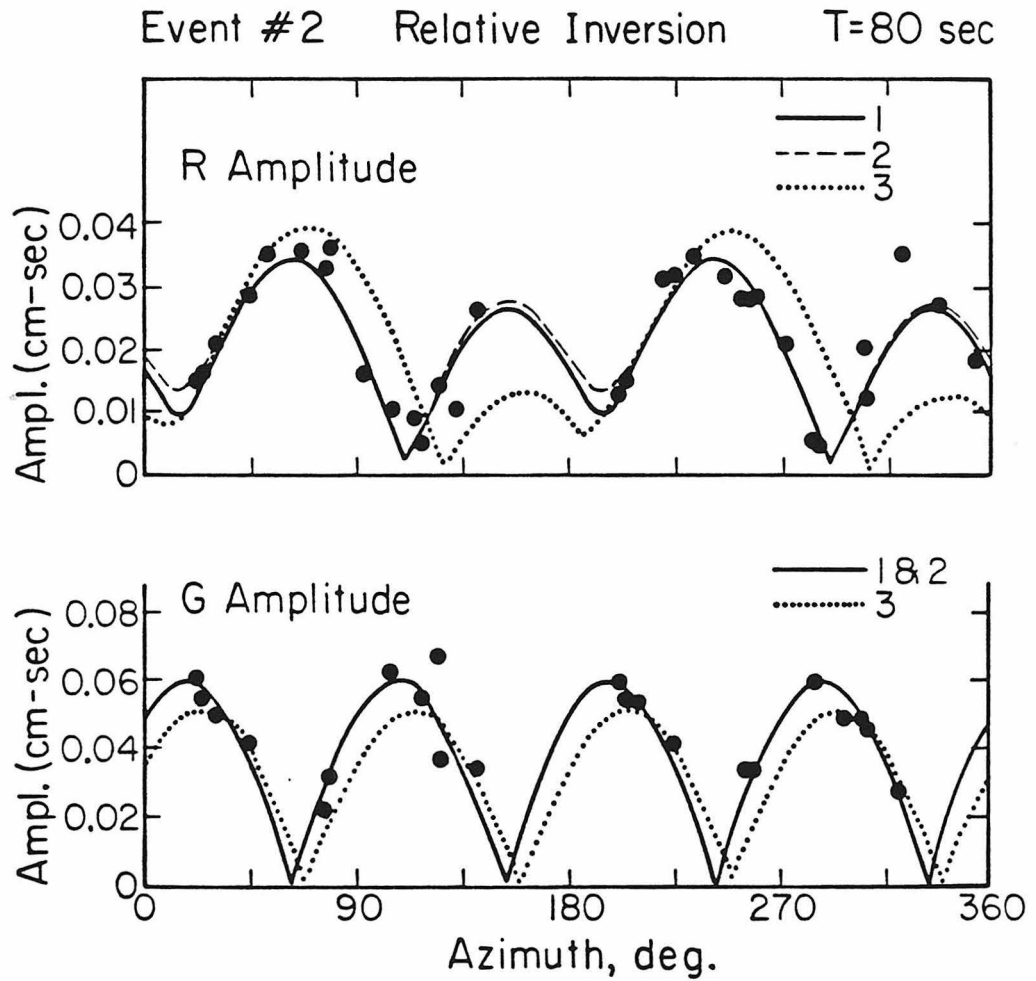


Figure 4-7: Results of the inversion of relative amplitudes for the second event (event C). Model details are given in Table 4-2.

TABLE 4-2

Event 2

Solution	1	2	3
	(δ fixed)	(unconstrained)	(θ, δ, λ fixed)
θ	15° (111°)	16° (111°)	12°
δ	50° (82°)	40° (85°)	50°
λ	-10° (-140°)	-7° (-130°)	-35°
M_o	1.27	1.50	1.22
RMS error	0.505	0.510	0.983

Event #3 Relative Inversion T=80 sec

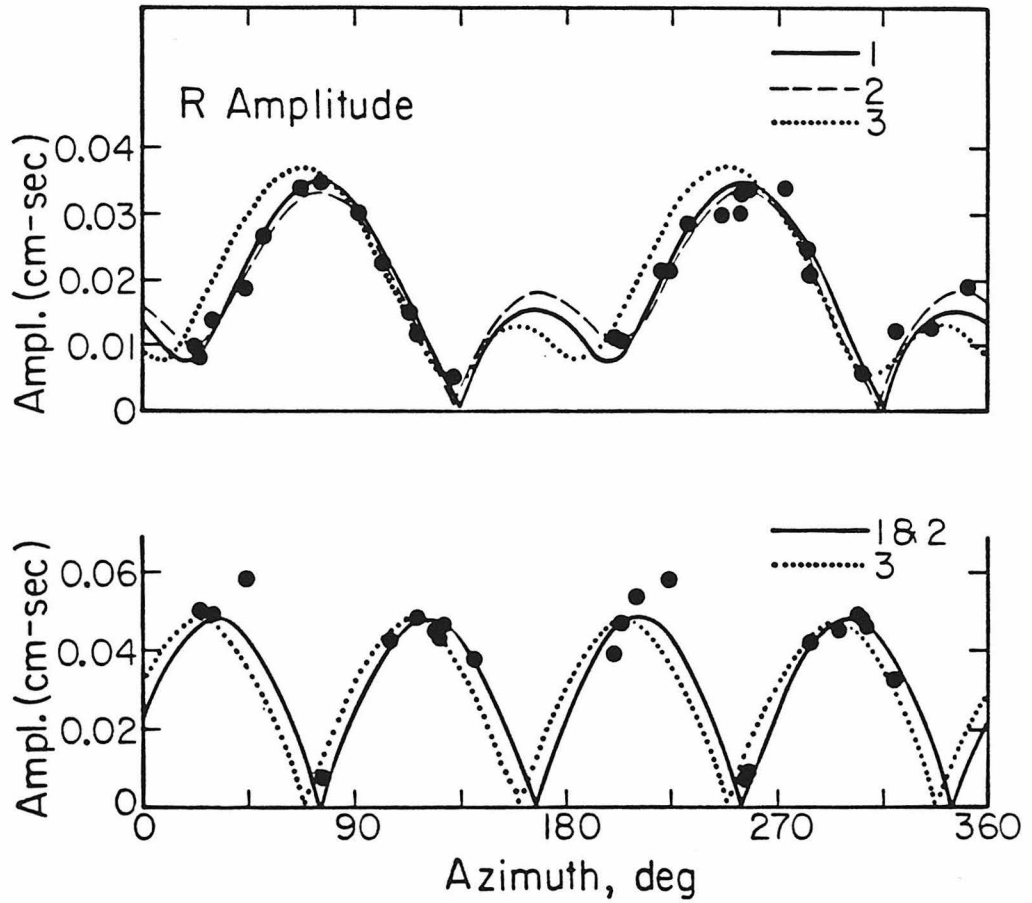


Figure 4-8: Results of the inversion of relative amplitudes for the third event (event D). Mechanism details are given in Table 4-3.

TABLE 4-3

Event 3

Solution	1	2	3
	(δ fixed)	(unconstrained)	(θ, δ, λ fixed)
θ	22° (131°)	25° (129°)	12°
δ	50° (69°)	42° (77°)	50°
λ	-28° (-136°)	-19° (-130°)	-35°
M_o	1.10	1.21	1.13
RMS error	0.432	0.402	0.660

The long-period P waves from the three events in the 1980 sequence are well recorded at teleseismic distances, and they provide a valuable constraint in the surface wave inversion. Figure 4-9 shows a representative sample of the long-period P waves. For a given station, there are one, two, or three records; if a single seismogram is shown, it is for the first event (event B), if two seismograms are shown they are for the first and third events (B and D), otherwise all three events are shown. The maximum amplitude of the upswing of a given seismogram is shown to the right of the trace. Two features are apparent from the figure: (1) the first event has a consistent double-pulse nature which suggests a multiple source, and (2) the amplitude of the second event is down by a factor of at least 2 in comparison to the third event. In fact, the body waves of the second event are so small that they could seldom be observed, hence the paucity of the waveforms in Figure 4-9. This is surprising since the surface-wave moments of the second and third events are nearly identical. The principal difference between the first and third events other than the source complexity is the relative importance of the second downswing.

We have attempted to match the observed P-waves with synthetic seismograms computed with generalized rays for a point-shear dislocation (see *Helmburger*, 1974; *Langston and Helmburger*, 1975). There are three basic rays which are used; P, pP, sP. The synthetic seismogram is the sum of the displacements convolved with an instrument, an attenuation operator, and a source time function. Only P waves recorded at distances beyond 30° were modeled. A Futterman attenuation operator with $t^* = 0.75$ was used. A half space velocity model ($\alpha = 6 \text{ km/sec}$, $\beta = 3.4 \text{ km/sec}$, $\rho = 2.7 \text{ gm/cm}^3$) was used and the appropriate source depths were taken from *Cramer and Topozada* (1980). The modeling procedure was a trial-and-error fit of the synthetics to the observations. The best fit was sought in terms

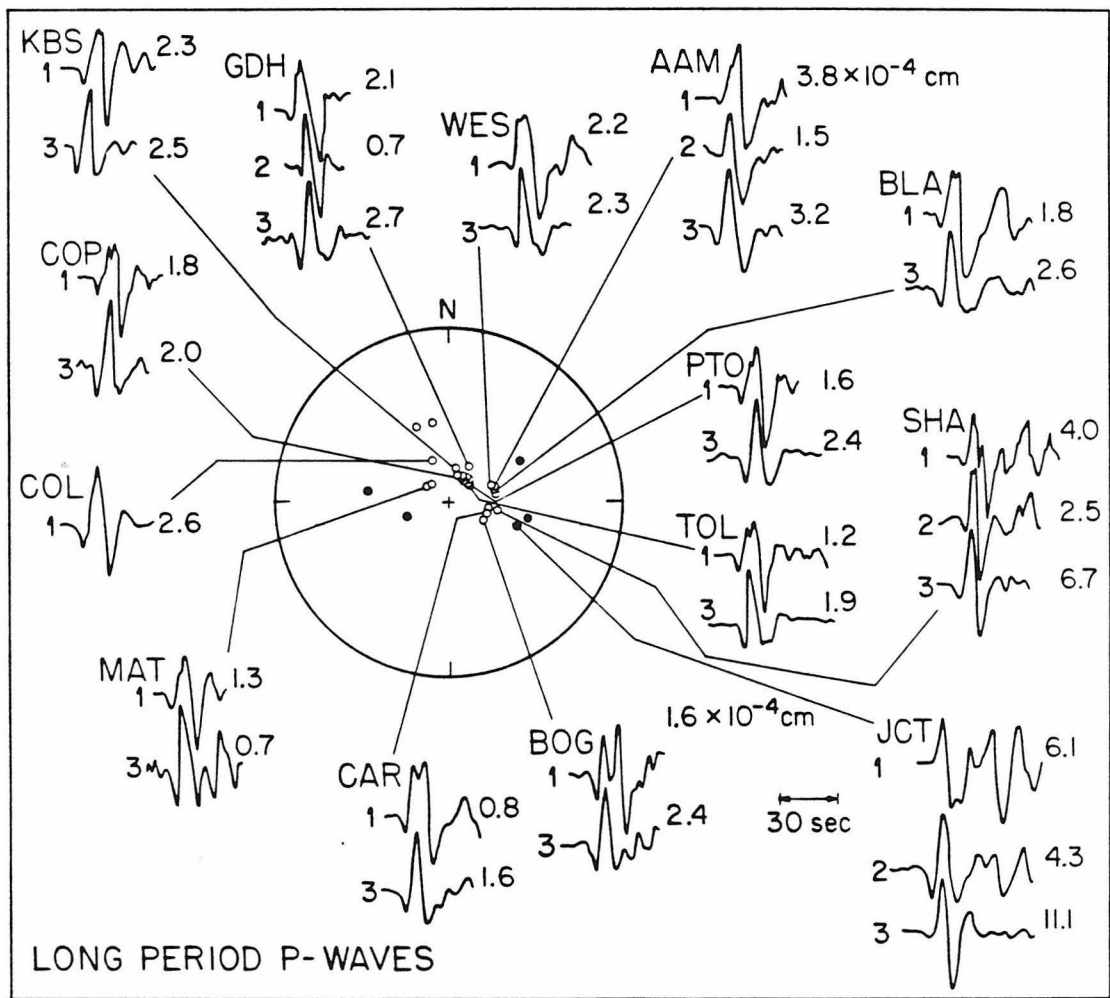


Figure 4-9: A comparison of the long-period P waves for the 1980 Mammoth Lakes sequence. The event number is denoted to the left of each trace and the maximum upswing amplitude is given to the right.

of a time function parameterized by a trapezoid as described by *Helmberger* and *Malone* (1975).

Figure 4-10 shows a comparison of the synthetics for the best fitting point-source model and the data for event B. The model has two sources separated in time by 4 seconds. The first source has a depth of 9 km while the second source is 7 km deep. Both sources have a symmetric trapezoidal time function with a rise/fall time of 1 second and a top of 2 seconds; the first source is 80 percent of the size of the second. Both sources are constrained to have a fault orientation of strike = 12° , dip = 50° , and a rake = -35° . In the modeling process, it was assumed that the first source was constrained to have the surface-wave mechanism (which is consistent with the body wave first motion data shown in Figure 4-4) while the second source could be either more dip-slip or strike-slip. Neither case significantly improved the fit, so the starting model was used for both sources. The poorest fitting feature of the waveforms is the large downswing (15 seconds after the first arrival). The relative amplitude of the downswing is consistently 2 to 3 times larger than predicted. We were unable to reproduce this feature with point sources and faulting mechanisms in a half space. One possible explanation is vertical directivity. If the second source ruptured toward the surface, sP and pP would be larger and would give a larger downswing. Synthetics for a finite fault were generated for a fault 5 km long (in vertical dimension) and the downswing increased about 10 percent. It would be hard to justify a much larger fault dimension considering the size of the aftershock zone, so it was decided that the finite fault was not a significant improvement. Similarly, a time function with a sharp rise and a long fall time will increase the downswing, but this also causes a misfit in pulse width.

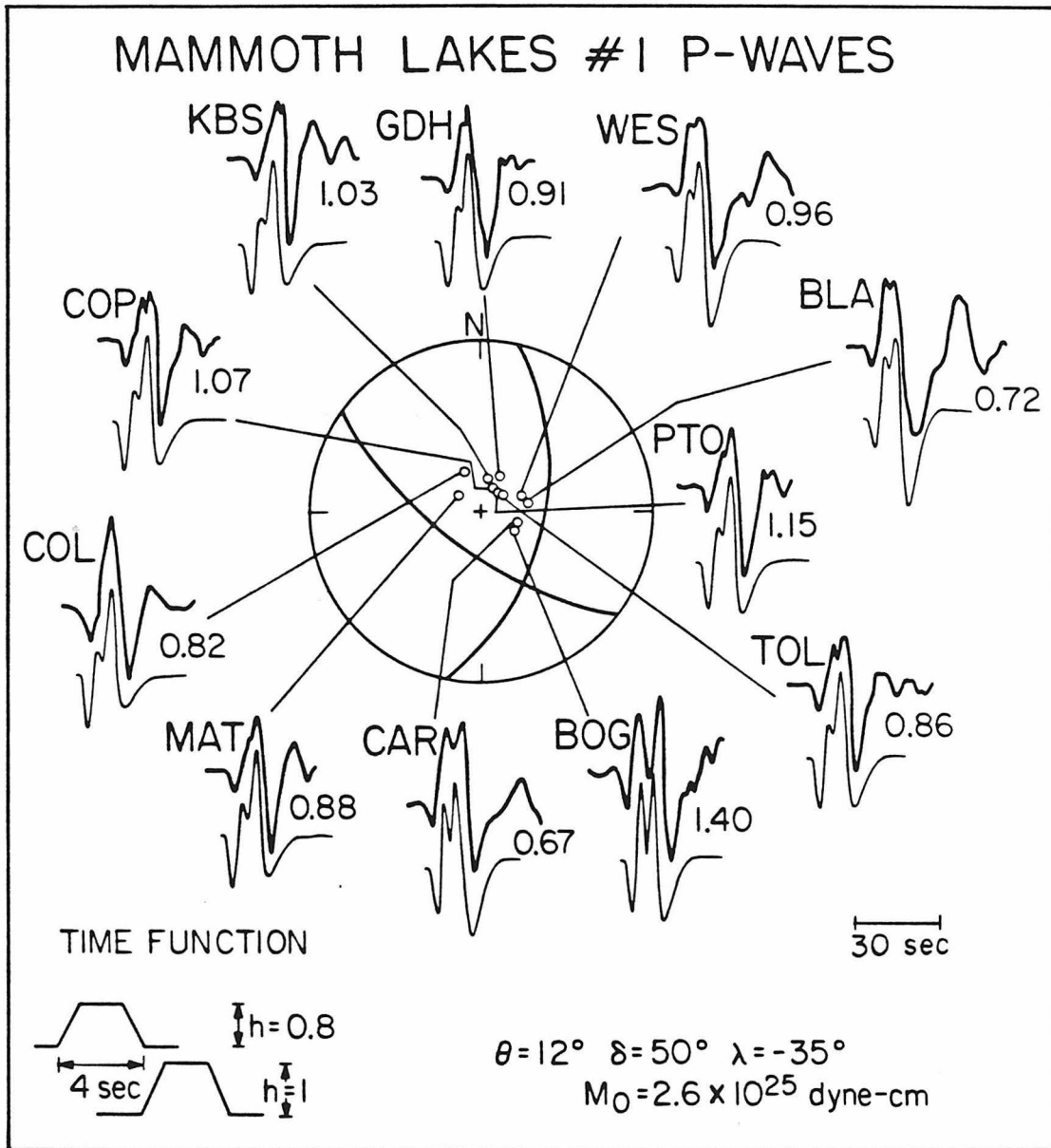


Figure 4-10: A comparison of the teleseismic P waves for event B and synthetics computed for two point sources. The ratio of particular stations moments and the average moment is given to the right of each trace. The time function and mechanism used in the synthetics are shown on the bottom of the Figure.

The body-wave model is based on assumptions which, admittedly, oversimplify the problem. The P-wave fit can probably be improved by a more detailed analysis of the long- and short-period body waves and near-source strong motion data, including in the analysis the effects of source finiteness and crustal structure. However, some general conclusions can be made. There is observable complexity in the body waves which requires at least two distinct sources. An estimate of the moment can be obtained by matching the amplitude of the upswing on each seismogram with the synthetic for that station. The body wave moment was determined to be 2.6×10^{25} dyne-cm which is in excellent agreement with the surface wave determination.

Figure 4-11 shows a comparison of the synthetics for the best-fitting model and the data for event D. The model has a single point source at 15 km depth. The time function has a rise, top and fall time of 2 seconds each. The mechanism is that determined by the surface waves: strike = 22° , dip = 50° , and rake = -28° . The synthetic fits appear quite satisfactory at all stations. The average moment was determined to be 1.2×10^{25} dyne-cm, again in excellent agreement with the surface wave analysis.

As discussed earlier, the waveforms of the second event (event C) were small, and no modeling of them was attempted. A moment can be computed by assuming the surface wave mechanism and comparing the amplitudes at the stations where body waves are observed. The moment was determined to be 0.6×10^{25} dyne-cm. The disparity between the surface wave and body wave moments is perplexing. An obvious explanation is that this event had a low stress drop compared to the other two, but this is not reflected in the M_L 's. ($M_L = 6.0$ for event B, and $M_L = 6.3$ for event C). Table 4-4 summarizes the source parameters of all the events.

TABLE 4-1

Source Parameters

Event	Date	OT	Lat	Long	Depth	Moment	θ	δ	λ^\dagger	P		T	
										ϕ	γ	ϕ	γ
A Bishop	10/4/78	16:42	37.493	118.673	8.0	5.7×10^{24}	290°	70°	235°	-21°	51°	45°	18°
B Mammoth Lakes #1	5/25/80	16:33	37.609	118.846	9.0	2.9×10^{25}	12°	50°	-30°	165°	46°	64°	11°
C Mammoth Lakes #2	5/25/80	19:45	37.562	118.838	15.3	1.3×10^{25}	15°	50°	-10°	161°	34°	57°	21°
D Mammoth Lakes #3	5/27/80	14:50	37.506	118.826	14.2	1.1×10^{25}	22°	42°	-19°	178°	43°	66°	22°
E Mammoth Lakes	8/01/80	16:38	37.554	118.896	5.0	1.5×10^{24}	11°	40°	-34°	176°	53°	63°	17°
F Mammoth Lakes	9/30/81	11:53	37.588	118.887	8.0		14°	50°	-28°	166°	45°	64°	12°
Huntoon Valley	9/07/80	04:36	38.048	118.558	5.5	9.6×10^{23}	67°	85°	-15°	-158°	14°	114°	7°

θ gives the strike of the fault measured clockwise from the north, δ gives the fault dip. Dip direction is always to the right of the strike direction. λ is the rake; rake is the angle of motion of the hanging wall relative to the foot wall (eg. right lateral strike-slip has a rake of 180, while pure normal faulting has a rake of -90). P and T are the most and least compressive stress axes respectively. ϕ is the azimuth and γ is the plunge.

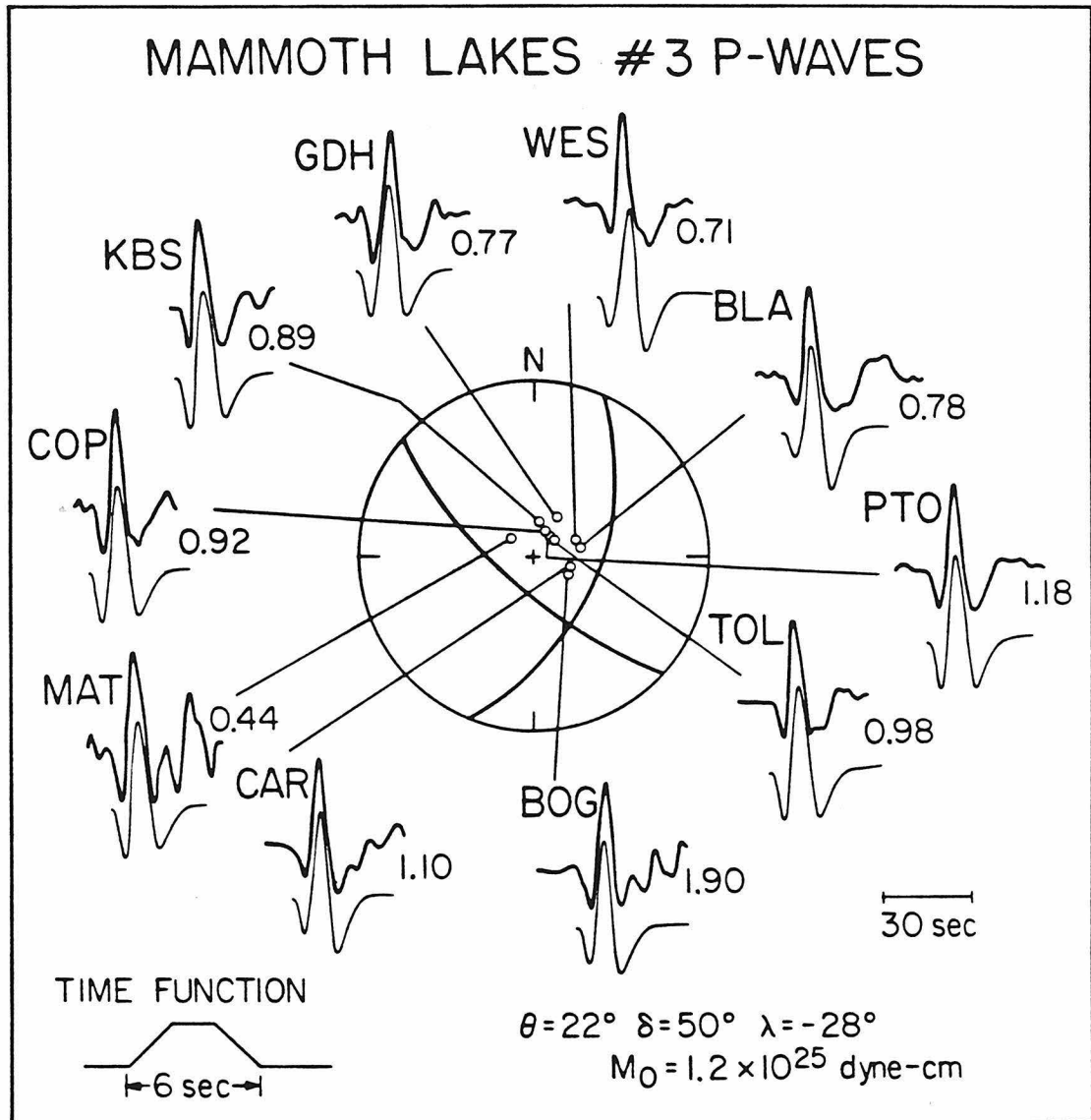


Figure 4-11: A comparison of the teleseismic P waves from event D and the synthetics computed for the time function and mechanism shown. To the right of each trace is the ratio of the stations moment to the average moment.

Aftershocks of the 1980 Sequence and the 1978 Bishop Earthquake

The remaining three events (A,E and F) were too small to produce usable teleseismic surface or body waves, but they did produce good P_{nl} records. As in Chapter II, we assumed the crustal structure and inverted for the source parameters of these events. The two aftershocks (events E and F) have mechanisms which are very similar to event B. The Bishop earthquake has oblique slip on a steeply north dipping plane. The source parameters are summarized in Table 4-4.

An additional mechanism was determined for an earthquake in Huntoon Valley, about 60 km northeast of the Mammoth Lakes epicenters. It was included in this analysis since it was close enough to Long Valley to test the hypothesis that some sort of regional distortion of the long-period waveforms is present, and at the same time it is far enough away to be free of the near source structural complications. The fault mechanism which was determined is essentially pure strike-slip on steeply dipping planes, which is in agreement with the local short-period first motion mechanism (U. Vetter, personal communication, 1982). In Table 4-4 note that there is a clockwise rotation of the P and T axes of the Huntoon Valley event relative to the Mammoth Lakes events.

4.3 COMPARISON BETWEEN THE LONG- AND SHORT-PERIOD MECHANISMS

We did a simple comparison of the focal mechanisms determined on the basis of local P-wave first motions with those determined by the long-period analysis of the previous section. The short-period mechanisms were taken from work by Ryall and Ryall (1981a) and Cramer and Toppozada (1980). The combination of the University of Nevada's local array, CDMG's (California Division of Mines and Geology) local

stations and the USGS southern and central California arrays provides fairly dense coverage of the focal sphere for the larger events. The arrivals are fairly clean and impulsive even at P_n distances.

Figure 4-12 shows in detail the long-period solution for event B and the local short-period solution (the nodal planes for the long-period solution are superimposed on the short-period data). The largest discrepancy between the long and short-period polarities is in the northeast quadrant. Although the series of stations due south of the epicenter are also mismatched with the long-period mechanism, the travel path is along the axis of the Sierra Nevada and it is possible that the earth velocity model used to determine the take-off angles is inadequate. This would allow the first motion data points to move in or out on the focal sphere and therefore they are not grossly inconsistent. Also, note that the short-period mechanism also disagrees with this series of arrivals. Figure 4-13 summarizes the comparisons of short- and long-period mechanisms. Shown are the three events in the 1980 sequence and the Bishop earthquake. For events B, C and D, if the north-south plane is picked for the fault, then there are two main differences in the mechanisms: (1) the long-period mechanism is much more moderately dipping, and (2) it requires a significant component of dip-slip (normal) fault motion. In the case of the Bishop earthquake the inconsistency between the long and short-period mechanisms is in the northwest quadrant. If the east-west plane is chosen for the fault, then the only significant difference between mechanisms is the large dip-slip component at long periods. Figure 4-14 shows a comparison of the P_{ni} data for the Bishop earthquake with synthetics calculated for the long-period (solid nodal lines on the focal sphere) and short-period (dashed nodal line) fault mechanism. The oblique-slip mechanism fits better at all azimuths, especially in the northwest quadrant. COR, LON, and MSO

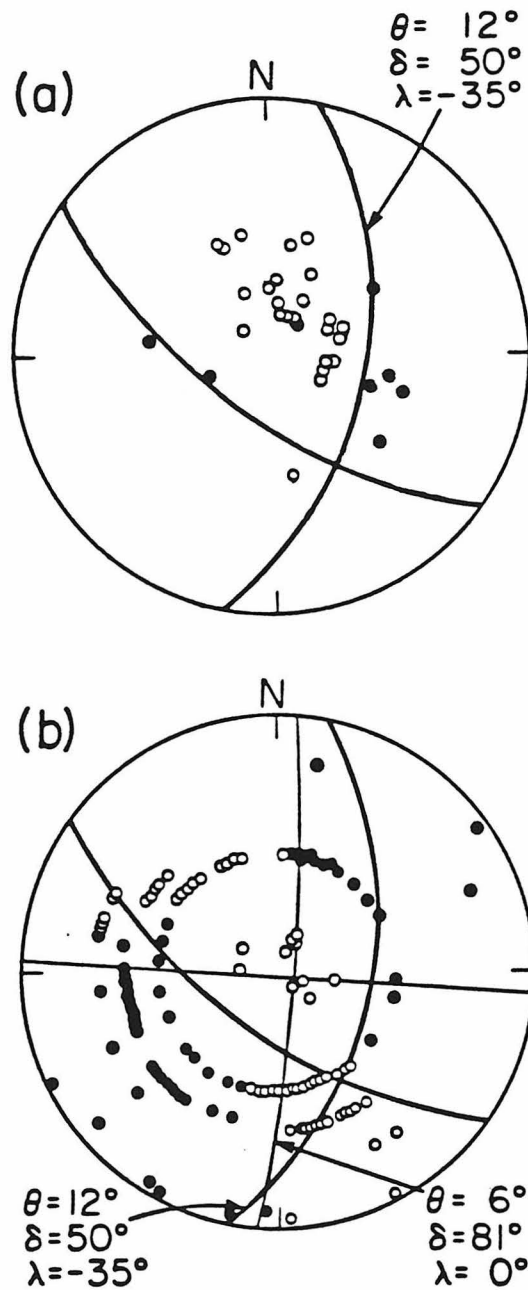


Figure 4-12: (a) Long-period teleseismic first motions and fault mechanism for event B. (b) Short-period first motion data (*Cramer and Topozada, 1980; Ryall and Ryall, 1981a; unpublished data from E. Corbett and R. Cockerham*). The strike-slip solution is from *Ryall and Ryall (1981a)*.

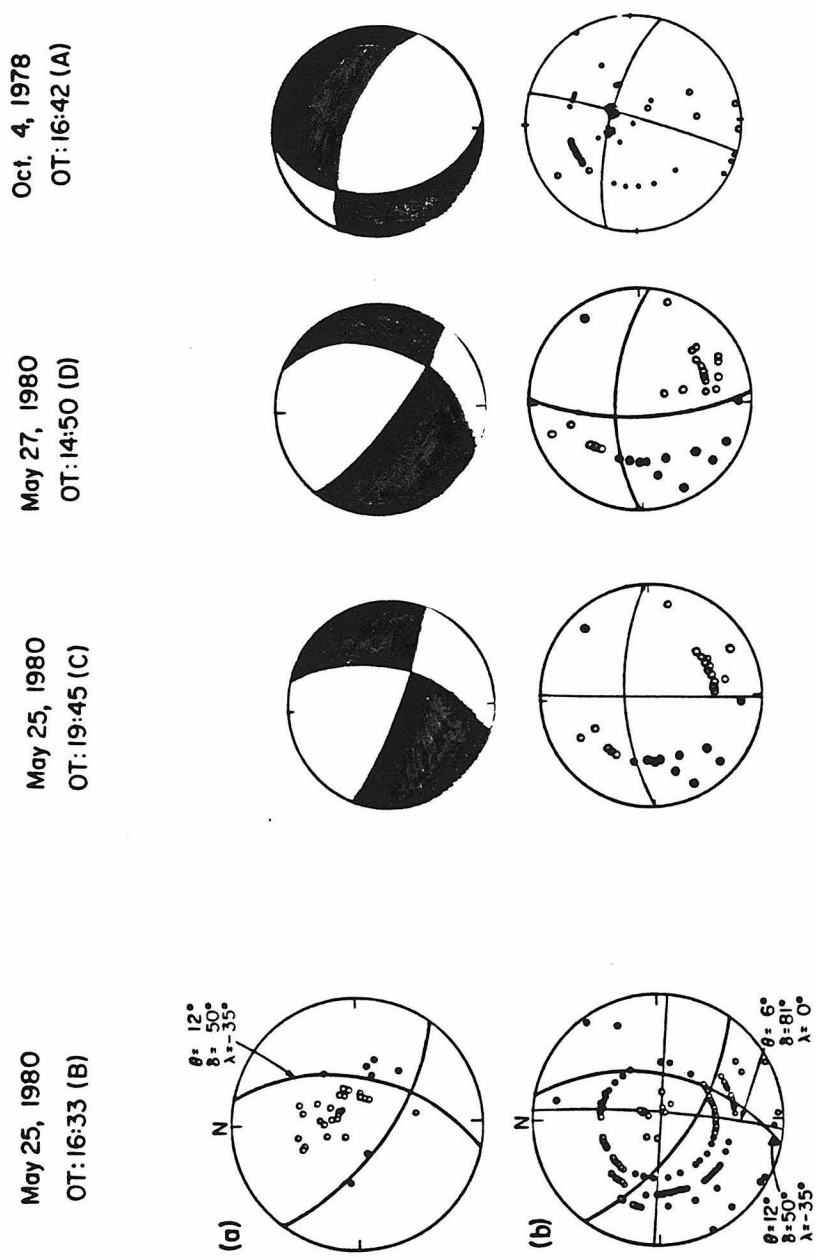


Figure 4-13: A comparison between the long-period mechanisms (top row) and short-period mechanisms.

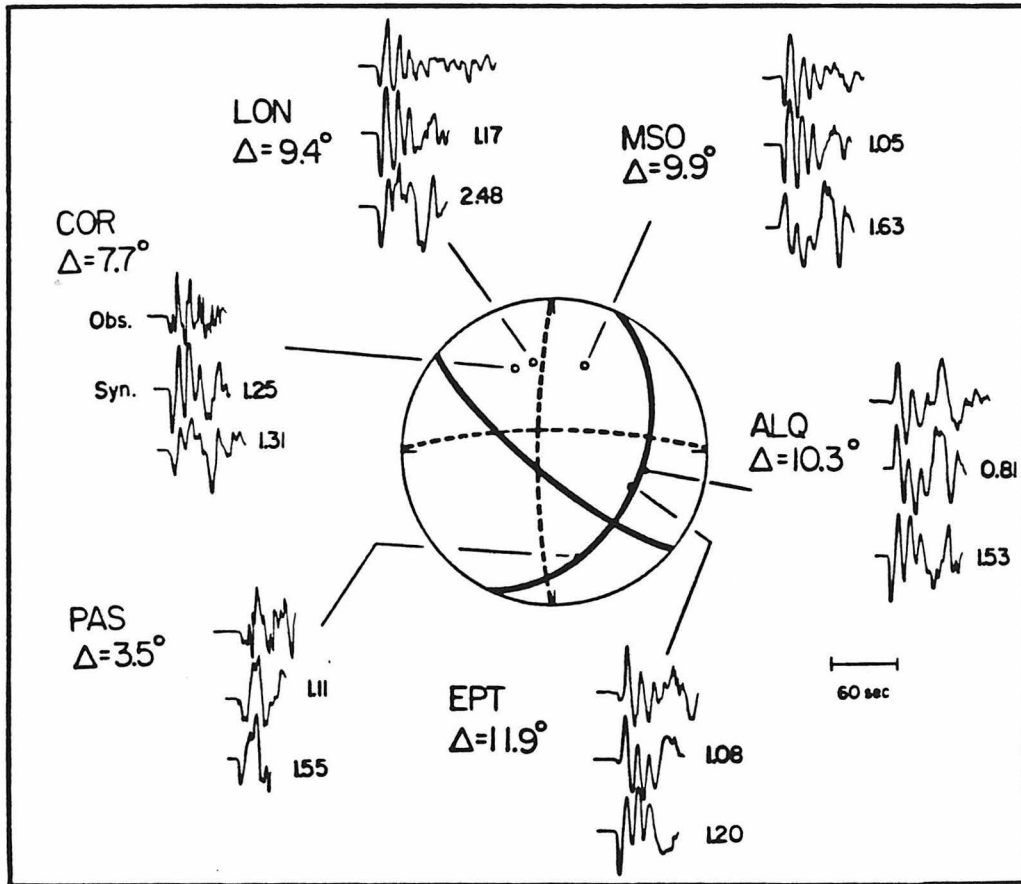


Figure 4-14: A comparison between observed (top trace at each station) waveforms for event A and synthetics calculated for the oblique-slip (middle trace) and strike-slip (bottom trace) models. The solid nodal lines give the oblique solution, while the dashed are for the strike-slip. The numbers to the right of each synthetic give the ratio of the moment determined at that station to the average moment.

would have the wrong polarity for the strike-slip model. The numbers to the right of each synthetic give the ratio of moment determined from that station to the average moment. The stability of this ratio can be used as a measure of the correctness of the fault mechanism. The order of magnitude larger scatter in the ratios for the strike-slip model compared to the oblique-slip model further supports the long-period mechanism.

Local short-period first motion solutions have not been published for the two aftershocks (events E and F). Although these events have substantially smaller moments (5 to 10 times smaller) than the main shocks, they also exhibit moderately dipping oblique faulting. This suggests that these aftershocks are the result of the same stress regime that caused the main shock sequence, and the discrepancy between long- and short-period fault mechanisms probably continues at least to these smaller moments. In Table 4-4 the P and T axes are also listed (in addition the T axes are shown in Figure 4-1). All the events in the Caldera area have very consistent stress-axes orientation. It is interesting to note that the T axes which would be determined from the short-period solutions are not grossly different from those in Table 4.4. On the other hand, the substantial plunge of the P axes is indicative of a dip-slip component of motion. The fact that the local short-period mechanism and the long-period fault mechanism is a phenomenon localized to the region around Long Valley.

4.4 DISCUSSION

Our interpretation of the faulting sequence associated with the 1980 Mammoth Lakes earthquakes is that each of the events occurred on planes which dip approximately 50° to the $S70^\circ E$ and involved varying amounts of lateral slip. The implication is that a system of en-echelon fault structures exists at depth. Evidence for the choice of the fault plane with the northeast strike is not compelling; it was chosen simply because it implied downfaulting along an approximately north-south structure which fit well with the gross geologic features in the area. Because of ground breakage on the Hilton Creek fault and the parallel trend of the epicenters, it is reasonable to propose that the earthquakes occurred on a zone of weakness associated with the frontal fault system. Direct association with the Hilton Creek fault is precluded by two observations. First, no fault plane compatible with the teleseismic data fits the trend of epicenters and the fault. The best line of evidence constraining the strike is the relative excitation of the Love and Rayleigh waves. Taken separately, each of the radiation patterns may fit a NNW fault with normal displacement, but unless a mechanism for anomalously large excitation of Love waves can be suggested, purely normal movement can be dismissed. Second, the hypocenters are located about 10 km west of the projected Hilton Creek fault plane at depth. Errors this large, although not impossible, are unlikely considering station coverage in the area.

The discrepancy between the long- and short-period fault-plane solutions is not easily explained away. There are two basic mechanisms that can cause the frequency dependence of the fault parameters; (1) distortion of the radiation pattern by structure and (2) complexity of the source. The simplest structural model would be to have deflection of short-period seismic signals due to a low velocity region

within the Caldera. *Steeple* and *Iyer* (1976) used teleseismic P-wave delays to map a volume beneath the Caldera in which the average P velocity is 15 percent lower than that of the surrounding crust. This low velocity zone extends in depth from approximately 5-25 km. *Hill* (1976) reported a series of late arrivals in a refraction experiment across Long Valley which he interpreted as a reflection from a depth of 7-8 km. This reflection could represent the roof of a magma body. There is evidence that the magma body is still an active feature. *Savage* and *Clark* (1982) present level line data which show a broad uplift centered over the resurgent dome in the western part of the Caldera. This uplift occurred sometime between 1975 and September 1980. *Ryall* and *Ryall* (1981b) observed S-wave screening for some of the aftershocks of the 1980 sequence which have travel paths through the Caldera. They interpret these observations to indicate a zone of partial melting at depths greater than 8 km. These different observations taken together strongly suggest that there may be a zone of substantially reduced velocity in the Caldera. *Sassa* (1936) observed the deflection of P waves up to 30° in azimuth for travel paths which crossed the Volcano Aso, Japan. The inconsistent first motions for the event B (see Figure 4-12, NE quadrant) correlate with travel paths across a segment of the Caldera; a low-velocity structure in this part of the Caldera would distort the radiation pattern in the observed manner. If we consider recording stations which are at Pn distance and that the low-velocity zone distorts both the azimuth and take-off angle, we can constrain the size of the velocity contrast which is required to produce the observed effect. It is simplest to assume that the low velocity zone has a deep root; then the velocity contrast must be on the order of 35 percent. For the Bishop earthquake, the travel paths are again across the same region of the Caldera and the velocity contrast which is required is approximately the same. Although a 35

percent velocity contrast is large (especially compared to *Stepples* and *Iyer's* 15 percent) this number is based purely on geometric deflection, and diffraction effects could reduce the necessary velocity contrast.

The data also suggest that source complexity may be a factor in the discrepancy between the short- and long-period mechanisms. This is demonstrated in Figure 4-15 which compares the long- and short-period waveforms for the same station for event B. For both records the first arrivals are well above the noise but show opposite polarity. The same phenomenon is observed at PNT ($\sim 14^\circ$) and FRB ($\sim 39^\circ$). These stations have azimuths which are approximately due north of the epicenters. Since the effect of deflection due to a near source velocity anomaly would have relatively little effect on teleseismic signals, these observations suggest complexity in the source-time function. Comparison of the arrival times between instruments indicates that the short-periods may arrive a fraction of a second earlier than the long-periods but this is probably not significant. The reversal of polarity is also observed for the first event in the 1980 sequence (event D) but it is not nearly as clear (the short-period arrival is much smaller).

For an arrival to show up clearly on the short-periods but be completely absent from the long-periods, a complicated time function would be required. The initial short-period waveform represents a very rapid rise time, or a small, high stress-drop event. The cleanness of the long-period dilational arrival puts a bound on the seismic moment of the small event; it is probably less than 1×10^{24} dyne-cm. The long-period waveforms are the response of the overall faulting episode. In other words, the short-period event may represent failure of an asperity (strong patch on the fault) which, when broken, allows the regional strain to be relieved with the mechanism determined from the long-period data.

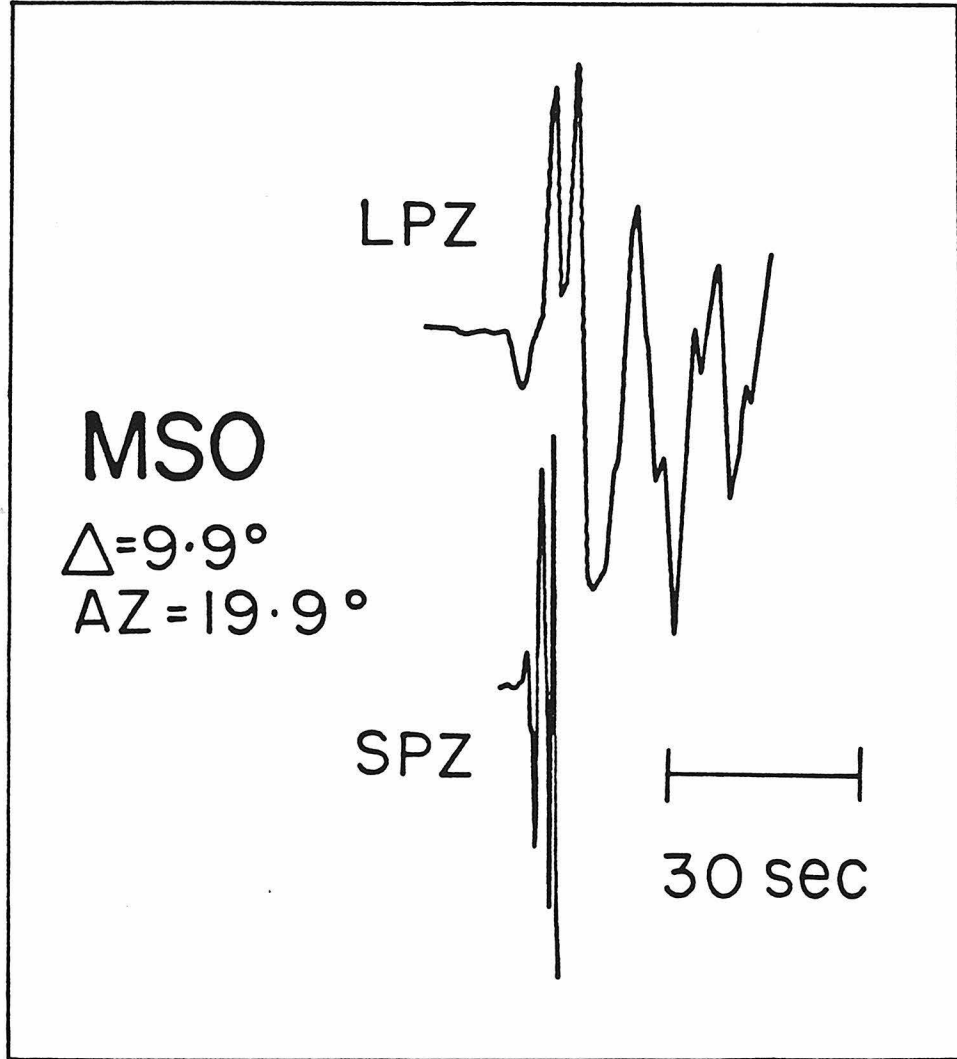


Figure 4-15: A comparison of the long- and short-period P arrivals at MSO for event B.

Although this type of source complexity seems plausible for a single event, it would be difficult to explain the frequency dependence of all the events with the same process. Obviously, the difference in polarity at teleseismic distances requires the short-period event to have a different faulting mechanism. Whether this fault mechanism is the vertical strike-slip fault as indicated by the local short-period mechanism depends on the effect of the local structure on these fault plane solutions as discussed previously. If one chooses to minimize the distortion due to structure and suggests that the short-period mechanism represents the breaking of a small asperity then the repeatability of the process must be explained. *Savage* and *Clarke* (1982) have shown that magma injection beneath the resurgent dome (at the western end of Long Valley) would give rise to a stress system which has a maximum shear-stress on north-south planes, consistent with left-lateral strike-slip faulting in the vicinity of the hypocenters. The stress drops that would be expected for *Savage* and *Clarke's* point source magma injection are small; a few bars at most. A similar left-lateral shear on north-south planes would be imposed in the hypocentral region of the Bishop earthquake although the stress drop would be substantially lower. It is possible to develop a model in which a superposition of the stress field from the magma inflation on the regional stress system allows the possibility of a very sharp, but low seismic moment strike-slip beginning followed by a large scale fault movement along a moderately dipping zone of weakness. Although this is a very complicated model (and for that reason unappealing), it can account for the source mechanism discrepancy, and would suggest a difference between the small and large earthquakes. A less speculative hypothesis would be to suggest that the stress system in this region has small scale heterogeneity and thus the short-period source time functions are complicated. The stress heterogeneity and process of magma

implication could be related causally, although probably not in a systematic fashion.

Of all the aftershocks of the 1980 sequence with $M_L > 4.0$ not a single one has been located in the Caldera itself. Since the hypocentral depths are as great as 15 km this suggests that the Caldera cannot support stress. If there is a magma body present it might be possible to detect it by some subtle differences between the observed P_{nl} and the synthetics. Figure 4-16 shows a cartoon depicting how these differences might arise. If the body is well defined it might affect upgoing or downgoing rays preferentially. Similarly, if the magma body is a honeycomb, the P waves will be more affected than the S waves, or conversely, if it is a mush, the S waves will show preferential attenuation. Figure 4-17 and 4-18 show the observed P_{nl} and fit of the synthetics for events A and D. Also shown are the azimuths to the receiver. In either case, there is not an obvious difference in the quality of fit for those stations which had travel paths through the Caldera and those which did not. COR is probably fit the poorest for event D; let's assume that this is due to the influence of the magma body. We can try to improve the quality of fit by attenuating different groups of rays. Figure 4-19 summarizes this analysis. t^* operators were applied to rays which left the source as P or S waves. The arrows on the β 's and α 's in Figure 4-19 denote whether they were upgoing or downgoing. Shown to the right of each synthetic is a number which gives the ratio of the moment determined for the non-attenuated to attenuated synthetic (a measure of the change in absolute amplitude). The case in which the fit improved the most was where all S waves had a $t^* = 0.2$ seconds. In any case, this can hardly be cited as evidence for anomalous structure. The negative result of this experiment does not exclude a magma body, but it probably limits its size to a fraction of the caldera width.

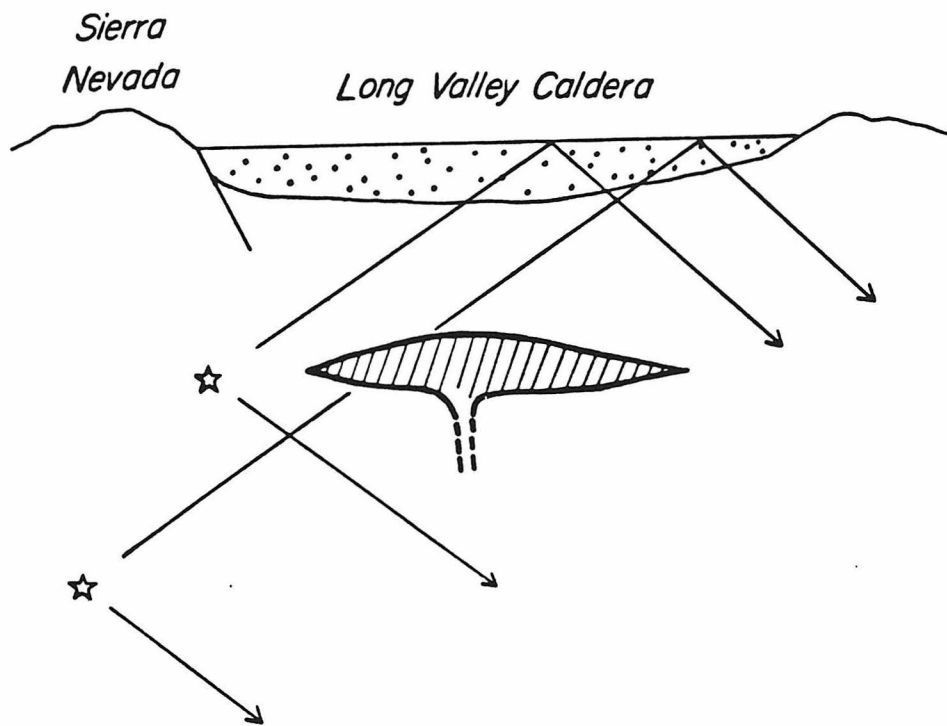


Figure 4-16: Diagram showing how different groups of rays could be affected by a magma body in Long Valley.

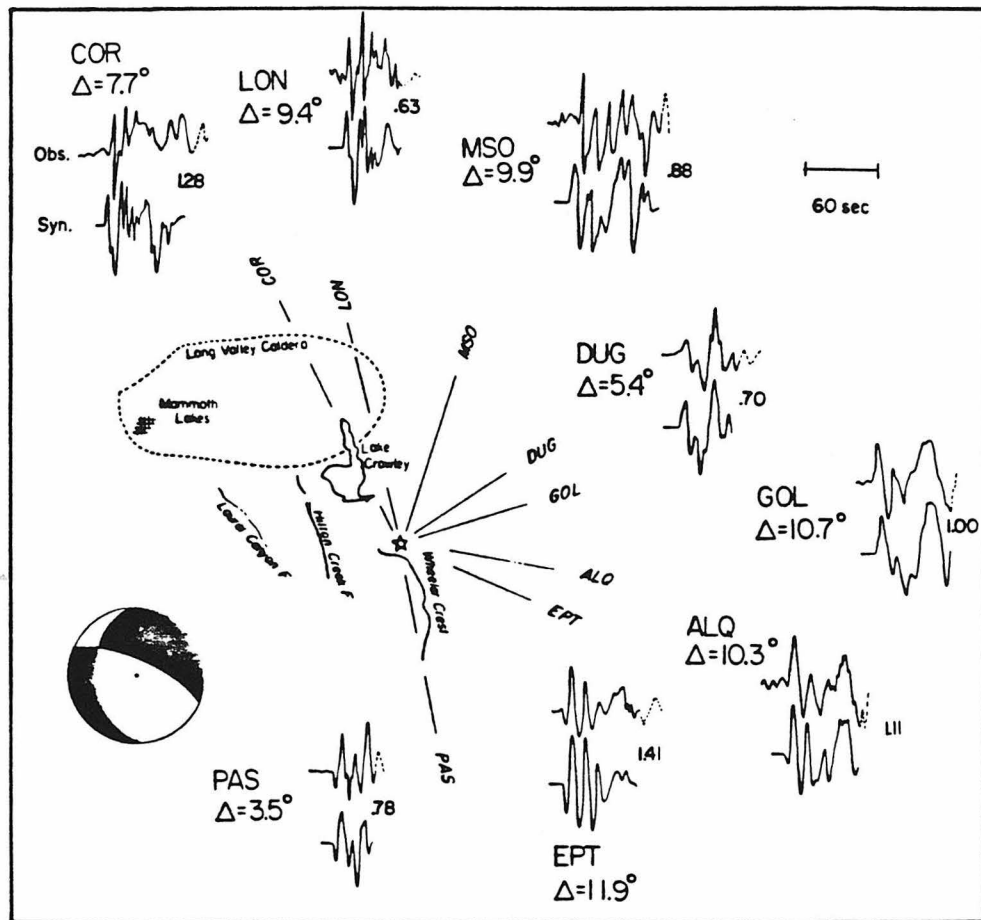


Figure 4-17: Waveforms and travel paths used for event A. The model for the synthetics is given in Table 4-4.

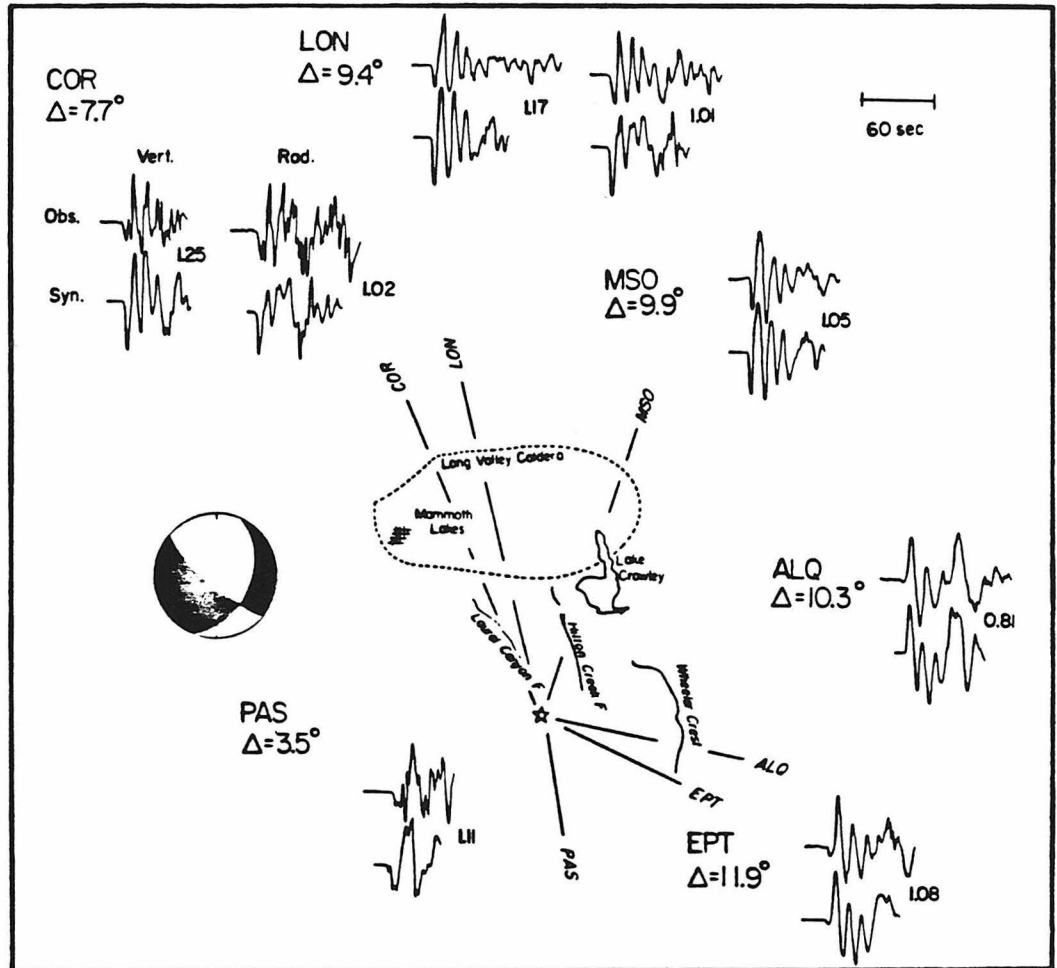



Figure 4-18: Waveforms and travel paths for event D. The model used for the synthetics is given in Table 4-4.

COR
 $\Delta = 7.7^\circ$
 AZ = 335°



60 sec

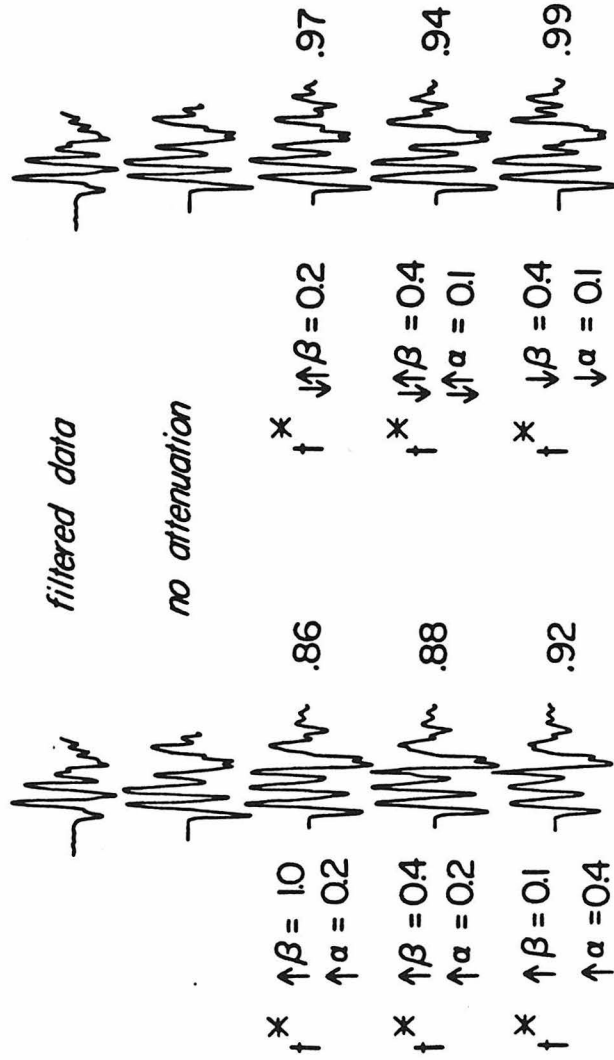


Figure 4-19: The effect of attenuating different groups of rays on the fit of the synthetics to the P_{nI} waveform at COR for event D. The arrows indicate which direction the rays leave the source.

4.5 CONCLUSIONS

Recent earthquakes near the Long Valley Caldera display a significant discrepancy between the long- and short-period faulting mechanism. The short-period first-motion solutions of the large events require vertical strike-slip faulting, while invariably the long-periods require oblique-slip on more moderately dipping faults. At this time it is not possible to isolate the cause of the fault mechanism discrepancy although it is apparent that the source-time functions are complex. The fact that this discrepancy has occurred over a period of time (since the 1978 Bishop earthquake) suggests that at least part of the discrepancy may be related to structure. Local short-period arrivals which travel through portions of the Caldera north of the epicenters could be systematically deflected. Both a low-velocity zone and stress heterogeneity are consistent with other evidence for the recent injection of magma. In such a region as Long Valley, great care must be taken when interpreting short-period fault mechanisms in terms of tectonic significance. The T-axes which are determined from the short-period mechanisms are consistent with those of the long-period mechanisms (both are roughly consistent with the regional stress field).

REFERENCES

- Bailey, R.A., G.B. Dalrymple, and M.A. Lanphere (1976). Volcanism, structure and geochronology of Long Valley Caldera, Mono County, California, *J. Geophys. Res.*, 81, 725-744.
- Clark, M.M. and J.C. Yount (1981). Surface faulting along the Hilton Creek fault associated with the Mammoth Lakes, California, earthquakes of May 1980 (abstract), *Earthquake Notes*, 52, 45.
- Cramer, C.H. and T.R. Topozada (1980). A seismological study of the May 1980 and earlier earthquake activity near Mammoth Lakes, California, Special Report No. 150, California Division of Mines and Geology, R.W. Sherbourne, ed., 91-130.
- Given, J.W., T.C. Wallace and H. Kanamori (1982). Teleseismic analysis of the 1980 Mammoth Lakes earthquake sequence, *Bull. seismo. Soc. Am.*, 72, 1093-1110.
- Helmberger, D.V. (1974). Generalized ray theory for shear dislocations, *Bull. seismo. Soc. Am.*, 64, 45-64.
- Helmberger, D.V. and S.D. Malone (1975). Modeling local earthquakes as shear dislocations in a layered halfspace, *J. Geophys. Res.*, 80, 4881-4888.
- Hill, D. (1976). Structure of Long Valley Caldera, California from a seismic refraction experiment, *J. Geophys. Res.*, 81, 745-753.
- Langston, C.A. and D.V. Helmberger (1975). A procedure for modeling shallow dislocations, *Geophys. J.*, 42, 117-130.
- Kanamori, H. and J.W. Given (1981). Use of long period surface waves for fast determination of earthquake source parameters, *Phys. Earth Planet. Inter.*, 27, 8-31.

- McNally, K.C. (1981). Geophysical anomalies in California: a return to normal seismicity (submitted for publication).
- Ryall, A. and F. Ryall (1981a). Spatial-Temporal variations in seismicity preceding the May 1980, Mammoth Lakes California, earthquakes, *Bull. seismo. Soc. Am.*, 71, 747-760.
- Ryall F. and A. Ryall (1981b). Attenuation of P and S waves in a magma chamber in Long Valley Caldera, California, *Geophys. Res. Let.*, 8, 557-560.
- Sassa, K. (1936). Anomalous deflection of seismic rays in volcanic districts, *Memoirs of the College of Science, Kyoto Imperial University, Series A*, vol. XIX, no. 2.
- Savage, J. and M. Clark (1982). Magmatic resurgence in Long Valley Caldera, California: possible cause of the 1980 Mammoth Lakes earthquakes, submitted to *Science*.
- Steeple, D. and H. Iyer (1976). Low-velocity zone under Long Valley as determined from teleseismic events, *J. Geophys. Res.*, 81, 849-860.
- Taylor, G.C. and W.A. Bryant (1980). Surface rupture associated with the Mammoth Lakes earthquakes of May 25 and 27, 1980, Special Report, No. 150, California Division of Mines and Geology, R.W. Sherbourne, Ed. 91-130.

Chapter V: Evidence of Tectonic Release From Underground Explosions in Long-Period P Waves

5.1 INTRODUCTION

It is well documented that certain underground nuclear explosions require sources which have substantial non-isotropic components (*Press and Archambeau, 1962; Toksoz, Ben-Menahem and Harkrider, 1964; Toksoz and Kehrner, 1971; among others*). The surface-wave observations provide the evidence which is most commonly cited for this source asymmetry. For example, for the explosion GREELEY, the observed ratio of the Love to Rayleigh wave excitation is much larger than would be predicted for a pure explosion source and scattering in a simple layered earth. In addition, the Rayleigh waves display a radiation pattern (*Toksoz and Kehrner, 1972*). In the case of the Shagan river region of the Eastern Kazakh Test site, explosions which are only kilometers apart produce Rayleigh waves which are 180° out of phase (*North and Fitch, 1981; Goforth 1982*). As for body waves, SH waves at teleseismic distances are a fairly common observation (*Nuttli, 1969*). Similarly, in the near field, there are tangential accelerograms which are much too large to be explained by simple scattering (*Aki et al., 1969*).

A widely accepted explanation for the phenomenon of SH-type seismic wave generation by explosions is the release of tectonic strain. Considering the abundance of examples for the influence of tectonic release on SH and surface waves, it is somewhat surprising that there is very little documentation of its influence on P

waves. *Johnson et al.* (1982) have shown that moment tensor inversion of three-component, strong-motion data (the data encompasses both P and S waves) can be interpreted in terms of an explosion plus a double couple, although the effect of the tectonic release on the P waves is not obvious. No one has presented a set of teleseismic short-period P waves which are clearly distorted by tectonic release. One of the more widely accepted explanations for the lack of an obvious tectonic release signature on short-period P-waves is that tectonic release is a low stress-drop phenomenon (*Bache*, 1976). In the case of NTS, the low stress-drop would conspire with the strike-slip radiation pattern (which does not radiate P-waves efficiently to teleseismic distances) predicted for the tectonic release from the surface waves to make the short-period signature very difficult to observe in the far-field body waves. In this paper we present a suite of long-period P waveform distortions which we have modeled as tectonic release. An unexpected result of our modeling analysis is that if the tectonic release is interpreted in terms of a triggered earthquake, very high stress drops are required. This apparent inconsistency with the short-period data may help resolve the mechanism of tectonic release.

The data set which we use is the long-period WWSSN recordings at regional and upper-mantle distances from megaton explosions at Pahute Mesa. At regional distances (less than 12°), the long-period body waves are essentially crustal reverberations and very little diving ray energy is present. Fairly complete azimuthal station coverage at regional distances allows the determination of a radiation pattern and moment for the double couple. Beyond regional distances the dominant body-wave arrivals are diving rays (rays bottoming below the Moho) and the phase sP can be identified and used to determine source depth and duration. The purpose of this report is to qualify the effects of tectonic release for these large explosions with

this data set.

5.2 COMPARISON OF EXPLOSIONS AND EARTHQUAKES

The set of observations that first lead us to suggest that there is a tectonic release signature on the long-period P waves is the striking similarity between the seismograms of certain NTS events and shallow, moderate-size earthquakes. Fortunately, long-period seismograms for earthquakes of this size are fairly well understood at regional through teleseismic distances. The use of synthetic seismograms allows the separation of the travel path and source effects and it is possible to identify the various phases such as P, pP and sP. A comparison of the well understood earthquake waveforms and those of an explosion can be used to isolate S-wave energy in the source. An earthquake of particular importance to this study occurred in eastern Nevada ($m_b = 5.6$, ISC) on August 16, 1966. The proximity of this event to NTS (≈ 200 km due east) allows us to calibrate the travel paths. In addition, the fault orientation is roughly consistent with that predicted for the tectonic release at NTS. Appendix V-1 gives the detailed analysis of the regional waveforms for the source parameters of this earthquake.

Figure 5-1 shows a comparison of the tangential records for the Nevada earthquake and the nuclear explosion GREELEY (12/20/66). The stations shown here (YKC, CMC and MBC) have source-station separations which are almost identical for the explosion and the earthquake. These stations are also very close to being naturally rotated, which makes it possible to compare the SH and Love waves for both sources directly on the E-W component. In Figure 5-1 the records are aligned on the SH arrival. Although the record from GREELEY is noisier, the coherence between the explosion and earthquake is remarkable. The earthquake depth is on the order of 6

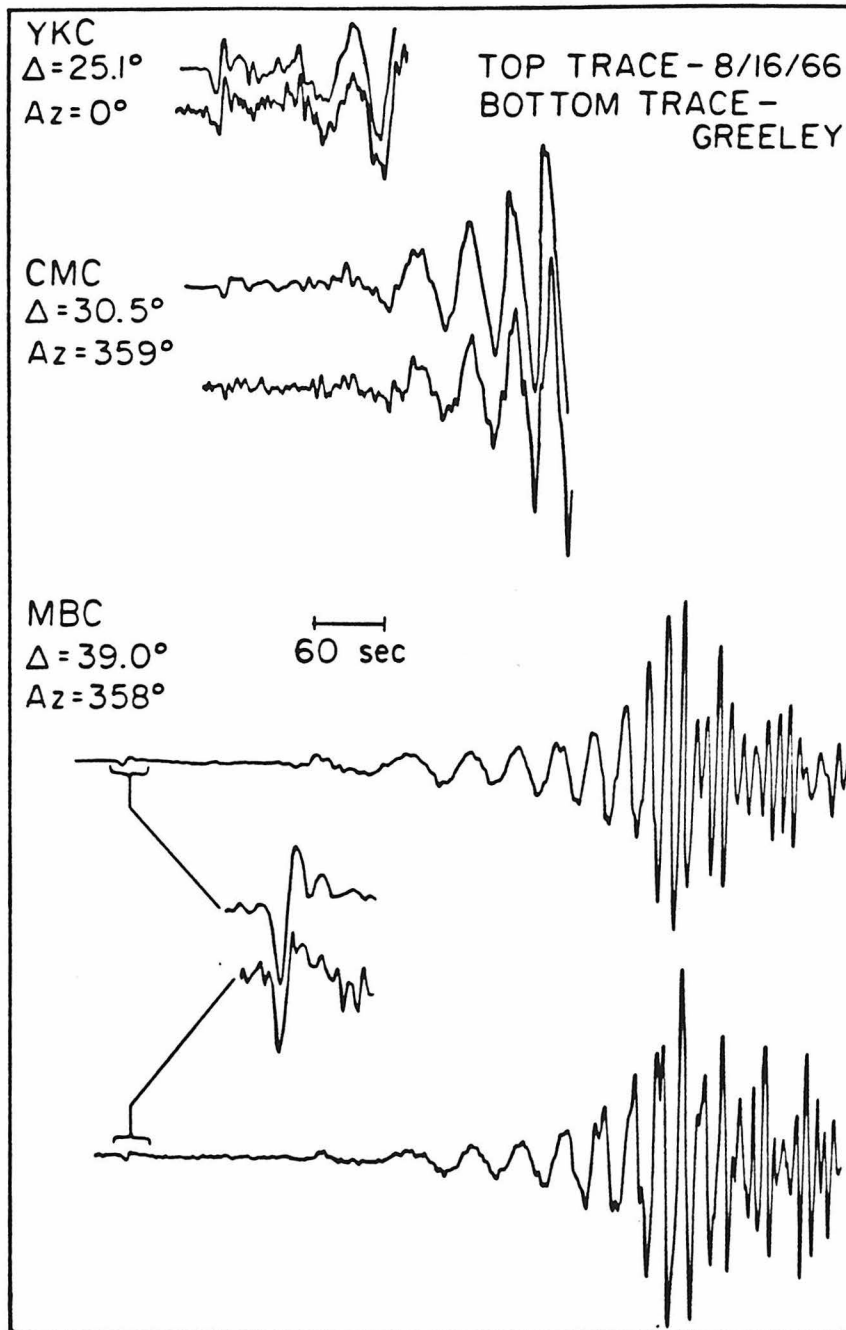


Figure 5-1: A comparison between the SH and Love waves for the nuclear explosion Greeley (12-20-66) and an earthquake in eastern Nevada (8-16-66). The stations are naturally rotated. The seismograms are lined up on the S arrival and the amplitude scale is the same for both the earthquake and explosion. The time scale of the enlarged SH wave is one half that of the other traces.

km (see Appendix V-1) while the explosion detonation was at 1.2 km depth. Considering this difference in depth, the coherence of the surface waves is also quite good. The SH pulses at MBC have been enlarged and very nearly overlay. The similarity between these seismograms suggests that the time function and mechanism associated with the GREELEY tectonic release must be similar to that of the earthquake. This leads us to believe that the long-period P waves from the GREELEY tectonic release should be visible wherever the earthquake's P waves are apparent. On the basis of the comparison in Figure 5-1, it is possible to place a lower bound on the moment for the tectonic release of 4.5×10^{24} dyne-cm. This lower bound is based on the fact that the northern azimuth is in a similar part of the SH radiation pattern for both the earthquake and tectonic-release orientations, within 20° of the maximum.

Another earthquake which provides an interesting comparison with Pahute Mesa explosions occurred in Northern Baja on December 22, 1964. The earthquake has a strike-slip orientation (see Appendix V-1 for the detailed source parameters) such that ALQ and LUB are near the positive P-wave radiation lobe. The tectonic-release orientation predicted for NTS on the basis of surface waves (right lateral strike-slip) also puts these two stations in the positive lobe. A comparison of the waveforms for the Baja earthquake and BOXCAR is shown in Figure 5-2. At the regional distance of ALQ, the waveform is essentially crustal reverberations. There is very little mantle ray energy present because the distance range is in the shadow of a low-velocity zone. At the slightly larger distance range represented by the LUB records, the shadow zone has been passed and diving rays play an important role in the waveform.

A comparison of the explosion and earthquake records at ALQ shows that they are similar. The PL from BOXCAR has a higher frequency content than that from the

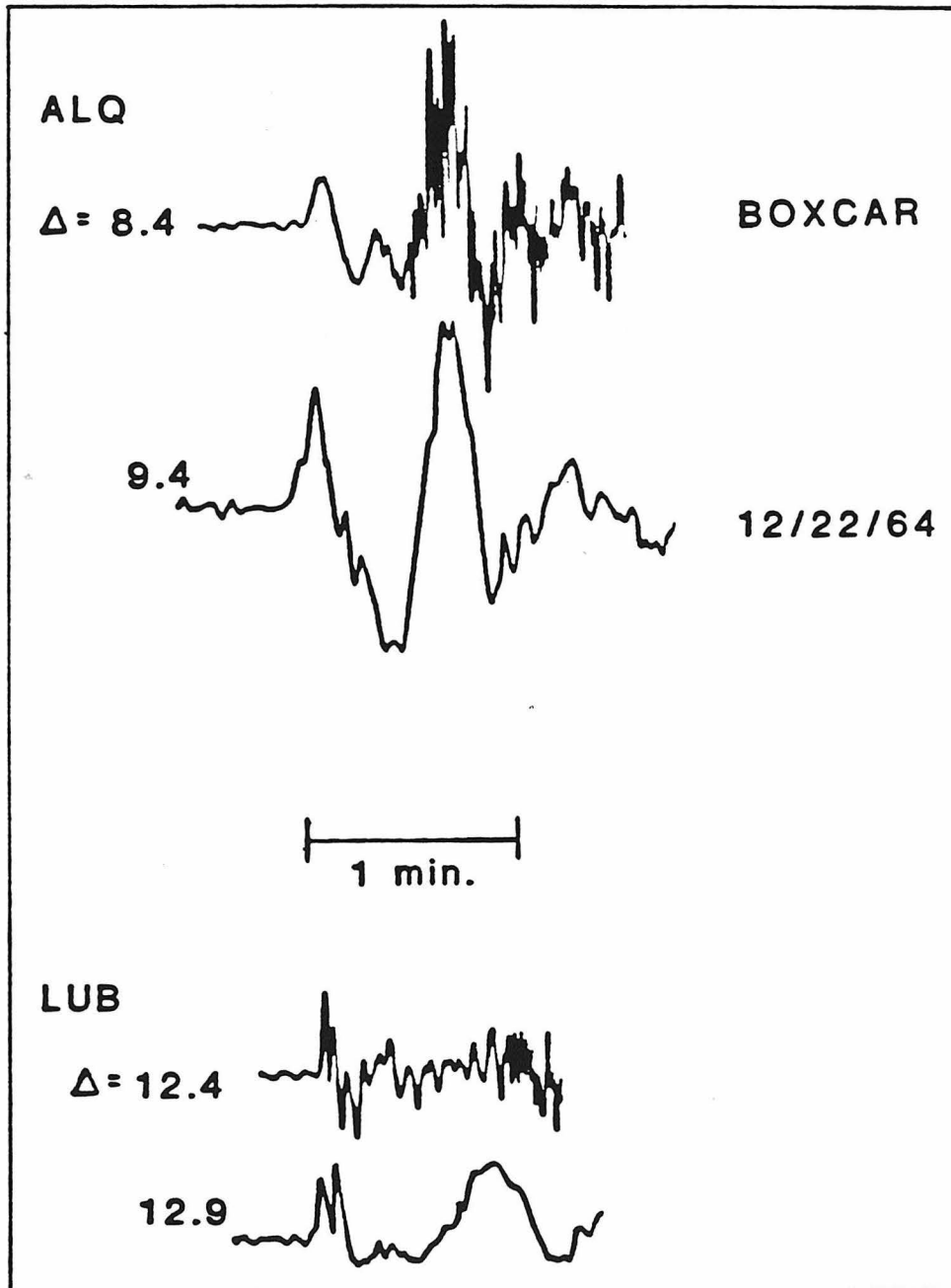


Figure 5-2: A comparison between the regional body waves of the nuclear explosion BOXCAR (top trace for both stations) and the San Miguel earthquake (12-22-64). The seismograms are the vertical components.

Baja event as would be expected from the higher frequency of the time function of the explosion. Although the larger distance for the earthquake makes the waveform slightly more dispersed, the long-period content is fairly coherent. At LUB, the PL on the earthquake record is again longer period than that of the explosion. In the beginning part of the record there is a clear separation of arrivals. For the earthquake we can model the second arrival as sP. Note that there is a similar separation of arrivals for BOXCAR, which is suggestive of a similar phenomenon. The more shallow depth of the explosion (1.2 km compared to 8 km) can explain the less dramatic separation, but it appears that there is significant S-wave energy present in the explosion time function.

Figure 5-3 shows a profile of synthetic seismograms for a strike-slip fault. The earth model which was used is a single layer crust over the T7 (*Burdick and Helmberger, 1978*) mantle. The ALQ seismogram for the Baja event corresponds to the record at 900 km while the LUB seismogram corresponds to the record at 1300 km. Our ability to predict the earthquake waveforms assures that we are correctly identifying sP. In the synthetic profile the effect of the low-velocity zone is fairly obvious; the seismogram at 800 km is clearly in the shadow while 1000 km is out of the shadow.

5.3 ANALYSIS

The megaton explosions at Pahute Mesa provide a good data set for a systematic analysis of tectonic release. The large size of the events produced usable long-period P waves out to 30°. Figure 5-4 is a base map of Pahute Mesa showing the location of some of the larger explosions. The outline of the Silent Valley Caldera, which is an important geological feature on Pahute Mesa, is also shown. The

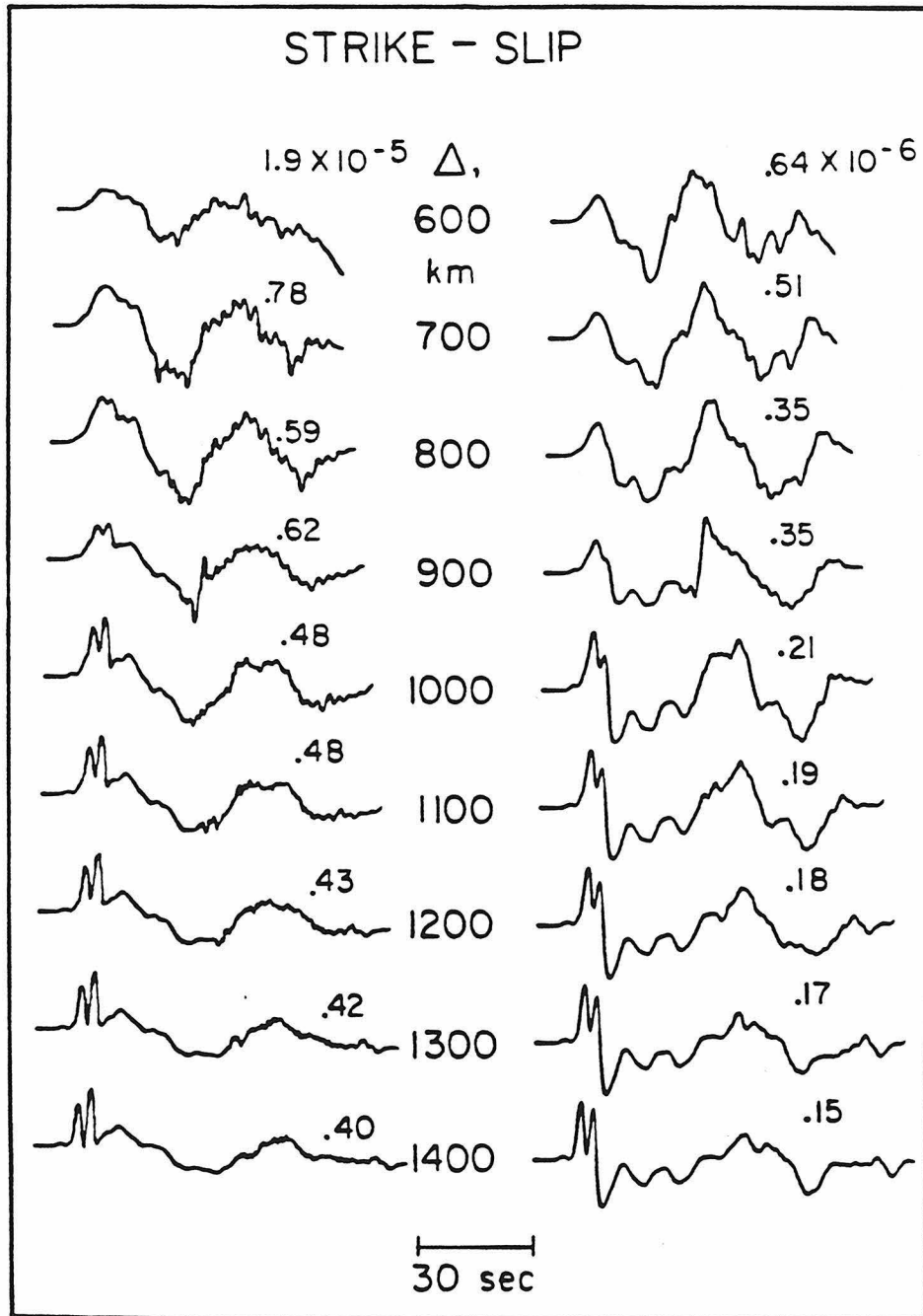


Figure 5-3: Profiles of synthetic strike-slip responses without instrument (left) and with a WWSSN long-period instrument (right) computed for a crustal layer over the T7 mantle. The distances before 900 km are in the shadow of the low velocity zone, while beyond a 1000 km strong diving ray energy is present. The clear separation of arrivals beyond 1000 km is due to sP and P.

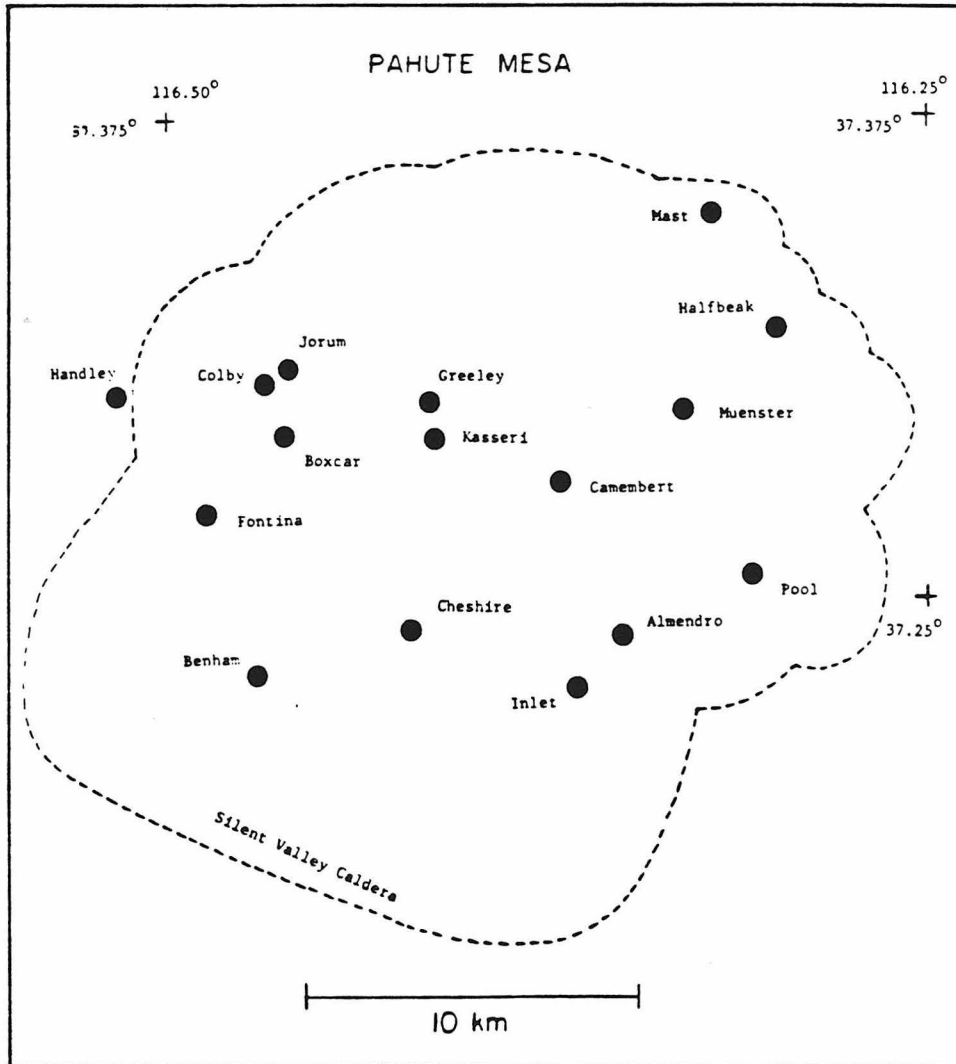


Figure 5-4: A base map of the Pahute Mesa test site and the location of some of the larger explosions.

explosions in the western half of the caldera are the most important for this study. The sizes and depths of burial for these events are comparable (see Table 5.1) which allows us to assume that the explosion time function is constant. The close spatial relationship of the detonations suggests that the near-source structure is also similar for all the events (at least in the long-period pass band). Therefore, we can interpret differences in the waveforms for several explosions in terms of tectonic release. It is particularly interesting to compare events which are very close in space but separated in time such as GREELEY and KASSERI or BOXCAR and COLBY.

Upper-Mantle Records: Ideally, at upper-mantle distances the waveforms from explosions should simply be the product of the interaction of the source time function, the rays P and pP and the earth structure. The addition of a component of tectonic release adds another time function convolved with the set of rays P, pP and sP. If the NTS tectonic release has the strike-slip mechanism as indicated by the surface waves, then the most important phase at upper mantle distances should be sP. Figure 5-5 shows the long-period vertical seismograms for eight of the Pahute shots at the WWSSN station SHA ($\approx 24^\circ$). All the records are plotted on the same amplitude scale. The records have been ordered according to the importance of the second upswing relative to the first upswing. About 4 1/2 minutes after the P wave is a long-period arrival whose timing corresponds to the travel time of SV. There is a strong correlation between the ratio of the second and first upswings in the P-wave signal and the size of SV (compare the first swing, or a-b P amplitudes to the SV amplitudes). This strongly suggests that the second upswing in the P wave train is controlled by an S wave, namely sP. Given this interpretation, the records in Figure 5-5 are ordered from least to most tectonic release. Note that KASSERI has a much smaller tectonic release than GREELEY which was detonated nine years earlier.

TABLE 5-1
Large Pahute Mesa Explosions

Name	Date	OT	Lat(N)	Long(W)	Depth	Est Yield (kt)
Greeley	12-20-66	15:30	37.30	116.41	1215	830
Boxcar	04-26-68	15:00	37.29	116.46	1158	1000
Benham	12-19-68	16:30	37.23	116.47	1402	1000
Jorum	09-16-69	14:30	37.31	116.46	1158	700
Handley	03-26-70	19:00	37.30	116.53	1206	1900
Almendro	06-06-73	13:00	37.24	116.35	1064	570
Mast	06-19-75	13:00	37.35	116.32	912	520
Camembert	06-26-75	12:30	37.28	116.37	1311	750
Kasseri	10-28-75	14:30	37.29	116.41	1265	1200
Inlet	11-20-75	15:00	37.22	116.37	817	500
Muenster	01-03-76	19:15	37.30	116.33	1451	600
Fontina	02-12-76	14:45	37.27	116.49	1219	900
Colby	03-14-76	12:30	37.31	116.47	1273	900
Pool	03-17-76	14:15	37.26	116.31	879	500

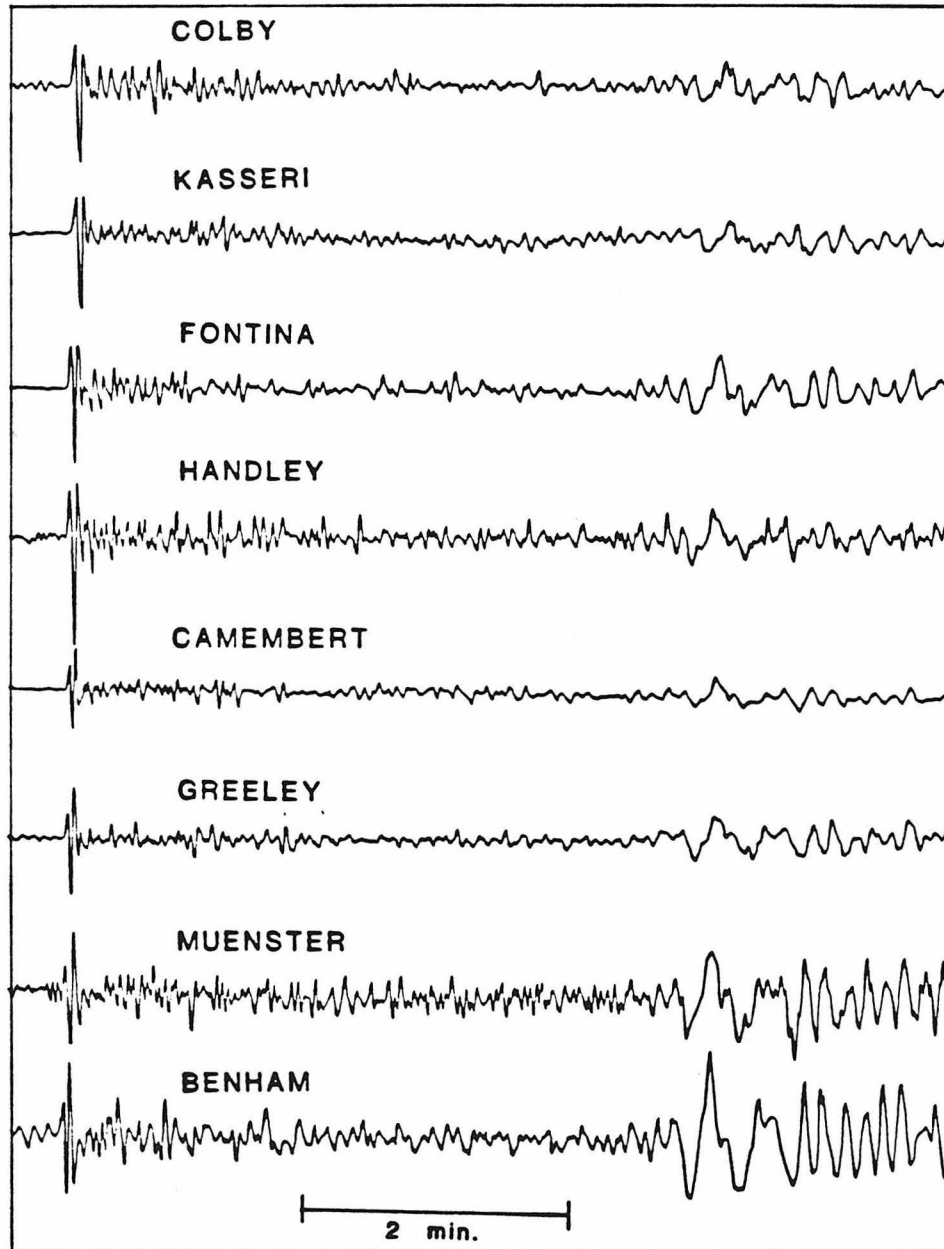


Figure 5-5: The vertical component records for 8 large Pahute Mesa explosions at the WWSSN station SHA. These are long-period seismograms which are arranged according to the importance of the second upswing in the P wave. About 4 1/2 minutes after the P arrival is the SV wave.

On the basis of the SHA comparison, BENHAM would be assigned the largest tectonic release. On the other hand, *Toksoz and Kehler* (1972) assign an F factor of 1.6 for GREELEY compared to 0.85 for BENHAM. The F factor is the relative strength of the double-couple (tectonic release) and explosion as determined by the ratio of the Love-wave to Rayleigh-wave amplitude. The difference between our assessment of the importance of tectonic release and that determined by the F factors is that *Toksoz and Kehler* assume a pure strike-slip mechanism for the tectonic release. In the case of BENHAM, preliminary modeling of the SV pulse suggests that there is a small, but detectable (15-20 per cent), component of dip-slip motion. This also agrees with observations of surface faulting (*Bucknam, 1969; Hamilton and Healy, 1969*). Even a ratio of 1-to-5 for dip-slip to strike-slip motion is important since the dip-slip motion is much more efficiently radiated to teleseismic distances.

The differences in the P waveforms, such as were discussed for SHA in Figure 5-5, are the types of waveform distortions we qualitatively model as tectonic release at upper-mantle distances. There is a well aligned profile of stations in the southern United States which simplifies the analysis. The stations LUB, JCT, DAL, OXF, and SHA only vary by about 10° in azimuth from NTS. This constant azimuth means that the effects of radiation pattern can be neglected. Also, this station profile is very close to the radiation lobe of sP as predicted by the surface-wave orientation for the double couple. The type of analysis we do is to compare the waveform of a low tectonic-release event with one which is high. Figure 5.6 is an example of this process. Shown are the COLBY and BOXCAR records at LUB ($\Delta = 12.4^\circ$). The main difference in waveform for these events is the second upswing. The latter part of the records are quite similar. This similarity suggests that one could simply add a component of tectonic release to the COLBY record and simulate the BOXCAR record.

Shown below the BOXCAR record in Figure 5.6 is such a simulation. In this case the tectonic-release synthetic has a strike-slip orientation where the earth model used is a single layer crust over the upper-mantle T7. This synthetic includes the large number of rays for the crustal waveguide (the P_{nl} response) plus the diving rays in the upper mantle. There is a one-second time delay between the double-couple component and the explosion, although the S-velocity of the source region is larger (3.5 km/sec) than would be expected for a shallow source (the crust is modeled as a single layer). There is a tradeoff between the relative timing of the explosion and double-couple and the S-velocity, but this aside, the prediction of the BOXCAR waveform is quite remarkable. Peak for peak, the prediction and observation of BOXCAR correspond back into the PL arrivals. The time function for the synthetic has a 0.6 second duration. The moment that is required for this fit is 5×10^{24} dyne-cm. This is a minimum estimate for a pure strike-slip orientation. Although there is very little seismic evidence for much dip-slip component in the BOXCAR tectonic release, a small component of dip-slip motion could lower the overall moment to 4.0×10^{24} dyne-cm (any larger component of dip-slip motion degrades the synthetic fit at LUB). Although there is not much resolution on the depth of the tectonic double couple, which may have some effect on the time function duration, even the least favorable case of the ratio of source duration to moment implies a high stress-drop (hundreds of bars) if the tectonic release is triggered fault motion.

The best example of this type of comparison analysis is for GREELEY and KASSERI. In this case there are four stations in the southern profile which are available for comparison. Figure 5-7 shows the records at LUB, JCT, DAL and SHA. The records are very similar for the two events with the exception of the very strong second upswing on all the GREELEY records. The similarity of waveforms allows us to

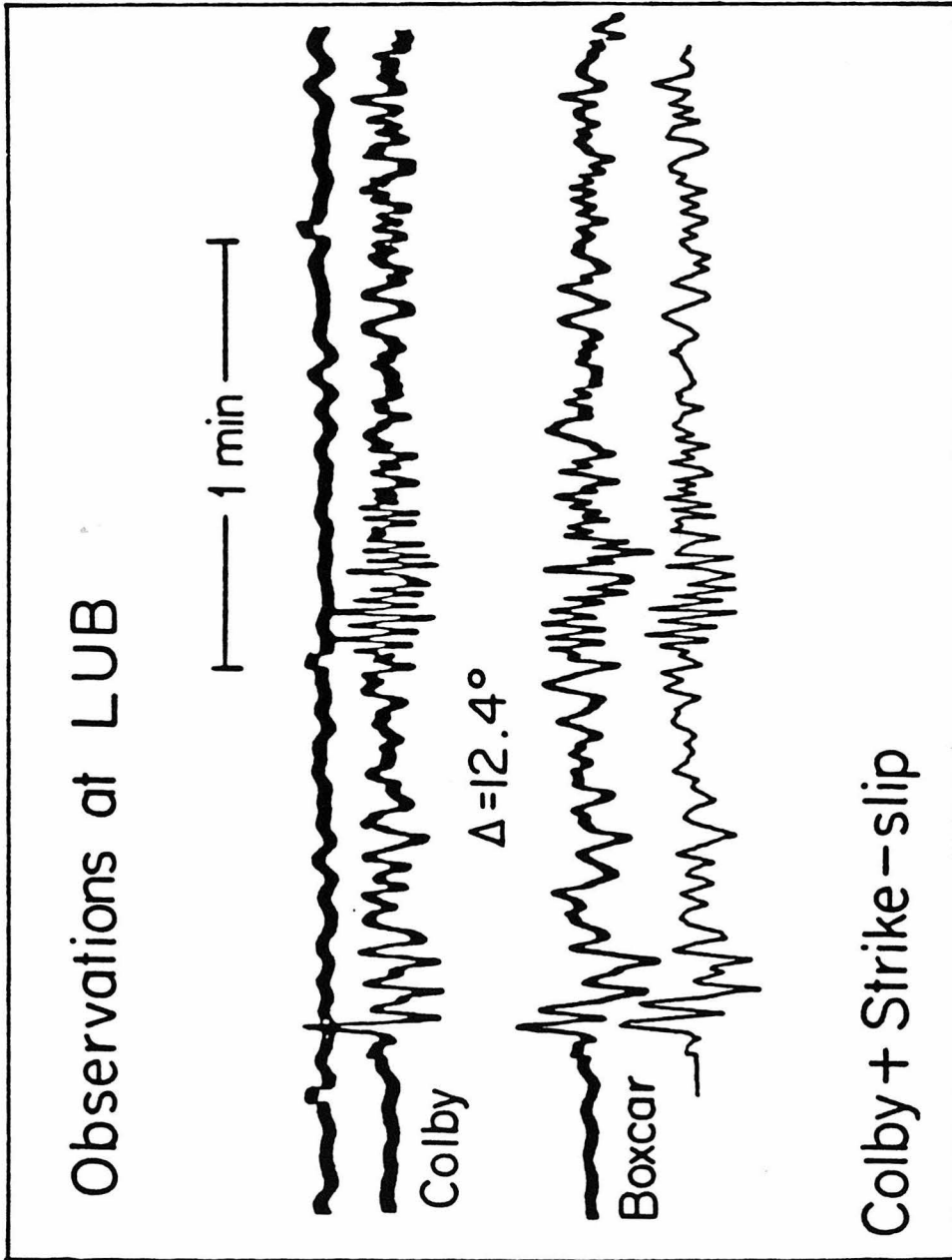


Figure 5-6: A comparison of the P and PL waves for BOXCAR and COLBY at LUB. Shown below is the COLBY waveform summed with a synthetic seismogram to simulated the tectonic release. The double couple has a pure strike-slip orientation. The time function is a triangle with a 0.6 second duration. The seismic moment for the double couple required to obtain the fit is 5×10^{24} dyne-cm.

perform the same kind of exercise of adding a double-couple synthetic to the KASSERI records to simulate the GREELEY records. In this case we chose a mechanism for the tectonic release which has a small component of dip-slip motion (strike-slip to dip-slip ratio of 5-to-1). The dip-slip component was used to lower the seismic moment required to get the very strong, second upswing at SHA. Figure 5-8 summarizes the results of this synthesis. Again there is a one-second time lag between the explosion and the tectonic release. The moments which were used for the double couple were 5×10^{24} dyne-cm for the strike-slip component and 1×10^{24} dyne-cm for the dip-slip component. The time-function has a source duration of 0.6 seconds (a triangle with 0.3 second rise and fall). The overall fit of the simulations to observations is quite good considering the large range of Δ 's. At LUB there is very little diving ray energy present, but at the distance of JCT the predominant arrivals are diving and there is still coherence between the observation and prediction. At DAL an arrival associated with the 400 km discontinuity is quite important, but the GREELEY record is still well predicted (the 400 km discontinuity causes the very strong second downswing). Finally, the waveform at SHA is fairly simple and the effect of the tectonic release sP is obvious. A slightly longer time function would improve the fits at LUB and JCT (a time function of 1.0 second duration brings out the interference in the second pulse at JCT quite well) but degrades the fit at DAL and SHA. If we increase the length of the time function by 25 per cent the stress drop decreases by a factor of 2, still a very high value for triggered fault motion.

The comparison of records over this southern profile of stations results in a consistent picture; the distortion of the waveforms can be explained by the addition of a double couple to simulate the tectonic release. Unfortunately, there is not another profile of stations along constant azimuth with which we can conduct a similar

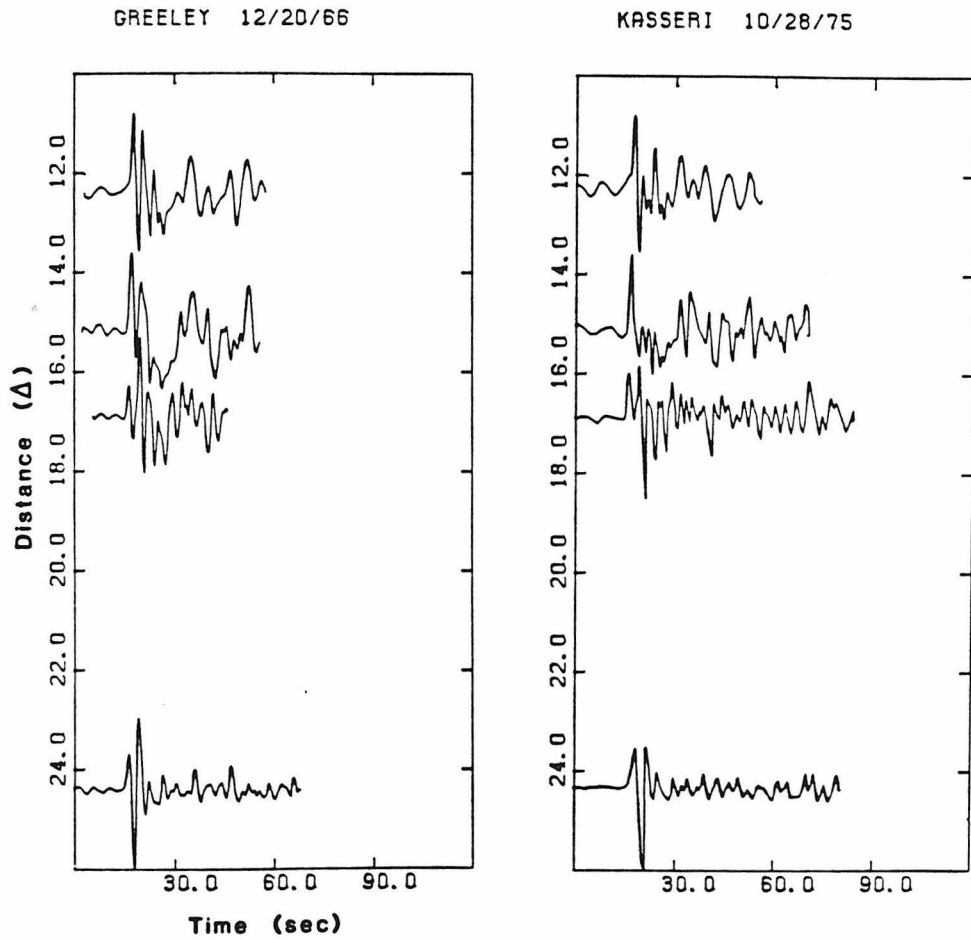


Figure 5-7: A comparison of the waveforms for GREELEY and KASSERI. Shown are LUB, JCT, DAL, and SHA. The two explosions look very similar with the exception of the large second arrival for GREELEY.

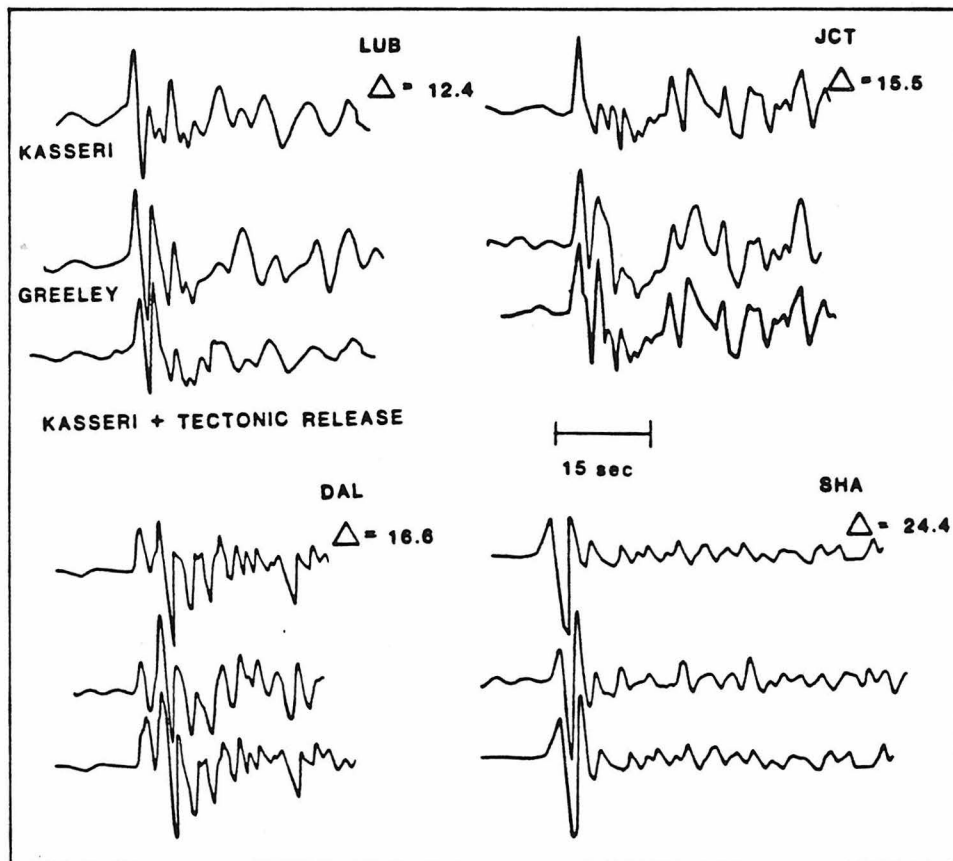


Figure 5-8: A comparison of the GREELEY waveforms with those predicted by KASSERI plus tectonic release. The tectonic release time function is a triangle with a 0.6 second duration. The fault orientation is a 5-to-1 ratio of strike-slip to dip-slip motion. The total moment is 6×10^{24} dyne-cm.

analysis, so it is difficult to constrain the strike direction of the double couple on the basis of the upper-mantle records alone. We can do a comparison of RCD with LUB, which is approximately the same distance from NTS, but should be in the opposite quadrant (negative) for the double couple. Figure 5-9 shows a comparison of GREELEY at LUB and RCD. Also shown is the RCD seismogram for the 8/16/66 Nevada earthquake. The two explosion records are quite similar, but appear to have the long-period content of the waveforms reversed in polarity. We have attempted to simulate the GREELEY waveform at RCD by assuming that the Nevada earthquake waveform is representative of the tectonic release. The earthquake waveform was added to an explosion source synthetic. This sum is shown below the GREELEY waveform. Although the waveform fit is not as good as that for the single-station comparisons, where the explosions have the same source structure and travel path, it is still good enough to be suggestive of several things. The long-period signature is fit quite well in that the ratio of the downswing to upswing amplitude for the second pulse is roughly correct. The difference in travel path length makes the earthquake waveform slightly too dispersed. The orientation of the Nevada earthquake is similar to that which we would expect for the tectonic release, so the approximate fit of the composite seismograms to the RCD GREELEY record supports the hypothesis that RCD and LUB are in opposite radiation quadrants.

Regional Distance Records: At regional distances the seismograms are very complicated due to the waveguide nature of the crust. The mode conversions (S-to-P and P-to-S) at the surface and Moho are very important to the P_{nl} waveform. Since the waveform is sensitive to both P and SV it contains a large amount of information about the seismic source. By making certain assumptions about the crustal structure it is possible to invert the P_{nl} waveforms of shallow, moderate-size

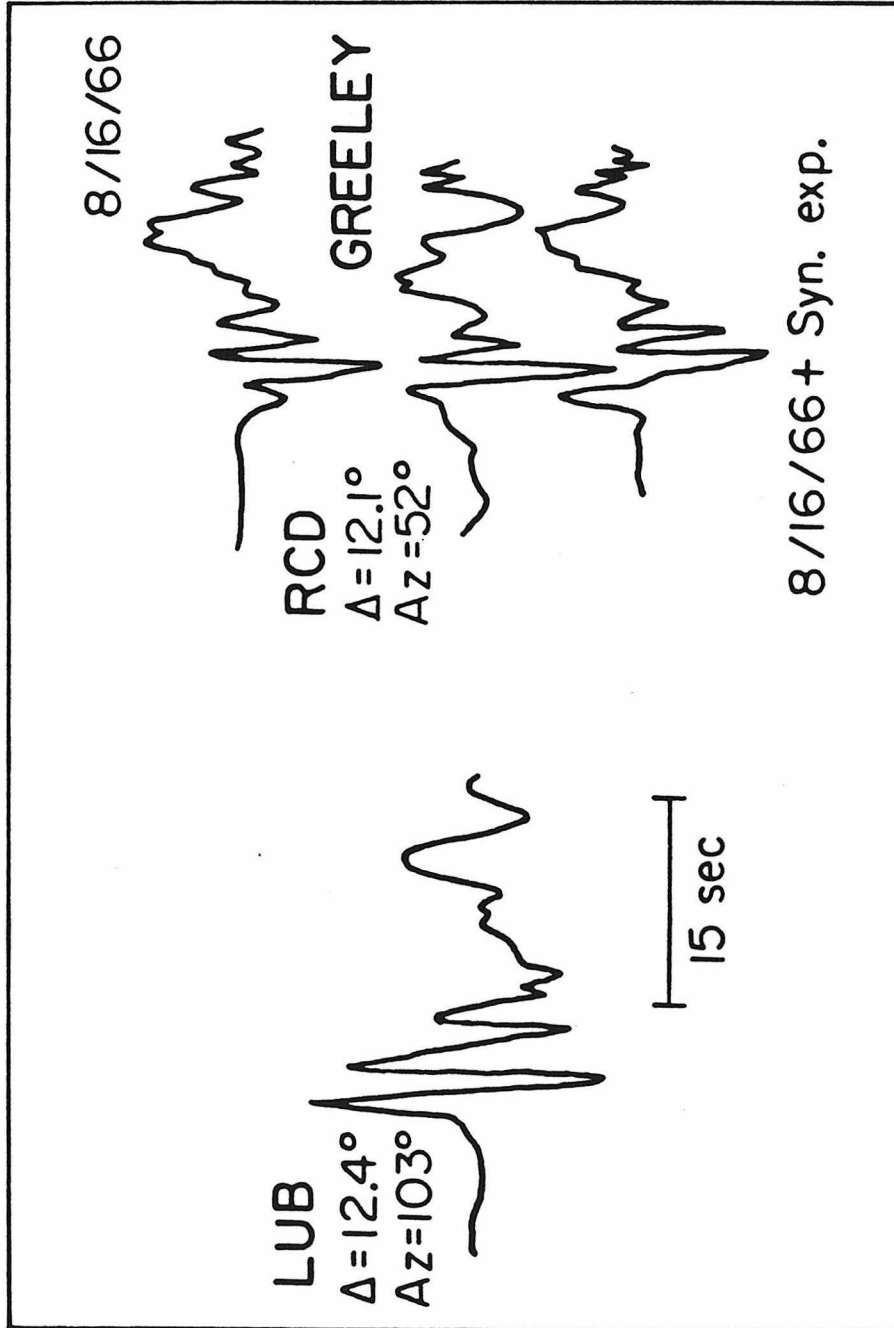


Figure 5-9: A comparison of the GREELEY waveforms at LUB and RCD. Also shown is the waveform of the 8-16-66 earthquake. This earthquake was used to simulate the GREELEY record by summing with a synthetic explosion waveform.

earthquakes to determine the fault orientations (*Wallace et al.* 1981a). On the other hand, a pure explosion source has a P_{nl} waveform which is quite distinct from those of earthquakes. The absence of S in the source and the very high frequency time function result in seismograms which "ring". Under favorable circumstances, if a double couple is superimposed on an explosion source, the waveforms are distorted in such a fashion that it is possible to recover the orientation of the fault.

Certain systematic effects emerge for some of the seismograms from the Pahute Mesa explosions. For example, the P_{nl} waveforms recorded at ALQ and TUC appear much more like those produced by earthquakes than explosions. Figure 5-10 is a composite of different explosions recorded at regional stations. These long-period seismograms have been convolved with a filter whose impulse response is a triangle with a 2 second rise and fall. Shown below the observations are a pair of synthetics which have been similarly filtered. The synthetics were generated with generalized rays using the crustal model in Table 5.1 in Appendix V-1. For each synthetic pair, the top trace is for an explosion source, while the lower trace is for a double couple source which has a strike-slip mechanism. The orientation of the fault was taken from the surface-wave work of *Toksoz and Kehler* (1972): right lateral motion on a plane striking N15° W. ALQ and TUC are in the radiation lobe for the tectonic release P_{nl} , while LON, which is in good agreement with the explosion synthetic, is near a node. DUG, which is in the negative quadrant, has a greatly reduced P amplitude. The first P pulse at DUG is only two thirds that which would be predicted on the basis of HANDLEY records at LON. This is significant in that the DUG P amplitude is not systematically small. For a low tectonic-release event (COLBY) the amplitude is larger than would be predicted on the basis of LON. Although Figure 5-10 is a composite and no doubt the tectonic release varies from shot to shot, it is highly suggestive

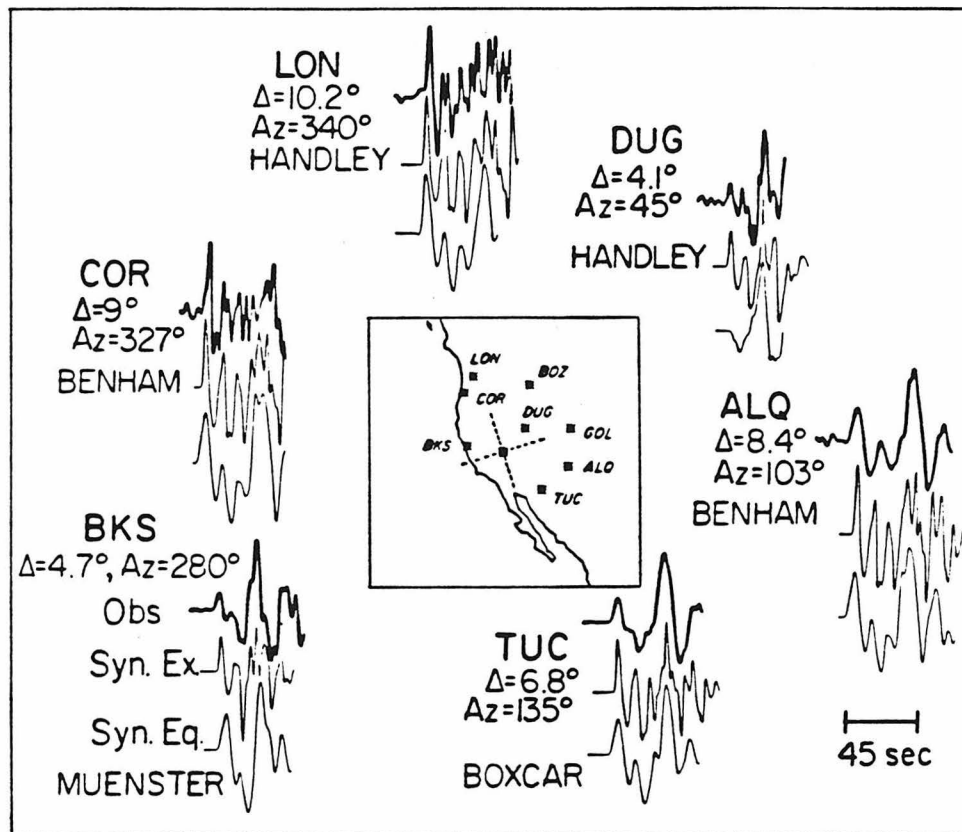


Figure 5-10: The P_nL waveforms for several Pahute Mesa explosions (top trace at each station) and synthetics for an explosion source (middle trace) and a double couple (bottom trace) source. Both the observations and synthetics were lightly filtered. The fault orientation for the double couple is strike-slip; the nodal planes are sketched on the location map.

that there is a significant tectonic release signature on the P_{nl} waveforms.

FAULTLESS was detonated about 100 km north of Pahute Mesa at Hot Creek Valley, Nevada. In contrast to the Pahute explosions, the FAULTLESS P_{nl} waveforms show much less evidence of tectonic release. Figure 5-11 shows the regional long-period records. Again the waveforms have been filtered as described above. Shown below each observation is a synthetic for an explosion source. Although TUC is not fully explained by an explosion alone, the tectonic release must be down by a factor of 3 in comparison to GREELEY or a factor of 2 compared to BOXCAR.

In this analysis it was assumed that differences between the observed explosion and the explosion synthetics can be isolated in the source. To determine the importance of the tectonic release, a double couple was added to the explosion synthetics until the fit to the observations was maximized. The attempt here is to qualify the nature of the tectonic release, so each record was fit independently although the orientation of the double couple was constrained to be the same for all the records. The explosion synthetics were constructed using a source time function described by *Helmberger and Hadley (1981)*. They used their source time function to model both the near-in velocity records and the far-field displacements for HANDLEY, one of the explosions considered in this report, so the values they determined for rise time and overshoot ($k = 5$, $B = 2$) were assumed for all the modeling. Changing the values of k and B within reasonable limits has little effect on the filtered synthetics. This is similarly true if we had used a *Haskell (1967)* source or a *Von Seggern and Blandford (1972)* source.

Strike-slip orientations have the largest effect on the P_{nl} waveforms for explosions. The displacement response from dip-slip faulting is higher frequency than that for strike-slip motion (this is a result of excitation) and generally adds or subtracts

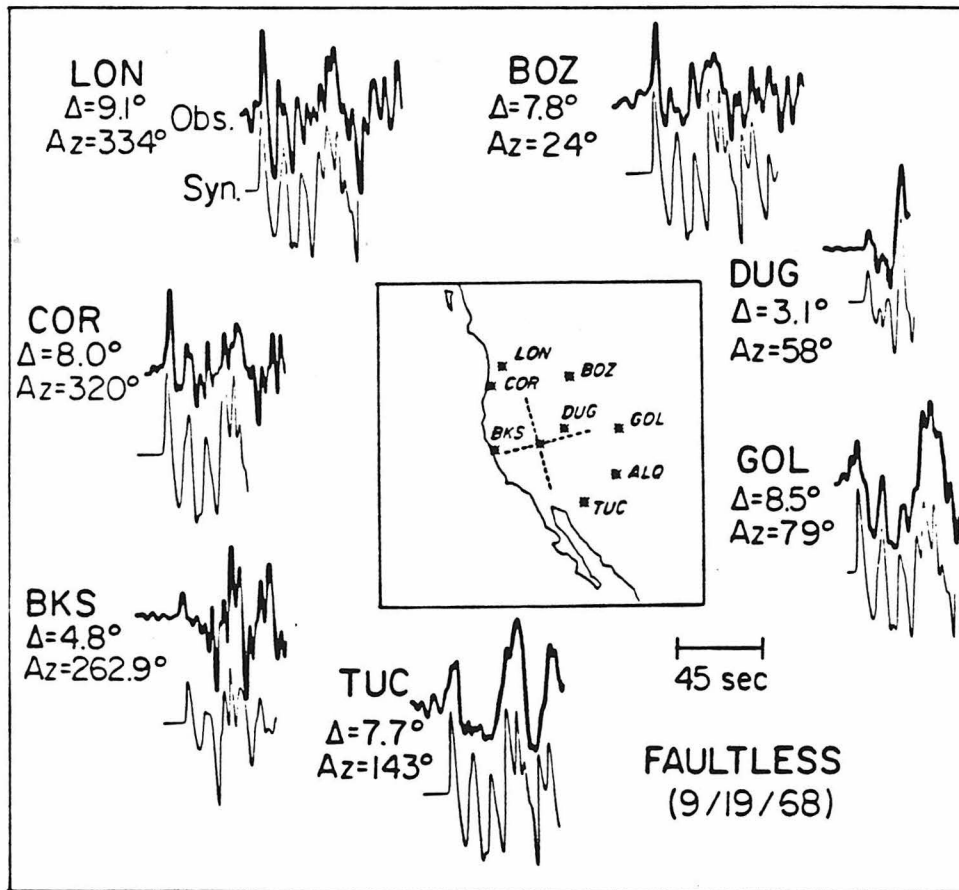


Figure 5-11: A comparison of the P_nL waveforms for the explosion FAULTLESS (top trace) and synthetics computed for an explosion source. Both observations and synthetics have been lightly filtered.

to the explosion waveform without substantially changing it. Since the ratio of dip-slip to strike-slip motion is small on the basis of upper mantle records, only the orientation of the strike-slip component was determined. Different orientations for the strike were tested for compatibility with the observations. Figure 5-12 summarizes the analysis. Shown are the same explosions as in Figure 5-10 and synthetics generated for a combination of double couple and explosion. The LON and COR records have a profound effect on the strike of the double couple. The contribution of the explosion to the waveform is much greater than that of the double couple, implying that these stations are near the node of the radiation pattern. This is particularly true of LON for nine different explosions. The best fitting strike-slip fault has a strike of $N20^{\circ}W$, not significantly different from that of *Toksoz and Kehrler (1972)*. The numbers to the right of each seismogram pair in Figure 5-12 give the ratio of Pn displacement caused by the explosion contribution to that caused by the strike-slip dislocation. Since different explosions were used in the composite figure, no absolute moments are given. Rather, these ratios give a measure of the importance of tectonic release for a given azimuth.

5.4 DISCUSSION

The main interpretation of the previous sections is that tectonic release has a significant effect on the signature of long-period P waves. What now must be done is to integrate this observation with the previous work on surface waves and teleseismic short-period P waves. There are two basic theories for the release of pre-existing tectonic stress by an explosion. The first, summarized by *Aki and Tsai (1972)*, is the triggering of a dislocation along a nearby fault. The second, is stress relaxation from the highly fractured zone immediately around the detonation point

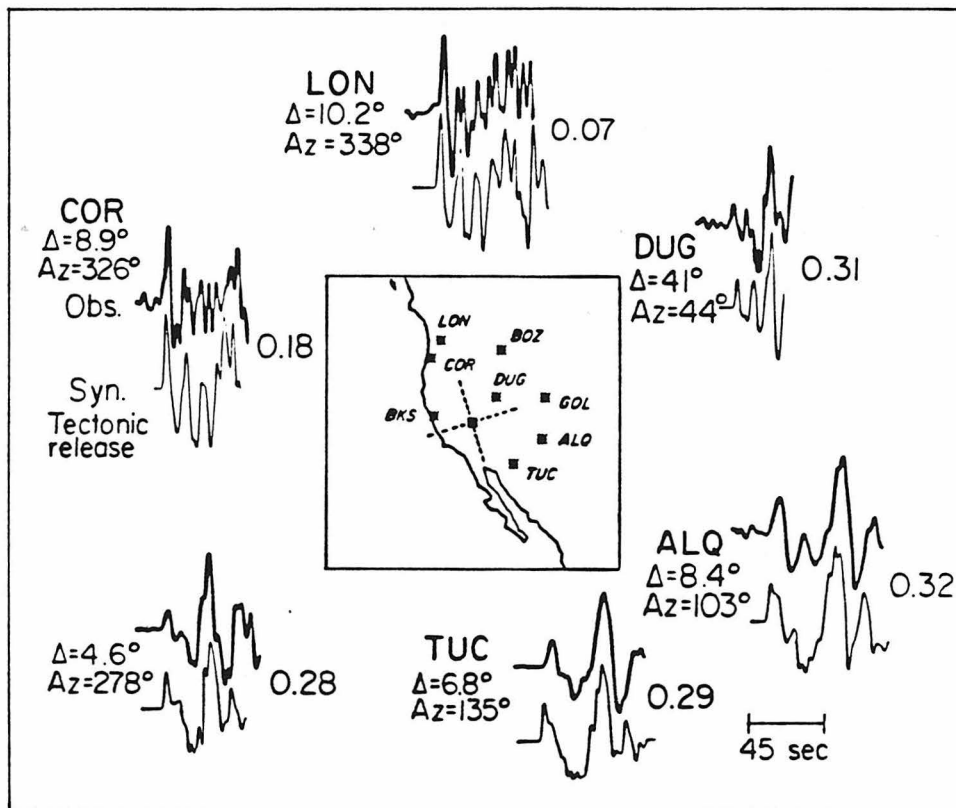


Figure 5-12: A comparison of the P_n waveforms of the same explosions as in Figure 5-10 and synthetic explosion waveforms with a component of tectonic release. Both observations and synthetics have been lightly filtered. The numbers to the right of each seismogram pair give the ratio of P_n amplitude due to the double couple.

(*Archaubeau*, 1972). Most of the previous work on tectonic release has relied on the surface-wave amplitude to determine the moment which in turn was used to obtain the stress-drop by relating the moment to the fault dimensions (as determined from aftershocks) or the volume of pulverized material. *Aki* and *Tsai* (1972) argue that the ratio of the fault dimensions to moment (the moments they obtain are smaller although roughly consistent with those in this study) requires low stress-drops; on the order of 10 bars. Since the surface waves that are used in this analysis have periods longer than 10 seconds there is little resolution of the time function. The shape of the time function can be used as another measure of stress-drop. In most fault models the time function is some convolution of a dislocation function and source finiteness. Therefore, the time function is dependent on the area of rupture as well as the average displacement on the fault. Assuming certain average properties about the rupture and displacement history, it is possible to relate the source duration to stress drop. We use a simple model in which the length of faulting is approximately the product of the source duration and the rupture velocity. Therefore, the stress drop is proportional to the time function (for a given moment, a time function which has a shorter duration has a higher stress drop than one which has a longer duration). We can calculate a fault length for GREELEY and BOXCAR on the basis of the time functions required to fit the upper mantle observations. Assuming a S-velocity of 3 km/sec and rupture velocity of $.8\beta$, then the fault length is on the order of 1.5 to 2 km. Using the formula (*Kanamori* and *Anderson*, 1975)

$$\Delta\sigma = \frac{7}{16} \frac{M_0}{a^3} \quad (5.1)$$

where a is the radius of rupture would give a stress-drop between 300 and 600 bars. This is an order of magnitude larger than *Aki* and *Tsai's* values. We can also

compare this result to a number of recent studies which investigate the relationship between source duration of earthquakes and seismic moment (*Ebel et al.*, 1978; *Liu and Kanamori*, 1980; *Cohn et al.*, 1982). In all cases, the short duration of the tectonic release translates into a stress drop which is an order of magnitude larger than would be expected for an earthquake of similar moment.

If tectonic release is a triggered earthquake, the frequency dependence of the stress-drop is not without precedent. Numerous authors (*Hart et al.*, 1977; *Lay and Kanamori*, 1980; *Ebel*, 1980; *Boatwright*, 1980; among others) have noted a large discrepancy between the moment computed with the body and the surface waves. The asperity model suggests that this phenomenon results from the body waves being radiated from small, strongly coupled, isolated regions while the fault as a whole radiates the surface waves. A similar argument can be made for stress-drop; the asperities have a high stress-drop. It is becoming apparent that for most earthquakes which are studied in detail in both the near-field and far-field, faulting often involves high stress-drop asperities (*Hartzell and Helmberger*, 1982; *Wallace et al.*, 1981b; *Liu and Helmberger*, 1982). If this is the case for tectonic release, the question is not so much how to rectify the long-period P waves and the surface-wave stress drops, but rather, should there be a strong short-period signature.

The 8/16/66 Nevada earthquake appears to be very similar to the tectonic release from GREELEY, although the stress drop appears to be a factor of two smaller. For this earthquake there were significant teleseismic short periods at 30° , in particular on the east coast of the U.S. Beyond 40° the short-periods were rarely visible on the WWSSN network. This is an expression of the strike-slip orientation; P waves are not efficiently radiated to teleseismic distances. The higher stress drop from the tectonic release probably would cause records to be written at larger

distances. Since the main phase radiated is sP there would be only a very small change in the a-b amplitude of an explosion with a tectonic release time function similar to those in this study. T. Lay (personal communication) has shown that at a distance of 50° a strike-slip mechanism with a moment of 5×10^{24} dyne-cm will effect the a-b amplitude by about 10 percent between maximum radiation lobes. On the other hand, the part of the waveform which corresponds to the arrival of sP has distinguishable differences. A comparison of short-period waveforms on the east coast show only minor differences between high and low tectonic release events. This leaves two possible conclusions: (1) the stress-drop must be lower, or (2) the spectra of the time function is peaked at 2-3 seconds. The stress-drops can be reduced by a factor of 2 by assuming that the rupture velocity of the tectonic release is approximately the P-velocity. In this case, the mechanism of tectonic release is fault motion driven by the explosion. Even with this reduced stress drop, the waveforms for high and low tectonic release events recorded on the east coast stations should show more variance than is observed. Although it is difficult to construct a time function which is strongly peaked at the pass band of the long-period P waves, the direction of rupture can produce a frequency dependent effect. The very strong similarity of the GREELEY SH waves with those of the Nevada earthquake suggests that the point source location of the tectonic release is deeper than the working point. Similarly, the time lag for the summing process in Figure 5-8 suggests that the best point source hypocenter of the tectonic release is on the order of 4 km. If we assume that the fault is driven by the explosion, then the rupture starts at the working point and is driven downward. *Liu and Helmberger (1982)* have shown that the short-period sP is greatly reduced compared to the long-period sP for a strike-slip event rupturing downward. This type of phenomenon could explain the

apparent inconsistency between the long and short-period data.

The fact that tectonic release is significantly reduced for explosions which are detonated close to the site of a previous explosion can be used to estimate the dimensions of the crust in which the stresses are relieved. On the basis of FONTINA and BOXCAR, the minimum radius of area affected by a megaton explosion is on the order of 3 km. On the other hand, CAMEMBERT is about 4 km from KASSERI and GREELEY but shows substantial tectonic release. Similarly BOXCAR and GREELEY are about 4.5 km apart and are apparently unaffected by each other. Assuming that 4 km is the outer radius at which stress relaxes for megaton events, it is possible to calculate the stress drop expected in the *Archambeau* (1972) cavity model. Using the elastic parameters given in *Bache* (1976) the stress drop must be at least 500 bars. This is in agreement with the time function found in this study, but again stress-drops this large should radiate sufficient short-period seismic energy to cause obvious waveform distortion.

It is apparent that the tectonic-release parameters determined from the long-period P waveforms does not fit neatly in either theory for tectonic release. We prefer a driven fault model, with the bulk of the tectonic release occurring deeper than the working point of the explosion. This type of stress release mechanism incorporates features from both the cavity and triggered earthquake models. It is interesting to note that CAMEMBERT and MUENSTER are smaller than most of the other explosions studied here, but still showed significant tectonic release. It is also true that these two explosions have a high ratio of depth of burial to yield.

5.5 CONCLUSIONS

Certain megaton explosions on Pahute Mesa have a long-period body waveform distortion which can be modeled as the signature of tectonic release. The tectonic release can be sufficiently represented as a double couple. Long-period WWSSN data at regional and upper-mantle distances constrain the double couple to be primarily strike-slip, which is in agreement with previous work on NTS surface waves. The events with the largest tectonic release (BENHAM and GREELEY) have double couples with moments on the order of 5×10^{24} dyne-cm. In the case of megaton explosions, detonations within a 4 km radius of previous large explosions result in a substantially reduced component of tectonic release.

The modeling of the sP phase from the double couple requires a time function which has a short duration. The moments determined both from the sP and SH amplitudes require very high stress-drops if the short duration time functions are interpreted in terms of a triggered fault. Similarly, the cavity model would also predict high stress-drops. It seems likely that stress drops higher than 300 bars should produce a detectable short-period tectonic release signature. Since, at this time, the evidence for short-period distortions is lacking, the long-period P-wave data does not easily fit either the triggered fault or cavity mechanism for stress release. Fault motion which is driven by the explosion and ruptures downward could account for the observed long-period and short-period data. A driven fault would be in better agreement with the observations.

REFERENCES

- Aki, K. and Y.B. Tsai (1972). Mechanism of Love wave excitation by explosion sources, *J. Geophys. Res.*, 77, 1452-1475.
- Aki, K., P. Reasenber, T. DeFazio and Y. Tsai (1969). Near-field and far-field seismic evidence for triggering of an earthquake by the Benham explosion, *Bull. seismo. Soc. Am.*, 59, 2197-2209.
- Archambeau, C.B. (1972). The theory of stress wave radiation from explosions in prestressed media, *Geophys. J.* 29, 329-366.
- Bache, T.C. (1976). The effect of tectonic stress release on explosion P-wave signatures, *Bull. seismo. Soc. Am.*, 66, 1441-1457.
- Boatwright, J. (1980). Preliminary body wave analysis of the St. Elias Alaska, earthquake of February 28, 1979, *Bull. seismo. Soc. Am.*, 70, 419-436.
- Bucknam, R.C. (1969). Geologic effects of the Benham underground nuclear explosion, Nevada Test Site, *Bull. seismo. Soc. Am.*, 59, 2209-2220.
- Burdick, L. and D. Helmberger (1978). The upper mantle P velocity structure of the western United States, *J. Geophys. Res.* 83, 1699-1712.
- Cohn, S.N, T.L. Hong and D.V. Helmberger (1982). The Oroville earthquakes; a study of source characteristics and site effects, *J. Geophys. Res.*, 87, 4585-4594.
- Dahlman, O. and H. Israelson (1977). *Monitoring Underground Nuclear Explosions*, Elsevier, New York, 440p.
- Ebel, J.E. (1980). Source processes of the 1965 New Hebrides Island earthquakes inferred from teleseismic waveforms, *Geophys. J.*, 63, 381-403.

- Ebel, J.E., L.J. Burdick and G.S. Stewart (1978). The source mechanism of the August 7, 1966, El Golfo earthquake, *Bull. seismo. Soc. Am.*, 68, 1281-1292.
- Goforth, T. (1982). Anomalous Rayleigh waves from presumed explosions at the Shagan River test site-A, abstract, DARPA symposium, Hampton, Va.
- Hamilton, R.M. and J.H. Healy (1969). Aftershocks of the Benham nuclear explosion, *Bull. seismo. Soc. Am.*, 59, 2271-2281.
- Hart, R.S., R. Butler and H. Kanamori (1977). Surface wave constraints on the August 1, 1975 Oroville earthquake, *Bull. seismo. Soc. Am.*, 67, 1281-1292.
- Hartzell, S. and D.V. HelMBERGER (1982). Strong-motion modeling of the Imperial Valley earthquake of 1979, *Bull. seismo. Soc. Am.* 72, 571-596.
- Haskell, N.A. (1967). Analytic approximations for the elastic radiation from a contained underground explosions, *J. Geophys. Res.*, 72, 2583-2587.
- HelMBERGER, D.V. and G.R. Engen (1980). Modeling the long-period body waves from shallow earthquakes at regional ranges, *Bull. seismo. Soc. Am.*, 70, 1699-1714.
- HelMBERGER, D.V. and D.M. Hadley (1981). Seismic source functions and attenuation from local and teleseismic observations of the NTS events Jorum and Handley, *Bull. seismo. Soc. Am.*, 71, 51-67.
- Johnson, L.R., T.V. McEvilly and K.L. McLaughlin (1982). Near-field recordings of ground accelerations from the Harzer explosion, abstract, *EOS*, 62, 971.
- Kanamori, H. and D.L. Anderson (1975). Theoretical basis of some empirical relations in seismology, *Bull. seismo. Soc. Am.*, 65, 1073-1095.
- Lay, T. and H. Kanamori (1980). Earthquake doublets in the Solomon Islands, *Phys. Earth Planet. Inter*, 21, 283-304.
- Liu, H.L. and H. Kanamori (1980). Determination of source parameters of mid-plate

- earthquakes from the waveforms of body waves, *Bull. seismo. Soc. Am.*, 70, 1989-2004.
- Liu, H.L. and D.V. Helmberger (1982). The near-source ground motion of the August 6, 1979 Coyote Lake California Earthquake, *Bull. seismo. Soc. Am.*, submitted.
- Nuttli, O.W. (1969). Travel times and amplitudes of S waves from nuclear explosions in Nevada, *Bull. seismo. Soc. Am.*, 59, 385-398.
- Press, F. and C.B. Archambeau (1962). Release of tectonic strain by underground nuclear explosions, *J. Geophys. Res.*, 67, 337-343.
- Smith, R.B. and M.L. Sbar (1974). Contemporary tectonics and seismicity of the Western United States with emphasis on the Intermountain seismic belt, *Geol. Soc. Am. Bull.*, 85, 1205-1218.
- Toksoz, M.N. and H.H. Kehrler (1972). Tectonic strain release by underground nuclear explosions and its effect on seismic discrimination, *Geophys. J.*, 31, 141-161.
- Toksoz, M.N. and H.H. Kehrler (1971). Underground nuclear explosions; tectonic utility and dangers, *Science*, 173, 230-233.
- Toksoz, M.N., A. Ben-Menahem and D.G. Harkrider (1964). Determination of source parameters by amplitude equalization of seismic surface waves, 1. underground nuclear explosions, *J. Geophys. Res.*, 69, 4355-4366.
- Von Seggren, D., and R. Blandford (1972). Source time functions and spectra for underground nuclear explosions, *Geophys. J.*, 31, 83-97.
- Wallace, T.C., D.V. Helmberger and G.R. Mellman (1981a). A technique for the inversion of regional data in source parameter studies, *J. Geophys. Res.*, 86, 1679-1685.
- Wallace, T.C., D.V. Helmberger and J.E. Ebel (1981b). A broadband study of the 13 August 1978 Santa Barbara earthquake, *Bull. seismo. Soc. Am.*, 71, 1701-1718.

Appendix V-1

A moderate size earthquake ($m_b = 5.6$, ISC) which occurred on August 16, 1966 (OT; 18:02) near the Nevada-Utah border (epicentral coordinates: 37.4°N , 114.2°W) produced good regional waveforms at five WWSSN stations. Using the crustal model in Table 2-1 it is possible to invert these waveforms to obtain the source mechanism (see *Wallace et al.*, 1981, for a description of the technique). Figure V-1-1 summarizes the analysis. Shown are the vertical and radial P_{nl} observations and below are the synthetics computed for the inversion source. Both the observations and the synthetics have been lightly filtered. The fault parameters determined from the waveforms are a strike of $\text{N}17^\circ\text{E}$ dipping 80° to the east. The rake (defined as the sense of motion of the hanging wall relative to the foot wall; e.g. pure normal fault motion has a rake of -90°) is 190° , or nearly pure right-lateral strike-slip. This solution is in close agreement with that of *Smith and Sbar's* (1974) which was determined on the basis of local first motions; strike = $\text{N}14^\circ\text{E}$, dip = 80°W , rake = 170° . The moment of the earthquake can be determined by comparing the amplitude of the observations and the synthetics. The ratio of the moment determined from each seismogram to the average moment is shown in Figure V-1-1 to the right of each trace.

The teleseismic short-periods at nine stations were modeled for source depth and time-function. The separation of P and sP indicates that the hypocenter is on the order of 6 km deep. Six of these records are shown in Figure V-1-2. In the short-period modeling it was assumed that the source orientation is known; depth and

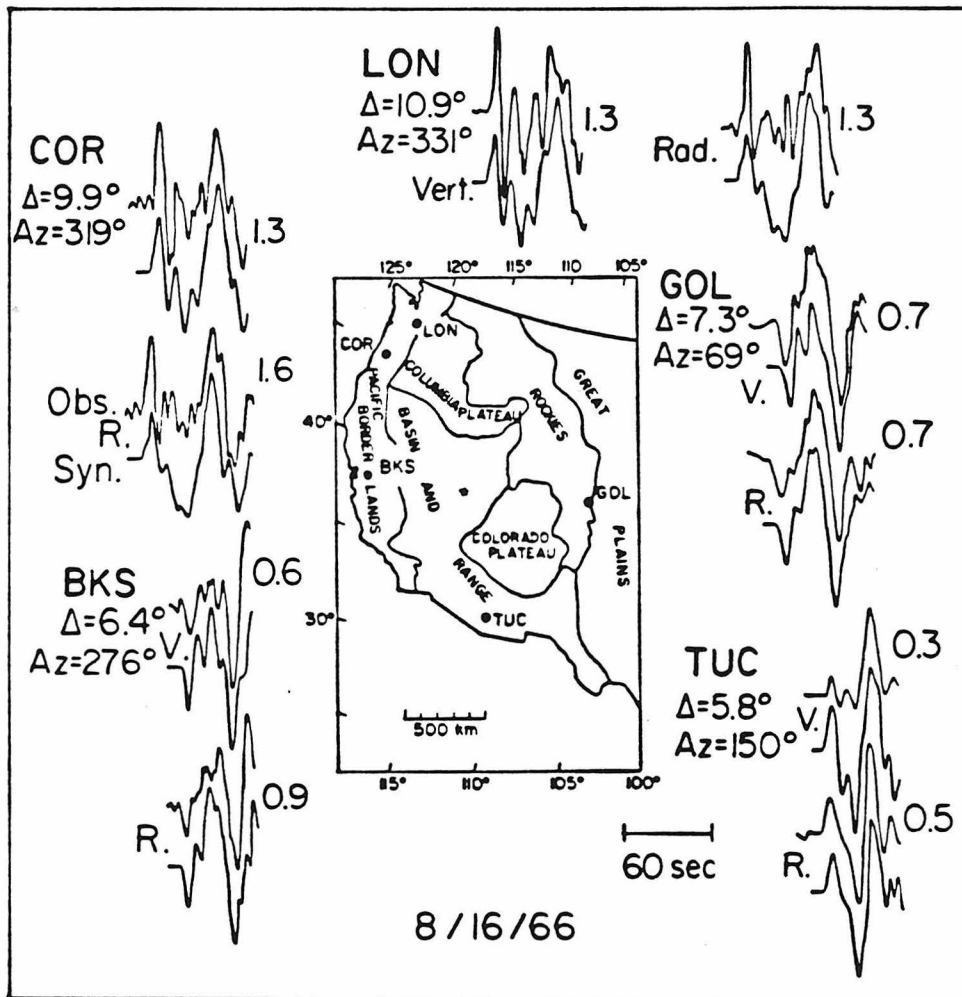


Figure V-1-1: Location of the 8-16-66 Nevada earthquake (star) and recording stations. Both radial and vertical components are shown. For each seismogram pair the top trace is the observation while the lower trace is a synthetic computed with the source orientation given by the inversion. The moment of the event is 4.1×10^{24} dyne-cm. The numbers to the right of each seismogram pair give the ratio of the moment determined from that trace to the average moment.

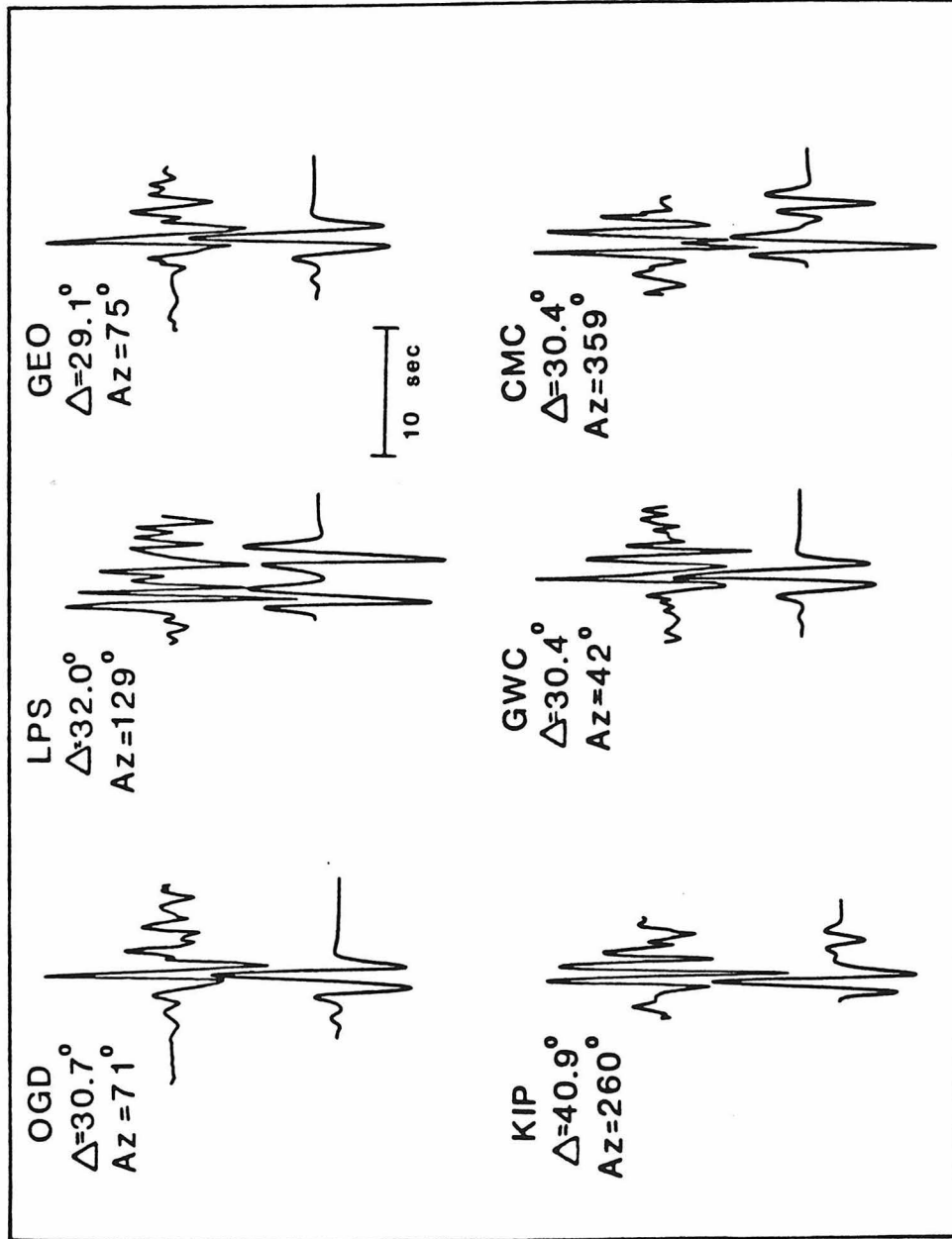


Figure V-1-2: A comparison of the short-period seismograms (top trace) and synthetic waveforms calculated for the fault orientation given by the regional waveforms. The depth is 6 km.

time function are the only unknowns. In Figure V-1-2 the depth phase sP is often the largest arrival. For example, the OGD waveform has a small, but clear, P and pP followed by a large sP. There obviously is some uncertainty in depth, but the event probably can not be shallower than 4 km or deeper than 8 km. The short-period time function was a trapezoid with a 0.4 second rise, 0.5 second top and 0.4 second fall. The short-period amplitudes give a moment of 4.2×10^{24} dyne-cm, consistent with the long-period analysis. The 8/16/66, Nevada earthquake is very similar to a strike-slip event which occurred near Coyote Lake, California on August 6, 1979. *Liu and Helmberger (1982)* give a moment of 3.5×10^{24} dyne-cm for this event, and the analysis of the strong-ground motion data indicates that the event is high stress-drop. The primary rupture occurred along a patch 2 km long and the stress-drop was 150 bars. A comparison of the teleseismic short-period records for the Nevada and Coyote Lake events shows that they are systematically larger for the Nevada event. This implies that the Nevada event is at least as high stress-drop as the Coyote Lake earthquake.

The December 22, 1964, Baja Norte, Mexico earthquake ($m_b = 5.6$, PAS) occurred on the San Miguel Fault zone (OT; 20.54, epicentral coordinates; 31.8° N, 117.1° W). The fault zone strikes N50°W and is right lateral strike-slip. The date of the event coincides with operation of a large number of LRSM stations in the southwestern U.S., which provided 15 P_{nl} waveforms used in the inversion for source parameters. The analysis is summarized in Figure V-1-3. As before, the observation (verticals only) are shown above the synthetic computed for the fault model. The fault parameters are strike = 312° , dip = 85° and rake of 177° . The moment is 8×10^{24} dyne-cm. The depth of the event is not well constrained but is between 2 and 8 km.

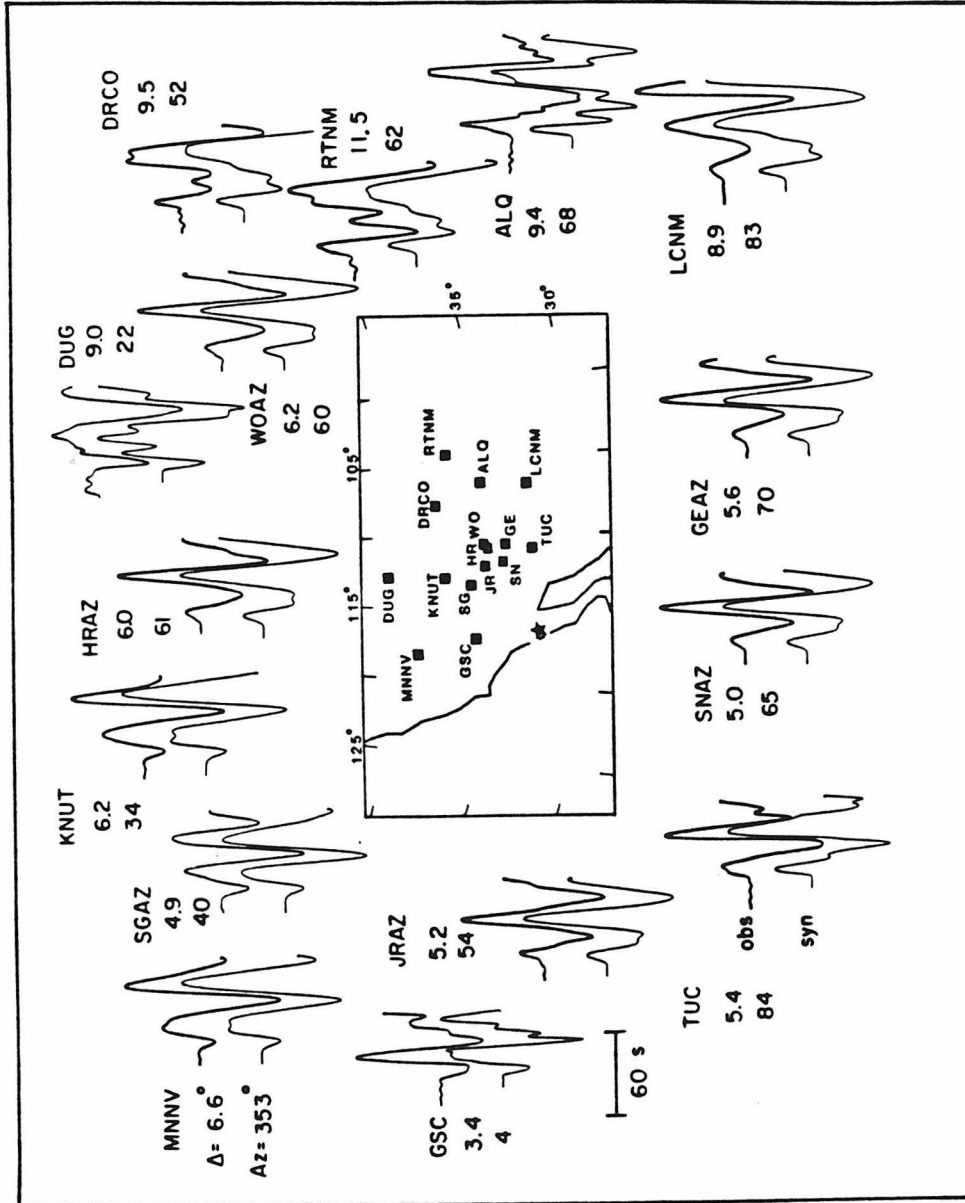


Figure V-1-3: Location of the 12-22-64 San Miguel earthquake (start) and the recording stations. The stations with two and four letter designations are LRSM while those with three letters are WWSSN. Also shown are the vertical component (top trace) and synthetics (bottom) computed with the inversion fault orientation. The moment of the event is 8×10^{24} dyne-cm.